Spring 5-15-2018

Fluorescence Guided Tumor Imaging: Foundations for Translational Applications

Jessica P. Miller
Washington University in St. Louis

WASHINGTON UNIVERSITY IN ST. LOUIS

Division of Biology and Biomedical Sciences

School of Engineering and Applied Science

Department of Biomedical Engineering

Dissertation Examination Committee:
Samuel Achilefu, Chair
Rebecca Aft
Mark Anastasio
Jianmin Cui
Joseph Culver
Henry Lai

Fluorescence Guided Tumor Imaging: Foundations for Translational Applications

By

Jessica P. Miller

A dissertation presented to
The Graduate School
of Washington University in
partial fulfillment of the
requirements for the degree
of Doctor of Philosophy

May 2018
St. Louis, Missouri

Table of Contents

List of Figures

List of Abbreviations

Chapter 1: Optical coherence tomography (OCT), diffuse optical tomography (DOT), fluorescence molecular tomography (FMT), near infrared (NIR).

Chapter 3: Planar view tumor volume algorithm (PV-TVA), fluorescence molecular tomography (FMT), bioluminescence imaging (BLI), computed tomography (CT), positron emission tomography (PET), magnetic resonance imaging (MRI), region of interest (ROI).

Chapter 4: Structured illumination microscopy (SIM), solitary extramedullary plasmacytoma (SEP), structured illumination fluorescence molecular imaging (SIFMI), planar fluorescence reflectance imaging (PFRI), diffuse optical spectroscopy imaging (DOSI), spatial-frequency domain imaging (SFDI), digital micromirror device (DMD).

Chapter 5: Laminar optical tomography (LOT), signal to background ratio (SBR), sub-surface depth (d_{ss}), total depth (d_{total}), object depth (d_{obj}).

Chapter 6: Dynamic contrast enhanced small animal imaging (DyCE), receiver operating characteristic (ROC).

Chapter 7: Circulating tumor cell (CTC), red blood cell (RBC).

Chapter 8: Squamous cell carcinoma (SCC), photodynamic therapy (PDT), methyl-δ-aminolevulinic acid photodynamic therapy (MAL-PDT), non-melanoma skin cancer (NMSC), photosensitizer (PS), chlorin e6 (Ce6), immunohistochemistry (IHC), average change in tumor volume (ACTV).

Acknowledgments

I would like to thank my advisor Samuel Achilefu for his contribution to my growth as an independent researcher. I would also like to thank my committee for their time, analysis, and suggestions to progress my research. Special thanks to Kurt Thoroughman for his guidance and mentorship through both my master's degree and PhD. Thank you to the department of Biomedical Engineering for their assistance, specifically Karen Teasdale and Kate Ruzicka. Thank you to the MSTP department for giving me the opportunity to take part in this amazing journey. Thank you to Rochelle Smith for opening doors and always encouraging me to walk through them. I would also like to thank my rotation mentors for their contributions to my research interests: Robyn Klein for an introduction to basic science research, and Kristen Naegle for a re-introduction to programming.

I would like to thank the members of the optical radiology lab for the opportunity to work in a collaborative research environment. Rebecca Gilson for her microscopy expertise, Dolonchampa Maji for dye synthesis and experimental collaboration, LeMoyne Habimana-Griffin for FMT expertise, Deep Hathi and Inema Orukari for programming assistance, Steven Wang for camera assistance, Walter Akers for animal experiment assistance, and Gail Sudlow for helping with just about everything in the lab. Thank you to Kexian Liang and Rui Tang for dye synthesis.

Imaging services were provided by WU-MDACC Inter-Institutional Molecular Imaging Center (NCI P50CA094056) and the Siteman Cancer Center Small Animal Imaging Core (NCI P30CA091842). IHC services were provided by Deborah Rubin, MD, and the Digestive Diseases Research Core Center – Advanced Imaging and Tissue Analysis Core (DDRCC-AITAC) at the Washington University School of Medicine (Grant P30-DK52574). 4T1-Luc cells were provided

courtesy of the lab of Dr. Kathy Weilbaecher. Catheter synthesis and placement was conducted by the MIR Pre-Clinical Pet-CT Facility of the Washington University School of Medicine. MCB6 bladder cancer mice provided by the lab of Dr. Vivek Arora. SCC-12 cells were provided courtesy of James Rheinwald, PhD, Harvard University.

Funding for this body of work was provided in part by funds from the US National Institutes of Health (NIH) NCI (R01 CA171651-04S1 and P50 CA094056), NIBIB (R01 EB007276 and R01 EB008111), and shared instrumentation grants (S10 OD016237 and S10 RR031625). NIH NCI: R01CA176221 and the Center for Multiple Myeloma Nanotherapy (U54CA199092). The Optix MX3 was purchased by NIH shared instrument grant S10OD016419.

Jessica P. Miller

Washington University in St. Louis

May 2018

Dedication

Dedicated to my parents, Debbie and Gregory Miller, for their continual love and support.

Additional thanks to all who have inspired and encouraged me over the years.

ABSTRACT OF THE DISSERTATION

Fluorescence Guided Tumor Imaging: Foundations for Translational Applications

By

Jessica P. Miller

Doctor of Philosophy in Biomedical Engineering

Washington University in St. Louis, 2018

Professor Samuel Achilefu, Chair

Abstract

Optical imaging for medical applications is a growing field, and it has the potential to improve medical outcomes through its increased sensitivity and specificity, lower cost, and small instrumentation footprint as compared to other imaging modalities. The method holds great promise, ranging from direct clinical use as a diagnostic or therapeutic tool, to pre-clinical applications for increased understanding of pathology. Additionally, optical imaging uses non-ionizing radiation which is safe for patients, so it can be used for repeated imaging procedures to monitor therapy, guide treatment, and provide real-time feedback. The versatile features of fluorescence-based optical imaging make it suited for cancer related imaging applications to increase patient survival and improve clinical outcomes. This dissertation focuses on the development of image processing methods to obtain semi-quantitative fluorescence imaging data. These methods allow for the standardization of fluorescence imaging data for tumor characterization.

When a fluorophore is located within tissue, changes in the fluorescence intensity can be used to isolate structures of interest. Typically, this is done through the accumulation of a dye in a target tissue either by the enhanced permeation and retention effect (EPR), or through targeted

peptide sequences that bind receptors present in specific tissue types. When imaged, the contrast generated by a fluorescent probe can be used to indicate the presence or absence of a structure, bio-chemical compound, or receptor. Fluorescence intensity contrast can answer many biological and clinical questions effectively; however, we were interested in analyzing more than solely contrast when using planar fluorescence imaging.

To better understand tumor properties, we developed a series of algorithms that harness additional pieces of information present in the fluorescence signal. We demonstrated that adding novel image processing algorithms enhanced the knowledge obtained from planar fluorescence images. Through this work, we gained an understanding of alternative approaches for processing planar fluorescence imaging data with the goal of improving future cancer diagnostics and therapeutics.

Chapter 1 :

Introduction

Optical imaging has the potential to improve medical outcomes in a number of areas. Using light to interrogate tissues is appealing due to the increased sensitivity and specificity, lower cost, and small instrumentation footprint as compared to other imaging modalities. Optical imaging consists of various techniques including, ballistic imaging, optical coherence tomography (OCT), spectroscopy, planar fluorescence imaging, diffuse optical tomography (DOT), and fluorescence molecular tomography (FMT). Each of these techniques has its advantages and is suited for different clinical and pre-clinical applications. This dissertation focuses on planar fluorescence imaging, specifically for the purpose of identifying and characterizing tumors.

Fluorescence is generated by the emission of a photon from a material that has absorbed energy from another source. Often the input energy is in the form of a light source causing the excitation of an electron to a higher energy state. When the electron relaxes back down to its ground state a photon is emitted (**Figure 1-1**). Fluorescence imaging uses a device to capture these photons and create an image. The device can be a camera, photo multiplier tube (PMT), or other instrumentation that is light sensitive in the spectral range of he emitted fluorescence.

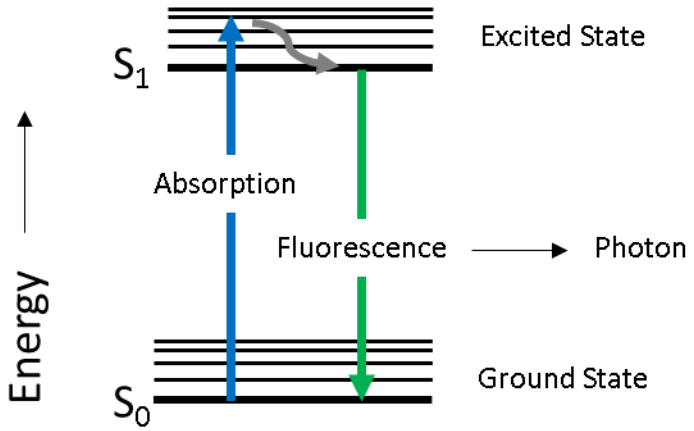

Figure 1-1: Jablonski diagram showing the mechanism of fluorescence. A material is excited by absorbing energy, then when it relaxes back to the ground state a photon is emitted causing fluorescence. Figure courtesy of Dr. Rebecca Gilson.

The majority of fluorescence imaging has been conducted using ballistic light for microscopy, planar imaging for wide-field tissue visualization, or diffuse optical imaging for tomographic analysis. When light passes through a turbid medium the photons are scattered and absorbed according to the optical properties of the tissue. The optical parameters of interest are the attenuation (μ_a) and reduced scattering (μ'_s) coefficients that vary with different tissues. Ballistic light, or light that is reflected and refracted in a predictable manner, occurs when the tissue properties cause negligible light attenuation. Ballistic light largely only occurs at shallow tissue depths, or in biological tissues such as the eyes where light can pass through the medium. In turbid tissue, the number of un-attenuated photons decrease exponentially with propagation distance according to the radiative transport equation. Ballistic light can be used for analysis in techniques such as two-photon imaging, however the depths imaged with this approach are primarily limited to microscopy.

To image at greater depths, optical imaging relies on diffuse optics and solving the radiative transport equation. Tomography involves collecting measurements from multiple angles to computationally determine the spatial location of an inclusion. DOT collects measurements of a 3D volume using a source-detector array, and these multiple measurements are then used to mathematically localize each volume element's relative contribution to the overall signal. FMT employs the same principles of DOT, however the source light excites a fluorophore, which is then detected at the surface. FMT can image to depths in the centimeter range and has been employed clinically for applications such as brain imaging. One of the drawbacks of FMT is that the calculations require extensive computational capacity, which limit real-time feedback applications.

Planar fluorescence imaging bridges the gap between ballistic light analysis and tomography, by using both forms of light to obtain wide-field surface weighted projected images of fluorescence in tissue. This surface weighted image can be readily obtained for rapid feedback making it attractive for a multitude of pre-clinical and clinical applications. When a fluorophore is present, changes in the fluorescence intensity can be used to isolate structures of interest. Typically, this is done through the accumulation of a dye in a target tissue either by the enhanced permeation and retention effect (EPR), or through targeted peptide sequences that bind receptors present in specific tissue types. The contrast generated by a fluorescent probe can indicate the presence or absence of a structure, bio-chemical compound, or receptor. Fluorescence intensity generated contrast can answer many biological and clinical questions very effectively. When near-infrared (NIR) fluorescent dyes are used, tissues can be interrogated to greater depths than with visible light due to the NIR optical window. The NIR optical window is a band of wavelengths at which the attenuation of light in tissue due to endogenous fluorophores is minimized. The optical window is from around 700 nm to 1100 nm. Within this window light can penetrate to centimeter depths in tissue and the spectral interference of tissue autofluorescence is limited.

The deep penetration of NIR light provides additional information as compared to visible light, however it also poses potential challenges for planar imaging modalities. This is because the signal projected to the surface of the tissue is a composite of each layer of underlying tissue. The deconvolution of this signal is complex and has proven to be difficult to conduct without using tomography. In this dissertation we explored methods to de-convolve this signal in order to obtain more information than simply using fluorescence intensity contrast. A series of methods were developed that each harness additional pieces of information in the convolved signal to better understand tumor properties through planar fluorescence imaging. We demonstrate this by

characterizing tumor volume with static fluorescence imaging, delineating the tumor boundary using structured illumination, estimating tumor depth using dual-wavelength imaging, then moving to dynamic imaging to identify tumors based on perfusion and stratify circulating tumor cells. Finally, we demonstrate the ability to monitor and treat tumors using light.

Chapter 2 :

Tumor Fluorescence Imaging

2.1 Tumor Florescence Imaging

In cancer research, molecular probes targeting specific biomarkers have been developed to give insight into tissue specific properties [1,2]. These probes allow for the rapid detection of a tumor, assessment of tumor-associated protein expression levels, and relative size of tumors. Targeted molecular fluorescence imaging has the potential to improve patient care by facilitating the understanding of tumor characteristics in small animal models. Additionally, preclinical testing of new cancer therapies is often conducted in small animal models to determine therapeutic efficacy[3].

Our lab has previously reported on a near infrared (NIR) fluorescent probe that selectively accumulates in tumors *in vivo*[4]. This probe, LS301, has demonstrated efficacy in a number of different tumor types, and has been a useful tool in visualizing and characterizing cancer *in vivo*. Typically, the probe is injected via the tail vein, then allowed to accumulate in tumors. Initially, the probe is present in all tissues, then at approximately 24 hours post injection the tumor exhibits more signal than the surrounding tissue. **Figure 2-1a** shows LS301 injected into a HT1080 (human fibrosarcoma) xenograft model. At short time points there is no contrast between the tumor and the surrounding tissue, however at 24 hours post injection the contrast is at a maximum **Figure 2-1c**. In this study, by 96 hours post injection there was minimal contrast remaining between the tumor and the surrounding tissue.

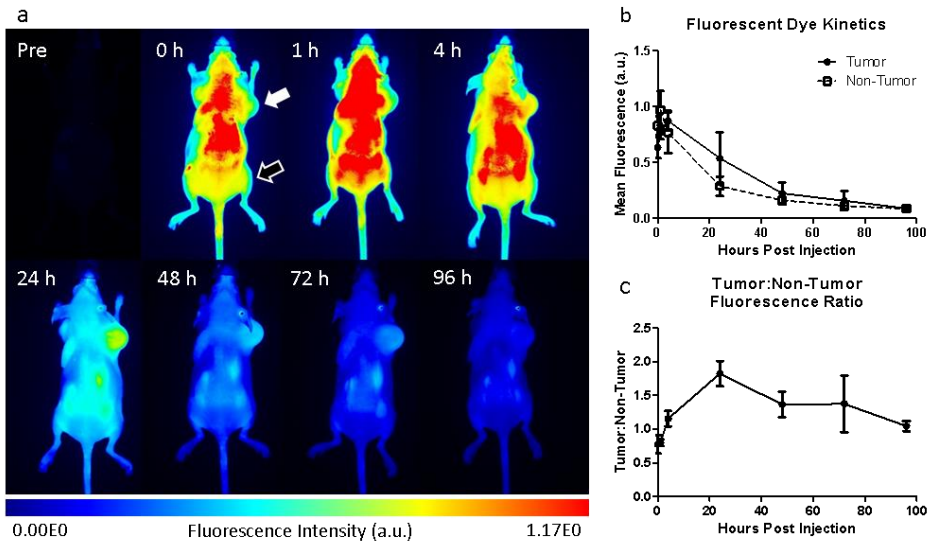

Figure 2-1: a) Time course images of a HT1080 xenograft model injected with a targeted fluorescent dye, from pre-injection to 96 hours post injection. Tumor identified by the white arrow and non-tumor region identified by the outlined arrow. b) Fluorescent dye *in vivo* kinetics, with 24 hours post injection showing largest difference between tumor and non-tumor regions. c) Tumor to non-tumor ratio showing maximum contrast at 24 hours post injection.

2.2 Skin Cancer Imaging

LS301 has been previously used in various tumor types, however we were interested in imaging those that were on surfaces that were readily accessible for optical imaging. Skin and mucosal sites were an attractive target because of the ability to image non-invasively or minimally invasively.

We used an orthotopic model of SCC-12 cells (human cutaneous squamous cell carcinoma) to develop methods for skin cancer identification and characterization. The SCC-12 xenografts were generated by injecting $2.5x10^6$ cells into 6-week-old female athymic nude mice in the bilateral shoulder and flank regions within the intradermal compartment. All studies were in compliance with the Washington University Animal Welfare Committee's requirements for the care and use of laboratory animals in research.

NIR fluorescence images were obtained using the Pearl Small Animal NIR fluorescence imaging system (LICOR Biosciences, NE, USA), ex/em 785/820 nm. LS301 was injected via the tail vein (0.40 mg/kg), and animals were imaged at 24 hours post injection (**Figure 2-2a**). We quantified the *in vivo* fluorescence signal, and the tumors exhibited a higher signal than the skin regions at 0.26 ± 0.012 to 0.42 ± 0.044, respectively (**Figure 2-2b**). After the conclusion of our study we sacrificed the mouse and confirmed the presence of our fluorophore in the tumor tissue. **Figure 2-2c** shows the tumor histology, and **Figure 2-2d** shows the fluorophore distribution within the tumor. **Figure 2-2e** shows the magnified view of the fluorophore along with skin cancer cells.

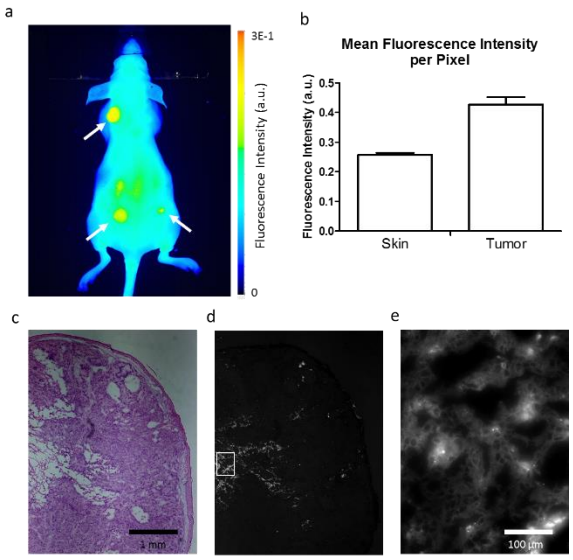

Figure 2-2: a) Fluorescence image of LS301 injected into a SCC-12 skin cancer model. Tumors visible at 24 hours post injection (white arrows). b) *In vivo* fluorescence signal for the tumor and non-tumor regions. c) Histology of a tumor section at 4x magnification. d) Fluorescence intensity of the histological section shown in (c). e) 40x view of a region with high fluorescence.

2.3 Bladder Cancer

We were also interested in imaging bladder cancer as cystoscopy is an optical method that is routinely used clinically to diagnose and monitor patients with bladder cancer. An endoscope could be utilized to image fluorescence contrast from within the bladder to detect the presence of

a tumor. We used a MCB6 (murine bladder cancer) model to test the ability of LS301 to identify bladder tumors. Bladder tumor cells were induced in one mouse, then the cells were harvested and injected into the side of another different mouse. LS301 was injected via the tail vein (0.40 mg/kg), and animals were imaged at 24 hours post injection. **Figure 2-3a** shows *in vivo* tumor contrast and **Figure 2-3b** shows the quantification of the tumor and non-tumor fluorescence intensity. As in the case of the fibrosarcoma (HT1080) and skin cancer (SCC-12) imaging, the bladder cell tumors showed greater contrast than the surrounding tissue. **Figure 2-3c** shows the ex vivo bio-distribution of LS301, with the values quantified in **Figure 2-3d**. The tumor showed higher signal than the surrounding subcutaneous tissue and muscle, and we were interested in determining if the tumor would exhibit contrast as compared to the normal bladder tissue. We harvested the bladder and imaged it alongside the tumor. In this case we saw higher signal in the tumor as compared to the bladder **Figure 2-3e**. This finding indicates that fluorescence contrast could potentially be used to image bladder tumors via an intravenously injected agent that localizes to tumors.

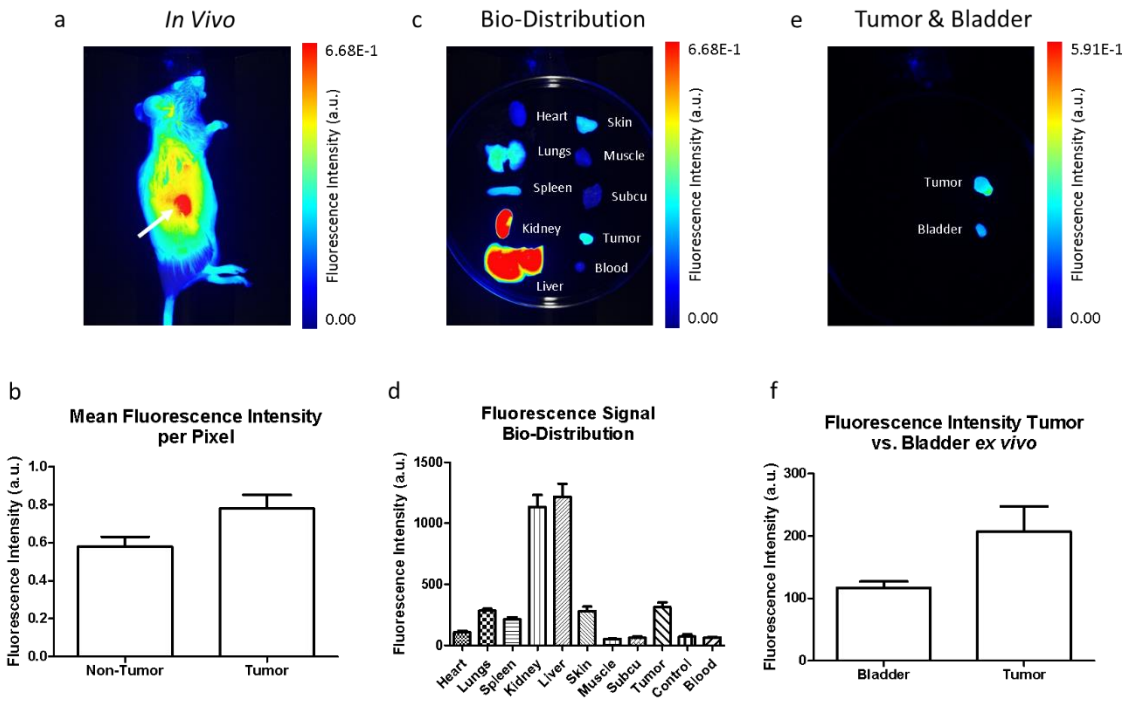

Figure 2-3: a) Fluorescence image of LS301 injected into a MCB6 bladder cancer model at 24 hours post injection. b) *In vivo* fluorescence signal for the tumor and non-tumor regions. c) Fluorescence image of the bio-distribution of the signal in various organs. d) Quantification of the bio-distribution. e) Fluorescence image of the tumor and bladder showing higher signal in the tumor as compared to the bladder. f) Quantification of the tumor and bladder fluorescence signals.

2.4 Conclusions

We demonstrated that LS301 is adequate to generate tumor contrast *in vivo* for tumor visualization in a variety of tumor types. While this is valuable for identifying tumors, other data such as tumor burden and tumor characteristics remain unknown when solely using fluorescence intensity. In the upcoming chapters we investigate using fluorescence contrast to obtain additional data about the tumor, such as tumor volume and tumor depth.

Chapter 3 :

Gradient-Based Algorithm for Determining Tumor Volumes in Small Animals Using Planar Fluorescence Imaging Platform

3.1 Introduction

Compared with conventional imaging modalities such as computed tomography (CT), positron emission tomography (PET), and magnetic resonance imaging (MRI), optical imaging of small animal models can serve as a high-throughput, accurate, low learning curve, and low-cost method for measuring pathophysiologic parameters using non-ionizing radiation. As a result, thousands of laboratories worldwide have adopted planar optical imaging as the preferred imaging modality for assessing drug efficacy, developing new molecular imaging probes, and understanding the molecular basis of pathophysiological processes.

Tumor volume assessment is a typical primary output in interventional studies investigating new therapies. Preclinical tumor volume is most often estimated using calipers to measure the length and width of a tumor, and then using the equation $V = 0.5 \times L \times W^2$ to report tumor volume, where V is the tumor volume, L is the tumor length, and W is the tumor width. This approach is simple, fast, and fairly reliable [5]. However, the potential for user dependent variability introduces intractable errors in data analysis [6,7]. When the tumor grows in an infiltrative manner and invades the underlying tissue, identification of the tumor margin using calipers presents additional challenges. Moreover, if a measurement is not taken for a given day, the data cannot be obtained at a later time.

Using fluorescence imaging to determine tumor volume has been a challenge, largely due to the attenuation of light within tissue. For *in vivo* imaging, light is reflected, scattered, and absorbed as it passes through a heterogeneous medium, thereby obscuring the true boundary of the target object within the tissue. There are two ways to solve the inverse problem of locating the boundaries of a fluorescent target: mathematically and empirically. Mathematical approaches have been developed that are based on stochastic modeling of light propagation through a medium.

Three dimensional quantitative fluorescence imaging has been accomplished through using fluorescence molecular tomography (FMT) to measure tumor geometry [8,9]. The drawback of FMT is that it requires a complex setup that is not accessible to most biological laboratories. Additionally, the process necessary to extract the signal can be computationally intensive and time consuming, limiting real-time feedback.

Because of the complexity of FMT, planar optical imaging platforms that utilize empirical methods have become the hallmark of most biological imaging studies. Empirical approaches have been successfully adopted for tumor cell viability testing with technologies such as bioluminescence imaging (BLI) [10]. BLI projects light generated from the interaction of a bioluminescent enzyme with its substrate to the skin surface, and modern cameras can use this to detect cancer cells with exceptionally high sensitivity. However, tumor volume measurements obtained from BLI are anecdotal because the method measures viable tumor cells, which does not represent the actual tumor volume. As tumor cells proliferate, some of the daughter cells do not express the reporter protein, which confounds the tumor volume assessment.

In this study, we sought to develop a simple optical method for determining tumor volume from planar fluorescence images. Currently, the inverse problem in tissue optics can be solved empirically if the target geometry dimensions are known, and parameters to compensate light attenuation are determined. Because small animal imaging uses similar tumor models to screen for therapies, the empirical approach can be employed with very few parameters necessary to obtain an adequate fit between the calculated volume and the actual volume. By using a cancer-targeting molecular probe, we were able to investigate the application of our model to diverse tumors. Compared to conventional methods, our new PV-TVA approach was simpler and more accurate.

3.2 Methods

3.2.1 Tumor Models

We used two subcutaneous tumor models in this study: HT1080 (human fibrosarcoma) to develop and test the algorithm, and 4T1-Luc (murine mammary cancer) to compare the algorithm to BLI, which requires luciferase-expressing cells. HT1080 xenografts were generated by the subcutaneous injection of $3x10^6$ cells into 8-week old female athymic nude mice in either the right shoulder or the left flank region. The right shoulder region was used to determine the optimal time point for imaging (n = 2), and the left flank region was used for the development of the algorithm (n = 3). 4T1-Luc xenografts were generated by the subcutaneous injection of $1x10^6$ cells into 6-week old female Balb/c mice in the left flank region (n = 5). The longitudinal therapeutic study was conducted using the HT1080 flank model (n = 4). Tumors were allowed to develop until palpable, and length and width measurements were taken using calipers. Mice were anesthetized with isoflurane (3-5%) during all experimental procedures, including inoculation of tumor cells, caliper tumor measurement, and image acquisition. All studies were conducted in compliance with the Washington University Animal Welfare Committee's requirements for the care and use of laboratory animals in research.

3.2.2 Fluorescence Imaging Studies

For imaging studies, the mice were injected with a 0.40 mg/kg or 0.80 mg/kg dose of LS301[11]. LS301 was suspended in 100 μL of DPBS and injected into the mouse xenografts through lateral tail vein injection. Using excitation and emission wavelengths of 785 nm and 810 nm, respectively, fluorescence imaging was performed with the Pearl Small Animal Imaging System (Li-Cor Biosciences, Inc., Lincoln, NE). Animals were imaged from a dorsal view at either 0, 1, 4, 24, 48, and 96 hours post injection, or a single image at 24 hours post injection. After the final

imaging time point the mice were euthanized and the skin was reflected from the tumor surface. *In situ* length and width were measured using calipers and the volume was calculated using the equation, $V = 0.5 \times L \times W^2$. The tumors were then carefully excised using the tumor capsule as a guide, and the tumor volume was measured using a water displacement method. Grayscale fluorescence images from the 800 nm channel were output in jpg format using the PearlCam software (Li-Cor Biosciences, Inc., Lincoln, NE). The image processing and analysis were conducted via custom code written in MATLAB (Mathworks, Inc., Natick, MA).

3.2.3 Bioluminescence Imaging Studies

Five mice with 4T1-GFP-FL xenografts received intra-peritoneal injection of 150 mg/kg D-luciferin in PBS (Gold Biotechnology, St. Louis, MO) for BLI. Mice were then imaged at 10 minutes under isoflurane anesthesia with an IVIS 50 (PerkinElmer, Waltham, MA; Living Image 4.3, 1 or 10 second exposures, bin8, FOV 12 cm, f/stop1, open filter). The total photon flux (photons/sec) was measured from software-defined contour regions of interest (ROIs) over the tumors using Living Image 2.6. Bioluminescence from viable tumor cells was used to estimate tumor burden.

3.2.4 Longitudinal Therapeutic Studies

One of the benefits of using the PV-TVA to measure tumor volume is to determine the efficacy of therapy over time. To investigate the treatment response, we obtained longitudinal images using an HT1080 xenograft model. Four mice were injected with a 0.40 mg/kg dose of cypate-cGRD via the tail vein, once a week for 4 weeks. In two of the mice, doxorubicin was administered at a dose of 10 mg/kg after a baseline image was obtained. The doxorubicin was dissolved in DMSO, and then mixed in DPBS to obtain the desired dose in 100 μL of solution.

3.3 Results

3.3.1 Gradient-Based Algorithm Development

The Pearl Small Animal Imaging System has the ability to create images using a color jet map, grayscale, and numerous other visualization options. The color jet map image provides for a rapid method to visualize tumor contrast from the surrounding tissue, however slight changes in the intensity scale may produce significant changes in the apparent tumor outline (**Figure 3-1A**). Color images rely on the user's visual interpretation to create the best guess for how to threshold the tumor boundary, therefore leading to variability. A more reliable approach was to reduce the need for perceptive input from the user. When analyzed, grayscale images produced a consistent tumor region as the contrast settings were varied (**Figure 3-1B**). To further standardize the approach, the grayscale images for output were selected by increasing the maximum intensity in the image until just below the point where the image became saturated. This technique allowed for maximum contrast between the signal and background without losing information in the image.

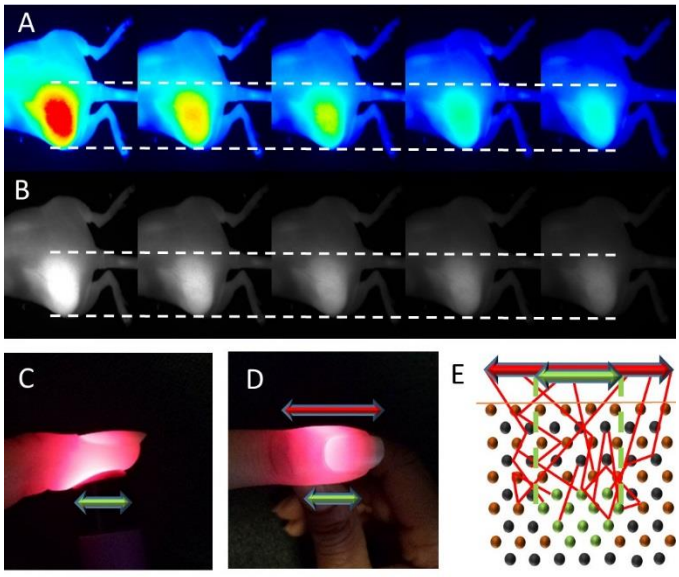

Figure 3-1: A) Color images of a fluorescent tumor and surrounding tissue with the maximum intensity set to different values (from left to right): $1.0x10^0$, $1.5x10^0$, $2.0x10^0$, $2.5\ x10^0$, and $3.0x10^0$ a.u. B) Grayscale images of the same tumor set to the same maximum intensity values as (A). C

and D) Side and top images of light scattering in tissue, with the apparent width of the source at the top of the finger (red arrow) larger than the actual width of the light source (green arrow). E) Illustration of a light emitting fluorescent tumor (light source) within scattering medium. The red arrow shows the observed width at the surface of the tissue, and the green arrow shows the actual width of the tumor within the surrounding tissue.

Even with the consistent tumor image produced using grayscale, the light attenuation due to tissue scattering still remained a confounding factor in determining the true tumor outline. This is similar to what is observed in **Figure 3-1C** and **Figure 3-1D**, where the light source is smaller than the observe light after it passes through tissue. Image processing allowed for an algorithm to account for the amount of scattering for a given tissue system. Because xenograft models of a particular tumor type were relatively consistent, the parameters to account for scattering were set for all other samples once they were known for a given tumor model.

To initiate the PV-TVA, two points were selected by the user approximately along the horizontal axis of the tumor from the grayscale image. This line was long enough to go from uninvolved tissue, through the tumor, and into back to uninvolved tissue (**Figure 3-2A**). An intensity curve was created using the intensity values from the pixels along the length of the line (**Figure 3-2B**). The slope of the intensity curve was calculated for each point along the line using the subsequent number of pixels that the user specified (user input parameter) (**Figure 3-2C**). Using a larger number of pixels to calculate the slope acted as a smoothing operation, making the algorithm less sensitive to local variability. Once the slopes were calculated along the length of the line, the maximum and minimum slope values were identified as the inflection points of the intensity plot along the line (**Figure 3-2D**). The average of these intensity values was used to determine the average value of the edge of intensity observed at the surface of the skin (**Figure 3-2E**). All values above this intensity were found within the user selected region (**Figure 3-2F**). Once this procedure was completed, it became evident that the scattered light caused the apparent

tumor outline to be larger than the actual tumor outline, as was later verified using post mortem *in situ* measurements.

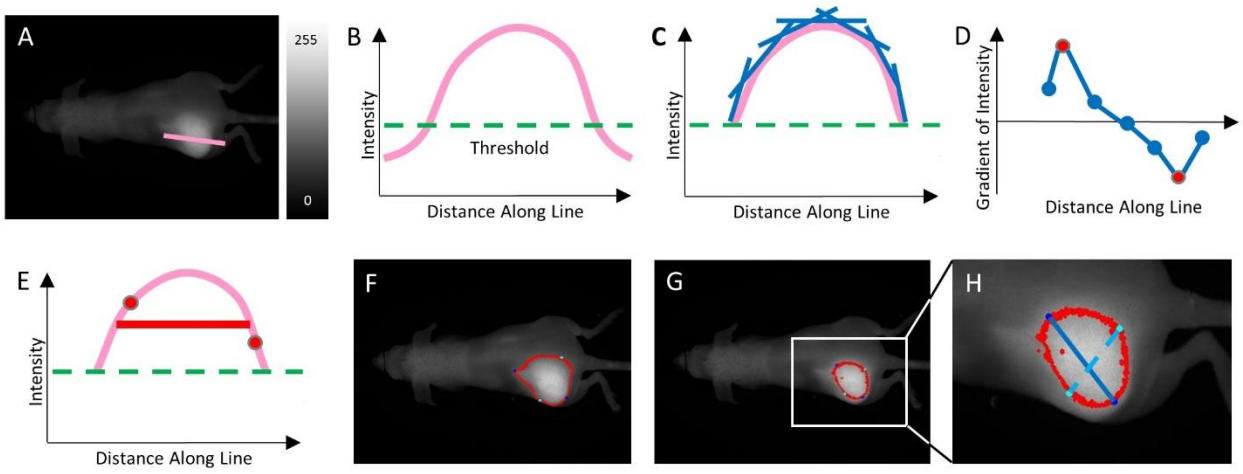

Figure 3-2: A) Input image with an illustrated user selected line for region of interest identification. B) Intensity profile along the line (pink curve) with a *Threshold* value (green dashed line). C) Moving slope (blue lines) of the intensity profile calculated along the line. D) Plot of the moving slopes (blue points) calculated along the line, with the inflection points of the intensity (red points). E) Two inflection points identified (red points) and the average used for the tumor boundary determination (red line). F) Algorithm determined tumor outline overlaid on image without using the *Threshold* value. G) Algorithm determined tumor outline overlaid on image using the *Threshold* value to account for scattering. H) Tumor length (blue solid line) and tumor width (cyan dashed line) overlaid on image.

To account for this variability, a threshold value was created to decrease the outline of the tumor with the verified assumption that the scattered light contributes to increasing the imaged tumor outline dimensions. For example, a *Threshold* value of 0.25 would select the highest 25% of values that were along the user selected line and calculate the inflection points based on only those values. Once the threshold was determined, the slopes of the intensity values were calculated using only the values that fell above that threshold value (**Figure 3-2C**). Adding a *Threshold* parameter to the PV-TVA resulted in a more accurate identification of the tumor from the images (**Figure 3-2G**). The threshold was defined in **Equation 3-1** as:

$$Threshold = I_{max} - Percent(I_{max} - I_{avg}) \quad \textbf{Eq. 3-1}$$

Where *Threshold* was the minimum intensity value accepted as potentially originating from tumor tissue, I_{max} was the maximum intensity value originating from the mouse, I_{avg} was the average intensity value for the entire mouse, and *Percent* was a user input value specific to the system being analyzed.

Percent was chosen as the user input value rather than *Threshold*, because inputting the *Percent* parameter allowed for the contrast of the intensity between the tumor and the surrounding tissue to be incorporated into determining the threshold value. This approach balanced the need for tuning the threshold based on the system properties (the tumor morphological appearance, dye kinetics, and dye attenuation properties at the emission wavelength), with preserving the relationship of the tumor contrast within the image. By changing the *Percent* value, this tunable threshold allowed for versatility of the algorithm for different biological systems and dye concentrations. The *Percent* value was initially determined by using the post mortem tumor volume value from one mouse, and then that value was subsequently used to analyze the images for all of the following mice. This *Percent* value was validated after the study by running the PV-TVA at various *Percent* values, and then comparing each resultant tumor volume to the actual value (**Figure 3-3E**). The validation confirmed that the initially selected *Percent* was valid for all of the tumors of this type.

The final tumor volume was calculated by determining the length and width of the outlined tumor (**Figure 3-2H**). The length was defined as the longest distance between two points on the outline. The width was defined as the distance between the two points, on opposite sides of the line defining the length, with the maximum perpendicular distance from the line defining the length. The volume was calculated using the same equation as the caliper method.

There was a tradeoff between versatility and variability when conducting automated image analysis. As a result, the PV-TVA had some inherent variability based on the initial two points that the user selected. Allowing the user to select the initial two points allowed for the independent analysis of multiple tumors on the same mouse, and was therefore an essential part of the algorithm training. The potential variability from this was compared to the variability in the tumor volume caliper measurement method. The PV-TVA was run ten times for a given set of images, with the user selecting different input points, to understand the precision and accuracy of the calculated values. The tumors were measured using calipers ten times by two users who were blinded to the previous readings to capture the inherent variation in measurements using calipers.

3.3.2 Tumor Volume Calculations

Three HT1080 tumors were analyzed to test the capabilities of the PV-TVA. We used caliper measurements as our control, and blinded the user to the previous caliper measurement. To capture inter-user variability, two users measured each tumor five different times, for a total of ten measurements. **Figure 3-3A** shows the caliper measured tumor volumes separated by user. T1 and T3 produced similar results, however T2 showed a difference in caliper calculated volume between users ($p = 0.010$). We binned the caliper measurements of both users for each tumor and repeated the PV-TVA 10 times for each tumor. The results were compared to the actual tumor volume obtained from the volume of water displaced by the tumor, and the deviations from the calculated vs. actual tumor volume were compared for the caliper method and the PV-TVA method (**Figure 3-3B**). The accuracy of each method was assessed by calculating the average of the absolute value of the deviations for the caliper and PV-TVA methods. The caliper average deviation was 18% (204.34 ± 115.35 mm^3) and the PV-TVA average deviation was 9% (97.24 ± 70.45 mm^3), $p < 0.001$ (**Figure 3-3C**). Comparison of the precision of each method using the standard deviations

of the ten calculations showed that the average standard deviations for the methods were 11% (131.95 mm^3) and 8% (96.51 mm^3) for the caliper and the PV-TVA, respectively (**Figure 3-3D**).

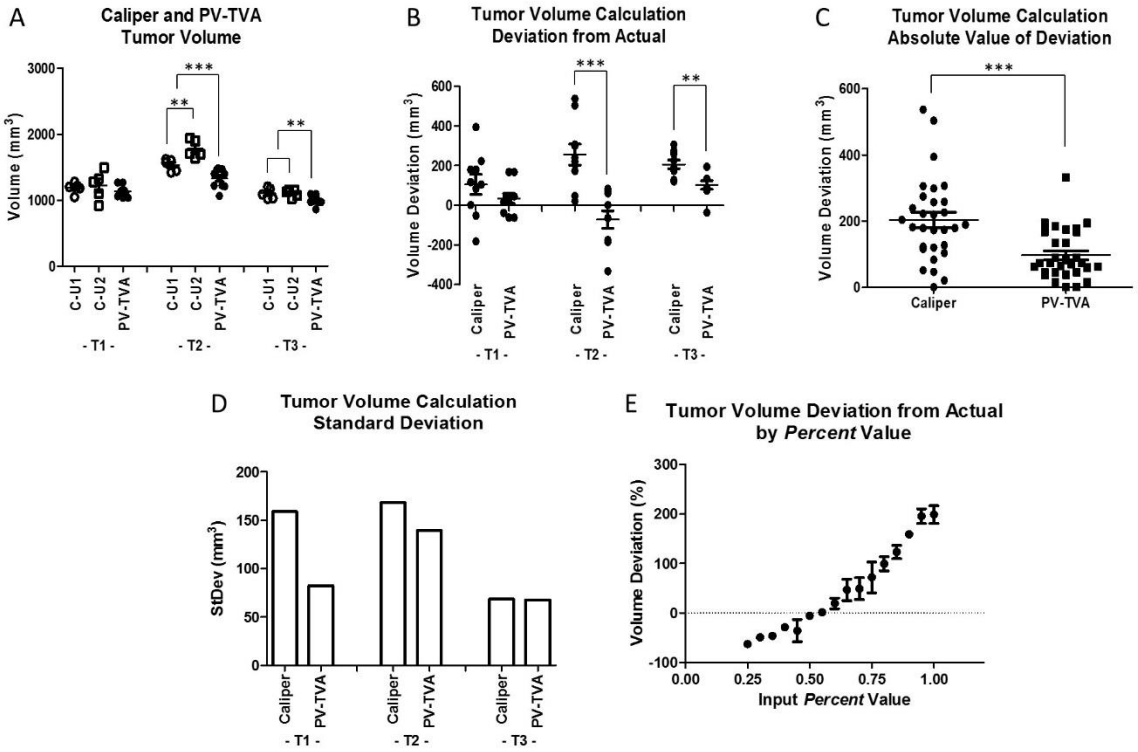

Figure 3-3: A) Tumor volumes for three HT1080 tumors (T1, T2, and T3) as determined using the caliper measurement method for two users (C-U1 and C-U2), and the PV-TVA (*Percent* = 0.55). B) Tumor volume calculation deviations from the actual volume as measured using post resection water displacement. C) Absolute value of the deviations of the tumor volume calculation methods to measure the accuracy. D) Average standard deviations of 10 measurements for each of the three tumors to measure the precision. E) Validation for the *Percent* value selected to calculate tumor volume. * ($p < 0.05$), ** ($p < 0.005$), *** ($p < 0.001$).

The *in situ* length and width were measured by reflecting the skin and measuring the tumor prior to complete resection. Our result showed that the absolute value of the length deviations from the *in situ* dimensions were on average 10% (1.21 ± 0.44 mm) for the calipers and 5% (0.68 ± 0.21 mm) for the PV-TVA, $p < 0.001$ (**Figure 3-4A** and **Figure 3-4B**).The absolute value of the width deviations were on average 8% (0.81 ± 0.48 mm) for the calipers and 5% (0.55 ± 0.31 mm) for the PV-TVA, $p = 0.001$ (**Figure 3-4C**).

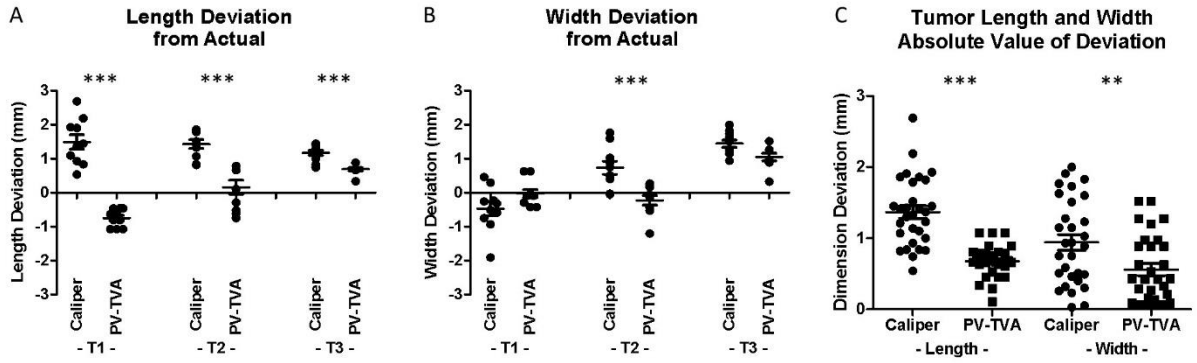

Figure 3-4: A) PV-TVA Length deviations for three HT1080 tumors (T1, T2, and T3) from the *in situ* length measurement. The algorithm was run 10 times for each image. B) Width deviations from the *in situ* width measurement. C) Absolute value of the deviations of the length and width for both calculation methods to measure the accuracy.

We next examined how this algorithm compared to other planar optical methods for determining tumor burden. BLI was conducted on a set of 4T1-Luc tumors and the results were compared with those of the caliper and PV-TVA methods. Because BLI does not give a tumor volume, the measurements for five tumors were all normalized to the value of the first tumor (T1). This analysis allowed us to compare the trend in tumor burden between the different tumors. The same normalization to T1 was done using the actual tumor volumes as measured by the water displacement method, and for the caliper and PV-TVA methods. The analysis revealed that the BLI measurements had a similar trend to the actual tumor volumes (**Figure 3-5B**), except for the case of T3 where the BLI would have predicted a much smaller tumor than what was observed (**Figure 3-5A**). In this case, the PV-TVA predicted a similar burden as the ground truth measurement obtained using the water displacement method. The deviations of each normalized value from the actual normalized value were calculated for the BLI, caliper, and PV-TVA methods (**Figure 3-5C**). When comparing the deviations, BLI had an absolute value average deviation of 36% of T1, the caliper method 19% of T1, and the PV-TVA 10% of T1. Normalization for

comparative analysis allowed for the comparison of trends, but did not give insight into the absolute deviations without extrapolation. **Figure 3-5D** shows the signed deviation from actual for the caliper and the PV-TVA methods. The average absolute value of the deviations was 37% (112.9 ± 93.62 mm^3) for the calipers, and 18% (60.52 ± 62.65 mm^3) for the PV-TVA, p = 0.105. The *Percent* value for this tumor model was determined to be 0.25. The PV-TVA was run at various *Percent* values and compared to the actual volume for validation (**Figure 3-5E**).

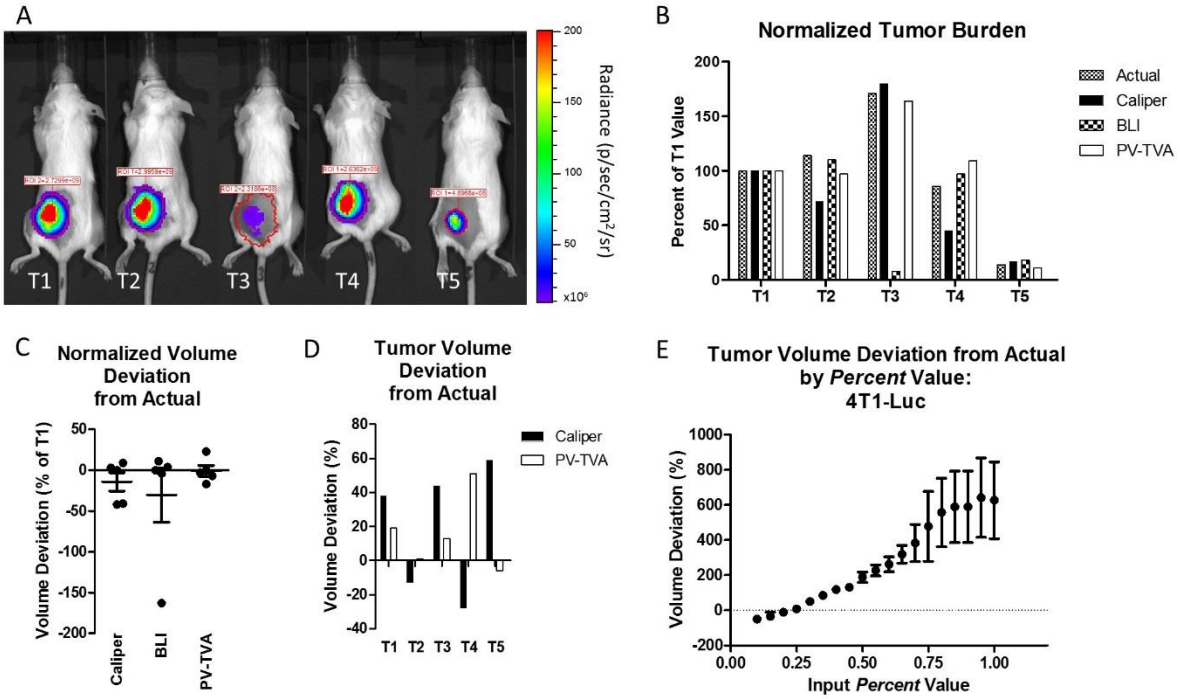

Figure 3-5: A) BLI images for five 4T1-Luc tumors (T1, T2, T3, T4, and T5). B) Normalized tumor burden values for the actual volume, caliper, BLI, and the PV-TVA. All measurements were normalized to the T1 value for the specific type of measurement. The PV-TVA result was obtained using *Percent* = 0.25. C) Normalized tumor volume deviation from actual as a percentage of T1 for each method. D) Tumor volume percent deviation from actual for the caliper and PV-TVA methods. E) Validation for the *Percent* value selected to calculate tumor volume using post mortem tumor volumes. The tumor volume deviations were calculated at various *Percent* values for the 4T1-Luc tumor model.

We next examined the ability of the PV-TVA to monitor the tumor response to a given treatment. We used the HT1080 tumor model because it previously demonstrated a treatment

response to doxorubicin. We took a baseline NIR image of each of the mice to establish the pre-treatment tumor volume. Two of the mice were treated with doxorubicin, and all of the mice were followed for three additional weeks. The NIR images showed the range of tumor-to-background signals obtained using planar fluorescence imaging (**Figure 3-6A**). Because the PV-TVA calculated a threshold based on a combination of a user input *Percent* value and the inherent image contrast, the PV-TVA was able to calculate the tumor volume, despite the varied appearance of the images, in all but one of the images (T4-Wk2). In the case of the image that did not produce a solution, there was insufficient contrast at the location of the tumor to calculate a tumor volume. To account for various initial tumor volumes at the time of treatment, the tumor response was calculated as a percentage of the pre-treatment volume. At each time point the PV-TVA was run three times. The mice treated with doxorubicin demonstrated a suppression of tumor growth over time as compared to the control mice (**Figure 3-6B**). This result was obtainable even with varying image properties such as tumor signal and average mouse signal (**Figure 3-7**). We also confirmed that the *Percent* value used to calculate tumor volume did not change as a result of multiple fluorophore injections. The PV-TVA was run at the final time point (fourth fluorophore injection), for various *Percent* values, to confirm that the original HT1080 *Percent* value remained valid (**Figure 3-6C**). A *Percent* value of 0.55 produced the smallest deviation from the actual value, consistent with the single time point study using an HT1080 tumor model (**Figure 3-3E**).

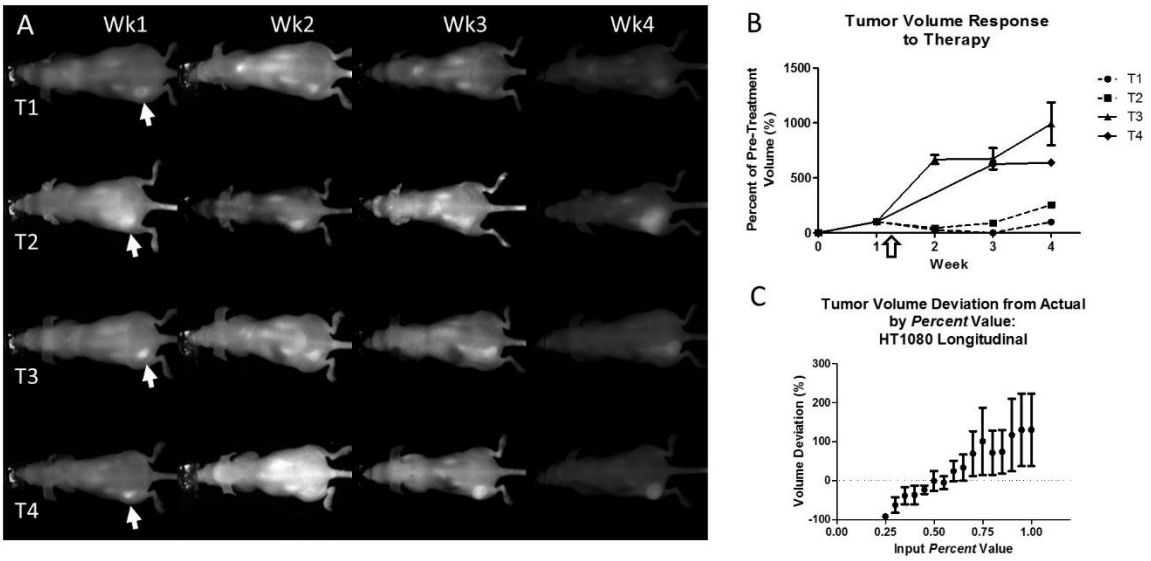

Figure 3-6: A) NIR images of four HT1080 mice with left flank tumors (T1, T2, T3, and T4) indicated by the arrows. Each mouse was imaged once a week for 4 weeks. Images had different tumor signals, average mouse signals, and tumor to mouse contrast. B) Tumor volumes over time normalized to the pre-treatment volume. Mice treated with doxorubicin (dashed line) had suppressed tumor growth as compared to the control mice following the administered dose (white arrow). C) Validation for the *Percent* value used in the HT1080 longitudinal treatment study after multiple fluorophore injections over time (*Percent* = 0.55).

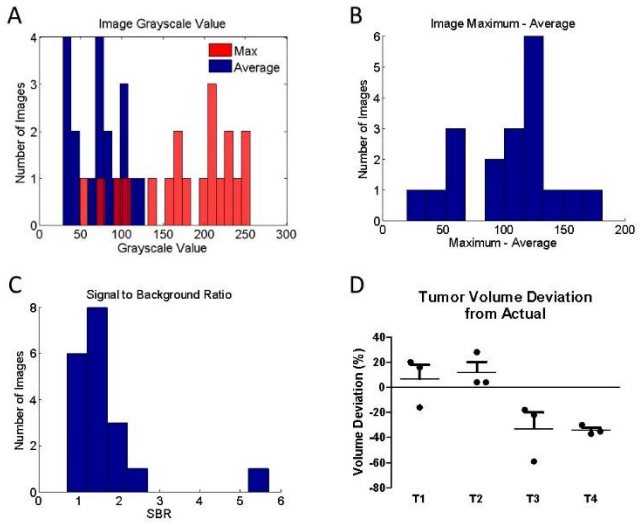

Figure 3-7: A) Maximum and average grayscale values for the images shown in Figure 5A. B) Maximum minus average grayscale values for each of the images demonstrating the range of values analyzed that produced a result. (T4-Wk2 is not included because there was inadequate contrast to generate a tumor volume). C) Signal to background ratios for each of the images.

(Assumes that the maximum value is the signal and the average is the background. Calculated: [M-A]/A, where M is the maximum and A is the average.) D) Tumor volume deviation from actual for each mouse at Week 4. The PV-TVA was run 3 times for each tumor and the percent deviation was determined using the post mortem water displacement method.

3.4 Discussion

When determining tumor volume, calipers are cost effective and relatively straightforward. However, they introduced variability that was in excess of what we observed from our PV-TVA data. Using an algorithm-based approach minimized the user induced measurement variability. The PV-TVA worked by allowing the user to input a fluorescence image, converting the image to a matrix of grayscale values, using user selected points to determine the region of interest, and then using a gradient based calculation to calculate the tumor volume (**Figure 3-8**). The gradient based calculation accounted for light scattering of fluorescence in a given system, allowing the algorithm to select the apparent tumor outline in a number of different systems. By combining the inherent image properties, along with a user input parameter, the tumor volume was reproducibly calculated.

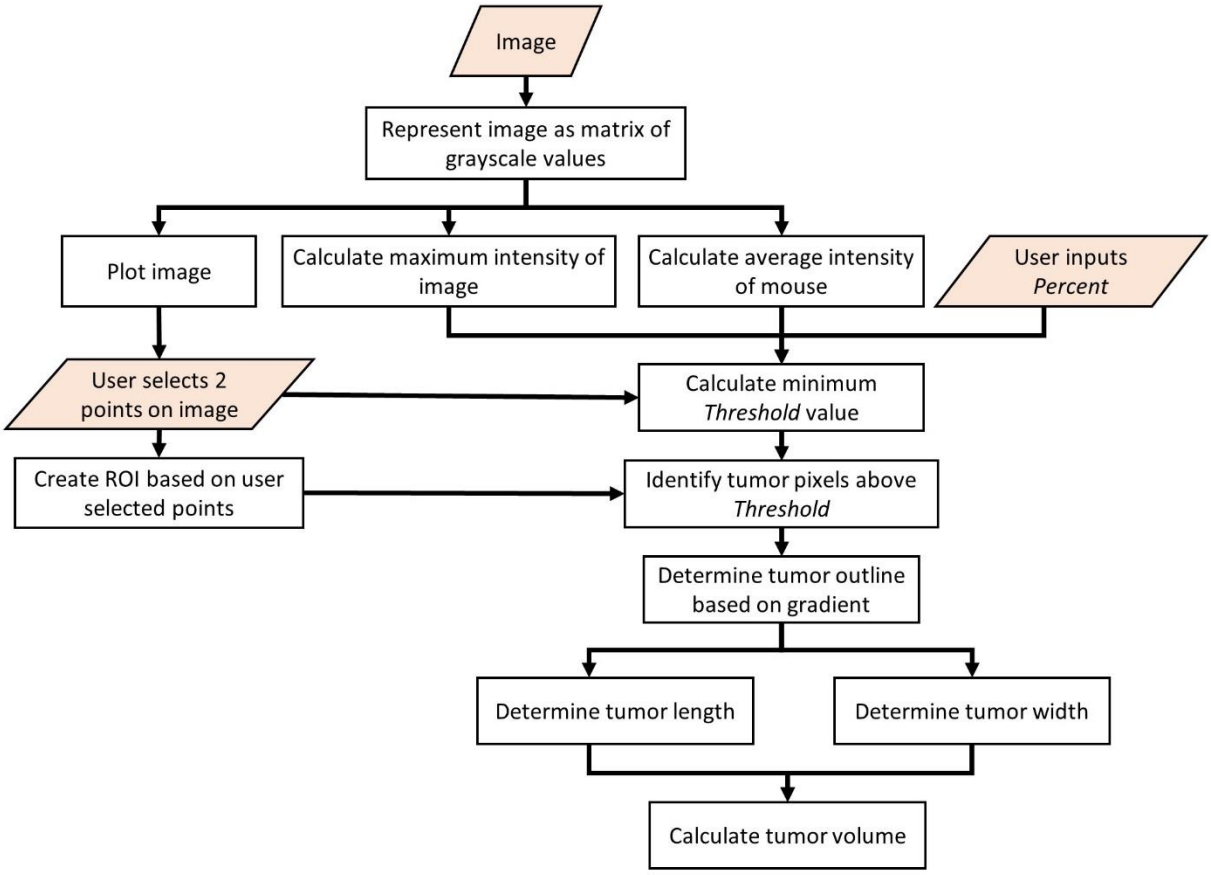

Figure 3-8: Planar view tumor volume algorithm (PV-TVA) schematic. The user inputs the image, *Percent* value, and selects two points on opposite sides of the tumor. The algorithm then calculates the tumor volume based on the gradient along the line connecting the two points the user selected.

The user input value, *Percent*, was be determined for different systems by acquiring empirical data. The *Percent* value used for the group of 4T1-Luc tumors in **Figure 3-5** was different than the value used in the HT1080 group of tumors in **Figure 3-3**. It was important to note that the injected fluorescent probe concentration also differed between the groups. This emphasized the versatility of the PV-TVA, along with the importance of calibration for a given system to obtain the ideal *Percent* value. Once this parameter was obtained, the value was used on subsequent images. Moreover, we demonstrated that this parameter remained consistent even after multiple fluorophore injections.

In addition to reducing variability, using an imaging approach to measure tumor volume had other advantages. Obtaining an image over a direct measurement allowed for retrospective analysis and calculations to be made after the study was completed. The PV-TVA could be used with any targeted fluorescent probe with enhanced signal within the tumor making it highly versatile.

A goal of this study was to provide a rapid and retrievable quantitative analysis method using planar fluorescence images. We illustrated the application of the PV-TVA in subcutaneous tumor models because of the wide use of these models in cancer research. The PV-TVA performed better than calipers, and as well as, or better than BLI for optically measuring and tracking tumor volume.

3.5 Conclusions

We demonstrated that pre-clinical tumor models could be monitored via fluorescence imaging using the quantitative output of tumor volume. The development of our PV-TVA allowed for planar imaging to accurately measure tumor volume without the need to measure tumors. The goal of the analysis was to develop a tool to track tumor volumes in pre-clinical settings, and a limitation of the approach was the need to for *a priori* information to determine the appropriate *Percent* threshold. *A priori* information is possible for pre-clinical studies, however it is not always available when techniques are translated to clinical applications. In order to understand tumor volume in a wider array of applications, both the tumor boundary and the tumor depth are necessary.

In the next chapter we investigated using fluorescence to obtain the tumor boundary without needing to know the threshold value prior to the application. The ability to identify tumor

boundaries in diverse situations, along with the tumor depth, would allow for fluorescence-based volumetric calculations without the need for the volume approximation equation currently used in pre-clinical tumor evaluation.

Chapter 4 :

Enhancing *in vivo* tumor boundary delineation with structured illumination fluorescence molecular imaging and spatial gradient mapping

4.1 Introduction

Surgical resection is the primary cancer treatment for many tumor types. Cancer is difficult to distinguish from adjacent non-tumor tissues, resulting in inadequate margins of resection and a high rate of repeat operations.[12] Surgical resection of tumors in the head and neck can be complicated by proximity to vital structures and could benefit from intraoperative fluorescence molecular imaging strategies.[13,14]

Intraoperative fluorescence imaging utilizing harmless light, and digital camera technology, to rapidly measure fluorescence over a large field of view. Real-time tumor localization can improve procedural outcomes.[15,16] Accurate tumor boundary determination is essential in resection of head and neck cancer tumors, where preservation of healthy tissue is vital for the essential tasks of eating and breathing.[13]

Fluorescence imaging is depth-limited due to signal attenuation from scattering and absorption. Attenuation results in signal weighting that scales exponentially with depth such that even low levels of dye in overlying tissues can obfuscate tumor-specific contrast.[17,18] Signal attenuation from surface weighting of fluorescence is compounded by reflected excitation light, of which even a few percent bleed-through can significantly confound fluorescence quantification.[19] Elimination of signal from overlying tissue is necessary to improve cancer-specific fluorescence contrast and better define tumor boundaries. Therefore, we investigated structured illumination techniques to separate the fluorescent signal from a head and neck cancer tumor and overlying healthy tissue.

Structured illumination microscopy (SIM) employs patterned illumination and image deconvolution to enhance axial resolution by rejecting out of focus light.[20] Optical sectioning with structured illumination, as demonstrated by Neil et al., uses fluorescence excitation in striped

patterns to isolate in-plane vs. out-of-plane fluorescence.[21] Thus planar imaged light (I_0), can be de-convolved into the spatially modulated signal (I_s) and the constant, unmodulated signal (I_C):

$$I_0 = I_S + I_C \qquad \textbf{Eq. 4-1}$$

Tissue acts as an optical low-pass filter, such that patterns projected on the surface are effectively blurred within a few millimeters of the surface.[22,23] Using striped patterns of different frequencies allows for effectively adjusting the light that is allowed to pass through the tissue, and therefore we can selectively eliminate fluorescence of different depths by modulating the signal. When illumination patterns are sequentially phase-shifted by $2\pi/3$, (I_1, I_2 and I_3), I_0 and I_S can be de-convolved according to **Eq. 4-2** and **Eq. 4-3**, respectively:

$$I_0 = (I_1 + I_2 + I_3)/3 \qquad \textbf{Eq. 4-2}$$

$$I_S = \frac{\sqrt{2}}{3}\sqrt{(I_1 - I_2)^2 + (I_2 - I_3)^2 + (I_3 - I_1)^2} \qquad \textbf{Eq. 4-3}$$

The peak-to-trough distance of the excitation pattern is equivalent to fixed source-detector separation of diffuse optical imaging[24,25], allowing for selective imaging of the desired fluorescence signal.[26] Therefore, the non-depth dependent signal coming from the tumor (I_C), can be isolated by subtracting of the unwanted plane of the shallow signal (I_S) from total fluorescence signal (I_0). Because the I_0 obtained in conventional planar fluorescence imaging contains both the unwanted background fluorescence (I_S), along with the tumor signal (I_C), the tumor to background ratio is reduced. Extracting the I_C signal from the total I_0 signal more effectively isolates the tumor fluorescence.

Herein we investigated fluorescent molecular imaging for identifying tumor location and boundaries of a mouse model of solitary extramedullary plasmacytoma (SEP). SEP is a malignancy that originates from plasma cells, which most commonly occurs in the head and neck region, and expresses high levels of the $\alpha_4\beta_1$ integrin receptor.[15,27] We compared structured

illumination fluorescence molecular imaging (SIFMI) with conventional, uniform illumination planar fluorescence reflectance imaging (PFRI), planar fluorescence imaging normalized by reflectance (Normalized)[28], and diffuse optical spectroscopy imaging (DOSI)[29]. Spatial-frequency domain imaging (SFDI) using structured illumination has previously demonstrated improved contrast over conventional planar illumination imaging for improving spatial resolution in phantoms[26] and tissues[22], but this was the first application of structured illumination for *in vivo* tumor-specific fluorescence contrast enhancement. We demonstrated that SIFMI, in combination with tumor-selective fluorescent molecular probes, enhanced contrast to better identify tumors and tumor boundaries *in vivo*.

4.2 Methods

4.2.1 Illumination Pattern Generation

Structured illumination patterns were projected by digital micromirror device (DMD)-based projector (DLP Lightcrafter 4500, Texas Instruments) using only the red light emitting diode (LED) (624 ± 18 nm) for fluorescence excitation of the fluorescent molecular probe, LLP2A-Cy5 (peak $\lambda ex/\lambda em$ = 657/676 nm)[27]. A NIR-sensitive complementary metal oxide sensor (CMOS) camera (Firefly MV FMVU-03MTM-CS, Point Grey Research, Canada) captured images after excitation light was blocked by optical bandpass filter (720 ± 20 nm, 720AF20, Omega Optical, Brattleboro, VT). The projector was positioned such that the offset projection uniformly illuminated the imaging platform over the camera field of view (**Figure 4-1a**). Pattern projection and image acquisition were controlled by customized MATLAB (The Mathworks, Inc., Natick, MA) code.[30] Premade 8-bit grayscale sinusoidal fringe pattern images, each offset by $2\pi/3$, were projected onto the subject using the red channel of the projector (**Figure 4-1b**). Images were

acquired and as 16-bit tagged image file format (TIFF) for each pattern, followed by full-field illumination and no illumination (dark) captures. This routine was repeated with neutral density emission filter in place of bandpass filter for illumination reference. Initial studies were performed using silicone-based phantoms with optical properties similar to biological tissues and fluorescent inclusions.[31] These studies indicated that fluorescence contrast enhancement was maximized when using a low frequency sinusoidal pattern of 0.66 cm^{-1}, which was subsequently used for all *in vivo* animal studies.

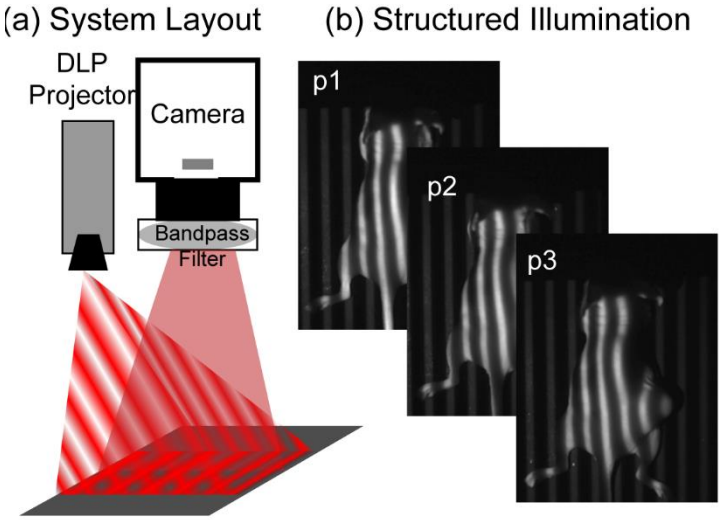

Figure 4-1: (a) Design of SIFMI imaging system including DLP projector providing patterned excitaion and CMOS camera for fluorescence detection. (b) Excitation patterns (3) projected onto subject for optical sectioning of superficial and deep fluorescence. Figure courtesy of Dr. Walter Akers.

4.2.2 Animal Model Development

All animal studies were conducted according to protocols approved by the Washington University Animal Studies Committee. Human multiple myeloma (U266) tumor xenografts were grown (Charles River Laboratories, Wilmington, MA) by subcutaneous injection of 1 million cells in the right flank of 8-week old male NCR nude mice (n = 2).

4.2.3 Fluorescence Imaging

When tumors were 1 cm in maximum diameter, mice were anesthetized with isoflurane (2% v/v in 100% O_2) and injected with 2.5 nmol LLP2A-Cy5 in 0.1 mL 4% dimethylsulfoxide (DMSO) in sterile water via lateral tail vein. LLP2A-Cy5 accumulates in tumors expressing $\alpha_4\beta_1$ integrin and has absorption and emission spectra suitable for our custom developed imaging system.[27] Eighteen hours post-injection, mice were anesthetized and placed prone on the imaging platform of the SIFMI system **(Figure 4-1a).** Image processing and analysis were performed using NIH ImageJ and MATLAB. Imaging was also performed using the Optix MX3 time-domain DOSI system ($\lambda ex/\lambda em$ = 670/695 nm) in single point source-detector setup with raster scanning (3 mm separation).[25]

We chose an animal model of SEP for this proof-of-concept study as this cancer presents clinically in regions where preservation of healthy tissue is necessary and expresses a marker that can be targeted for molecular imaging.[32,33] We intentionally positioned the tumors underneath the skin to demonstrate the performance of various fluorescent imaging techniques when the tumor was not directly visible by the operator.

4.3 Results

4.3.1 Image De-convolution

Summation of the three phase-shifted fluorescence images using **Eq. 4-2** resulted in I_0 **(Figure 4-2a)**, which was equivalent to planar fluorescence images acquired with uniform illumination. These I_0 images contained both tumor and background fluorescence, showing high signal throughout the mouse body with highest signal from the subcutaneous xenograft on the right flank. High signal was also present from the stomach and intestines, presumably from dietary

sources. Superficial signals were isolated by demodulation of phase-shifted images with frequency-dependent characteristics according to **Eq. 4-3**, yielding the surface components in I_S **(Figure 4-2b)**. Further image analysis indicated true surface fluorescence signal was equal to twice the values in I_S and subtraction of $2*I_S$ improved tumor isolation and reduced background fluorescence, correlating with *ex vivo* fluorescence measurements (**Figure 4-2c**). The linear artifacts present in I_S and passed through processing to I_C can be minimized by further optimization of projected excitation patterns.[22]

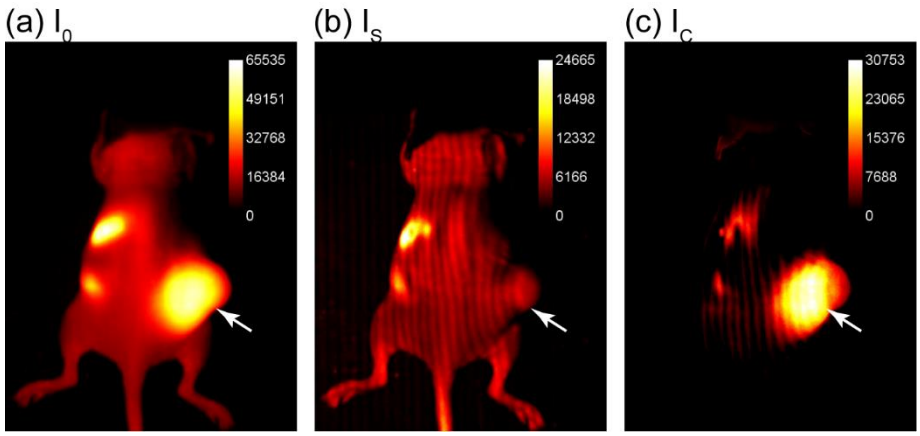

Figure 4-2: Demonstration of SIFMI process with subcutaneous tumor xenograft model and NIR fluorescent molecular probe with high affinity for multiple myeloma cancer cells in solid tumor (arrow). (a) Planar fluorescence uniform illumination equivalent image (I_0) reconstructed using the sum of the projected light patterns (Eq. 4-2). (b) Surface signal image (I_S) from the modulated signals (Eq. 4-3). (c) Subsurface, diffuse signal (I_C) according to a modified Eq. 4-1. Figure courtesy of Dr. Walter Akers.

4.3.2 Gradient-Based Algorithm

For comparison of SIFMI to other *in vivo* fluorescence imaging techniques, region-of-interest (ROI) analysis was performed for data acquired using uniform illumination PFRI, fluorescence/reflectance normalization, and DOSI. The normalization of PFRI was performed using the ratio of fluorescence to excitation.[28] We first compared the fluorescence intensity spatial

distributions obtained using the various methods **(Figure 4-3a)**. PFRI tumor imaging resulted in the highest signal emitted from within the tumor with a gradual reduction until the signal was that of the background fluorescence. The normalized image resulted in a reduction in bleed-through reflectance, however there was still significant background signal from the non-tumor regions. The DOSI image showed the fluorescence localized to the tumor, with background fluorescence limited to the scattered light traveling to the tissue adjoining the tumor. The SIFMI approach resulted in high signal from the tumor, and a striped artifact pattern from incomplete modulated signal subtraction. When the fluorescence intensity for all images were compared **(Figure 4-3c)**, using the cross section shown in **Figure 4-3b**, it was apparent that the SIFMI approach had the highest signal from within the tumor as compared to the signal on either side of the tumor.

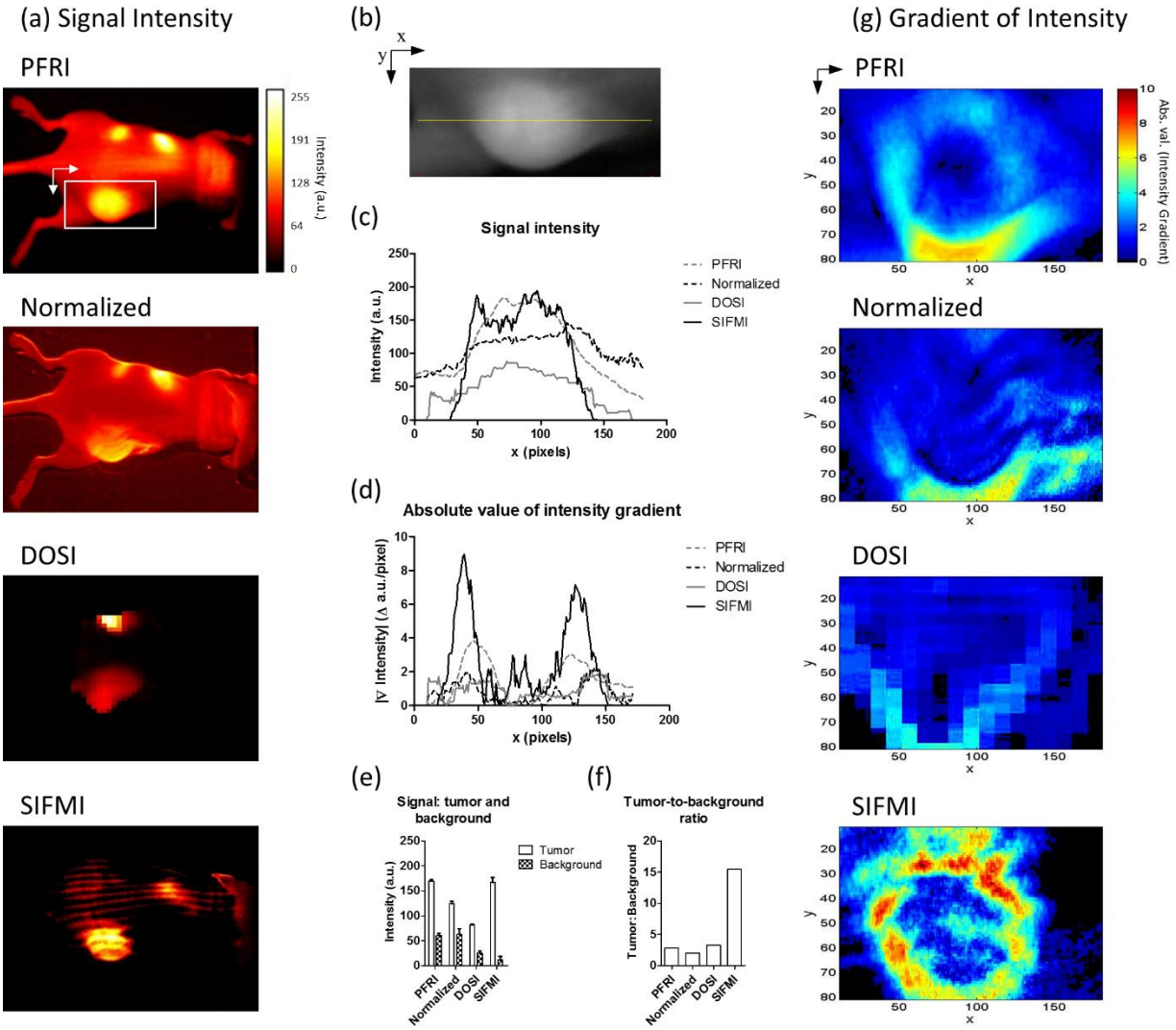

Figure 4-3: (a) Fluorescence signal intensity for the same mouse imaged using planar imaging, fluorescence/reflectance imaging, diffuse imaging, and structured illumination. (b) Example of ROI analyzed, with yellow line indicating the origin for the values plotted in (c) and (d). (c) Signal intensity plot from non-tumor region (background), through tumor region, then back to non-tumor region. (d) Absolute value of the gradient of intensity plotted along the line selected. (e) Signal intensity quantified for the tumor region and the non-tumor region. (f) Tumor-to-background ratio calculated using the signal intensity. (g) Absolute value of the gradient of intensity visualized over the ROI for the different imaging methods.

We then calculated the tumor to background ratios by selecting ten points from the center of the tumor, and ten points from outside of the tumor, but still within the ROI and on the mouse surface. The quantitative results of fluorescence intensity followed the initial visual inspection

with the PFRI and SIFMI having a high tumor signal **(Figure 4-3e).** SIFMI resulted in higher tumor contrast due to background subtraction, resulting in a five-fold higher tumor to background ratio than other full-field fluorescence imaging methods **(Figure 4-3f)**.

We further applied spatial gradient mapping to enhanced tumor boundary display.[34] In doing so, we preserve the sensitivity of SIFMI, while still providing useful spatial feedback to the operator. The rate of the change in fluorescence intensity in space was quantified, and the absolute value of the gradient was compared for each method **(Figure 4-3d)**. Spatial gradient maps were calculated in both the x- and y-directions, and the maximum absolute value of the intensity gradients chosen for each pixel. The tumor intensity gradient of the SIFMI image was much higher than other methods, providing well-defined boundaries of the tumor **(Figure 4-3g)**.

4.4 Discussion

We demonstrated that structured illumination fluorescence molecular imaging (SIFMI) isolated subsurface fluorescence from subcutaneous tumor xenografts, eliminating background signals from reflected excitation light, auto-fluorescence, and nonspecific fluorescent reporter accumulation in overlying skin. SIFMI allowed for rapid optical sectioning which provided similar results to more time-consuming raster scanning[35], line scanning[36], and tomographic reconstruction[35,37,38] methods. The use of striped patterns of different frequencies allowed for clear delineation between the tumor and the background fluorescence. In doing so, tumor contrast enhancement did not rely on arbitrary, user-defined thresholding[13].

4.5 Conclusions

SIFMI analysis using a gradient-based analysis method highlighted the tumor boundary without the need for *a priori* information. A key challenge in the translation of fluorescence-based imaging to clinical application has been removing background fluorescence. We demonstrated that structured illumination allowed for tumor boundary delineation without the need for thresholding out the background fluorescence. The next piece of valuable information to structurally characterize tumors is understanding the extent of tumor invasion. Tumor extent is often clinically classified based on penetration depth into the surrounding tissue. We next examined the research field of fluorescence depth imaging to determine appropriate techniques to accurately calculate tumor depth.

Chapter 5 :

Fluorescence Depth Imaging

5.1 Introduction

The attenuation of light in tissue results in more than just a decreased signal, it also causes a fundamental challenge when attempting to locate a light source within tissue at an unknown depth. A fluorescent inclusion of small size with a shallow depth will result in the same signal at the surface as a large inclusion at a greater depth. Additionally, tissues are by nature heterogeneous and cannot be easily modeled by fixed optical parameters. To further complicate the inverse problem, the fluorophore concentration and quantum efficiency also must be considered because they impact the fluorescence intensity observed at the tissue surface. The result of these unknowns is an ill-posed inverse problem where the number of unknowns is greater than the number of equations to represent the system. The ill-posed nature of the system renders depth estimation of a fluorescent signal in tissue complex.

Many approaches have been investigated to solve the inverse problem. The approaches can be divided into categories that largely overlap with each other. Some examples include analytical methods, empirical methods, and combination approaches. Specific modalities utilize solving the diffusion equation using *a priori* information, spectral imaging, temporal imaging, diffuse optical tomography (DOT), fluorescence molecular tomography (FMT), and structured illumination imaging. Many of these approaches have been validated in tissue simulating phantoms, however few have been used *in vivo*.

5.2 Depth Imaging: A Historical Overview

Here we have summarized the various techniques to identify fluorescent inclusions in turbid media. We have focused on fluorescence guided techniques, but some absorption-based

techniques that could be modified to fluorescence were included where indicated. We divided the approaches into planar, tomographic, and hybrid imaging methods, and the light behavior representation into ballistic, diffuse, and empirical. Hybrid imaging techniques drew from both planar and tomographic imaging modalities. Empirical light modeling representations are based on observations of optical behavior rather than analytical solutions to ray diagrams, or solving the radiative transport equation. A summary of the classification system used to describe the techniques is shown in **Table 5-1**.

Table 5-1: Overview of approaches used to estimate depth using fluorescence in a turbid media.

		Light Behavior Model		
		Ballistic Light Representation	Diffuse Light Representation	Empirical Light Representation
Imaging Method	Planar	*Optical Gate** *Two-Photon*	*Diffusion Equation Approximation* *Random Walk Equation Approximation*	*Relative Fluorescence Intensity* *Temporal* *Multi-Wavelength*
	Tomographic		*Diffuse Optical Tomography** *Fluorescence Molecular Tomography*	
	Hybrid	*Dual Offset Detectors** *Dual Offset Light Sources* *Frequency-Domain Phase Cancellation* *Masked Detection* *Structured Illumination*		

* Methods using absorbance that could presumably be modified to use fluorescence.

5.2.1 Summary of Approaches

The purpose of our literature review was to provide a comprehensive overview of the field of fluorescence guided depth estimation. As part of our literature review we summarized each of the methods in **Table 5-2**. The maximum depth imaged to, along with the associated error, is listed where reported by the authors or inferred based on the figures in the original publication. Methods

based on absorbance have been noted, along with whether the method was applied in an imaging phantom or in tissue.

Table 5-2: Fluorescence guided depth estimation methods. A depth-to-error score was calculated for comparison of the accuracy of different approaches. Note that not all methods were used for image reconstruction.

Authors	Year	Classification	Approach	Excitation Wavelength (nm)	Fluorophore	Tissue or Phantom	Inclusion Dimensions	Maximum Depth (mm)	Accuracy or Error	Depth:Error Score
Dunn et al	2000	Planar-Ballistic	2-Photon	780	Fluorospheres	Phantom	0.1 µm diameter spheres	0.250 mm	-	-
Kleinfeld et al	1998	Planar-Ballistic	2-Photon	830	FITC-dextran	*In vivo* rat cortex	Blood vessels	0.600 mm	-	-
Stasic et al	2003	Planar-Diffuse	Diffusion Theory Model	633	Aluminum phthalocyanine tetrasulphonate	Phantom	Fluorescent layer	5 mm	±0.9 mm, ≤18%	5.6
D'Andrea et al	2010	Planar-Diffuse	Diffusion Theory Model	633	Nile Blue	Phantom	4 mm diameter cylinder	18 mm	±1 mm	18.0
Hejazi et al	2010	Planar-Diffuse	Diffusion Theory Model	615 - 665	Qdot 705 ITK	Phantom	2 – 6 mm diameter spheres	4 mm	±0.68 mm, ≤17%	5.9
Eidsath et al	2002	Planar-Diffuse	Random Walk Theory Model	690	Far Red Fluospheres	Phantom	Cylinders 0.6 mm long and diameter 0.5 mm	12 mm	±1 mm, ≤10%	12.0
						Ex vivo porcine tissue slabs		11.5 mm	±1.73 mm, ≤ 15%	6.6
Tian et al*	2011	Tomographic-Diffuse	DOT	830	N.A.	Simulation	8 mm spheres	15 mm	±3 mm	5.0
						Human cortex	Blood vessels	14 mm	-	-

* Absorbance based method

Abbreviations: ICG – Indocyanine Green, DOT – Diffuse Optical Tomography, LOT - Laminar Optical Tomography, FMT – Fluorescence Molecular Tomography, SBR – Signal to Background Ratio

Authors	Year	Classification	Approach	Excitation Wavelength (nm)	Fluorophore	Tissue or Phantom	Inclusion Dimensions	Maximum Depth (mm)	Accuracy or Error	Depth:Error Score
Liu et al*	2005	Tomographic-Diffuse	DOT	690	N.A.	Phantom	6.3 mm diameter cylinder	40 mm	±10 mm	4.0
Hillman et al*	2004	Tomographic-Diffuse	LOT	532	N.A.	Phantom	0.1 mm diameter hair	2.5 mm	0.1 – 0.2 mm (resolution)	-
Ntziachristos et al	2001	Tomographic-Diffuse	FMT	675	Cy5.5	Phantom	3.5 mm diameter cylinder	25 mm	+ 30% (size estimate)	-
Solomon et al	2011	Tomographic-Diffuse	FMT	785	ICG	Phantom	3 mm diameter cylinder	12 mm	±1 mm	12.0
						In vivo rat lymph node	30 mm^3	12 mm	-	-
Axelsson et al	2007	Tomographic-Diffuse	FMT	532	Rhodamine 6G	Phantom	5.6 mm diameter cylinder	11 mm	-	-
Kuo et al	2007	Tomographic-Diffuse	FMT	580 & 620	675 nm LED fiber	Phantom	200 μm fiber diameter	17.6 mm	±1.2 mm	14.7
					Tritium	*In vivo* mouse	1 mm x 3 mm beads	5.7 mm	±0.7 mm	8.1
Judy et al	2015	Planar-Empirical	Relative Fluorescence (SBR)	785	ICG	Phantom	1 – 5 cm diameter spheres	30 mm	-	-
Hall et al	2004	Planar-Empirical	Temporal	666	Cy5.5	Phantom	4 mm cubes	16 mm	±0.9 mm	17.8

Authors	Year	Classification	Approach	Excitation Wavelength (nm)	Fluorophore	Tissue or Phantom	Inclusion Dimensions	Maximum Depth (mm)	Accuracy or Error	Depth:Error Score
Swartling et al	2005	Planar-Empirical	Dual Wavelength	780	IR-140	Phantom	1 mm thick layer	10 mm	±0.6 mm	16.7
Kolste et al	2015	Planar-Empirical	Dual Wavelength	635	Alexa Fluor 647	Phantom	1 cm x 1 cm	5 mm	±1.5 mm	3.3
Kainerstorfer et al*	2013	Hybrid-Empirical	Offset Detectors	690	N.A.	Phantom	3.5 mm diameter cylinders	60 mm	±4-7 mm	8.6
						In vivo breast tissue	Blood vessels	55 mm	-	-
Xia et al	2013	Hybrid-Empirical	Offset Light Sources	765	ICG	Phantom	2 mm x 2 mm x 0.6 mm	8 mm	±0.46 mm, ±5.8%	17.4
Chen et al	2003	Hybrid-Empirical	Frequency-Domain Phase Cancellation	780	Cypate-2DG	Phantom	5 mm spheres	25 mm	±1.2 mm (in x-y)	-
						In vivo mouse tumor	8 mm x 8 mm tumor	20 mm	±3.5 mm (in x-y)	-
Konecky et al*	2009	Hybrid-Empirical	Structured Illumination	Broadband	N.A.	Phantom	1.8 mm diameter cylinders	3 mm	-2.1 mm	1.4
Mazhar et al	2010	Hybrid-Empirical	Structured Illumination	660	IRDye 700DX	Phantom	1 mm diameter cylinders	4 mm	-	-

5.2.2 Analysis of Approaches

Each method was associated with a tradeoff of the depth imaged to and the error associated with imaging at that depth. We have provided an overview of the accuracy and imaging depth for each modality in **Figure 5-1**.

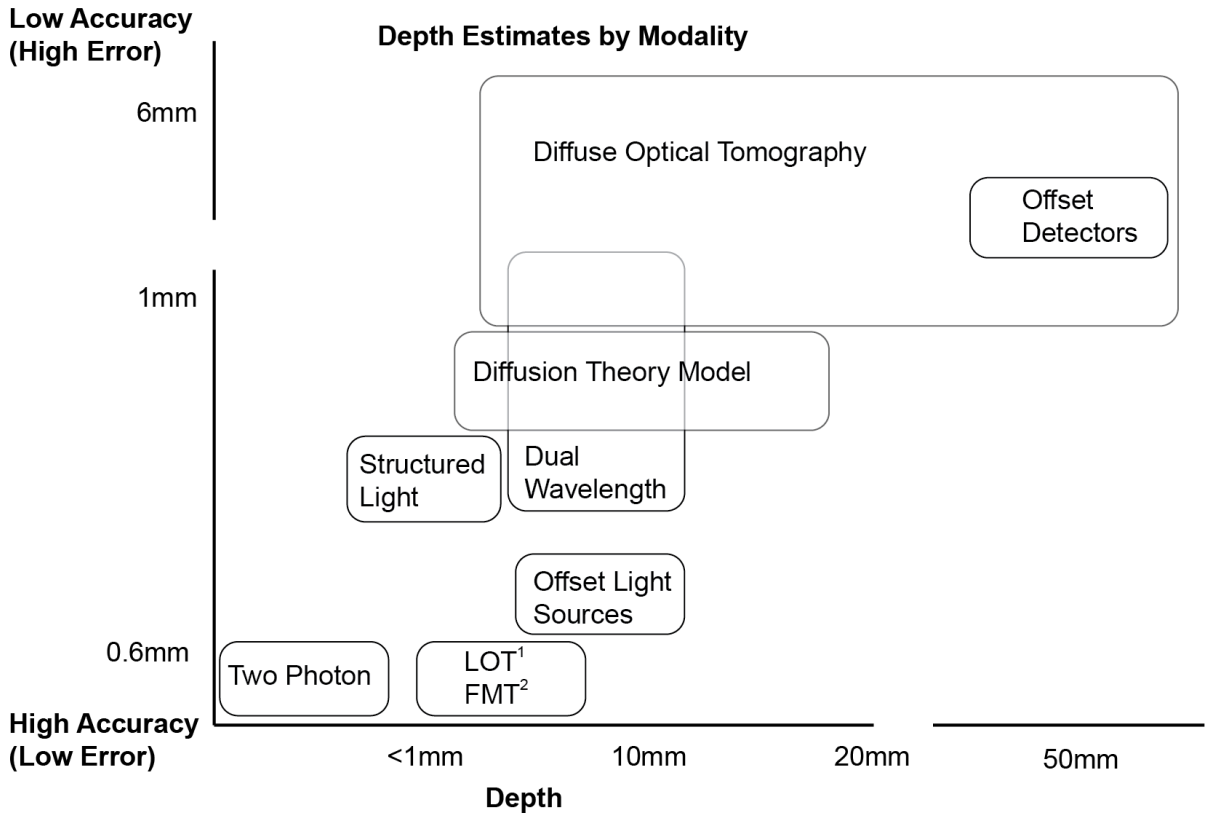

Figure 5-1: Overview of depth estimate vs. accuracy by imaging modality. Figure courtesy of Dr. Karla Bergonzi.

To analyze the different methods, we plotted the error of a method against the depth imaged to for each study (**Figure 5-2a**). The best-fit line representing all methods is shown to demonstrate the average performance. Studies falling below and to the right of the curve exhibited more

accurate depth calculations than methods to the left and above the line. It is important to note that this analysis does not consider the robustness or versatility of the method. Because many of the methods were empirical in nature, there is the possibility that a study performed well under the conditions tested without defining the boundaries for method performance. Additionally, whether the method was used solely for depth estimation, or if an image was reconstructed using the depth information was not considered in this analysis.

In **Figure 5-2b** we examined the overall depth for the estimates by method type. Note that this analysis is not necessarily indicative of the method overall, however it is indicative of the performance of the methods that reported depth values and were therefore included in this review. Not unexpectedly, approaches that were based on absorbance were capable of imaging to greater depths. This is because the quantum efficiency of the fluorescent probe is not a factor with absorbance, making it useful for deeper applications. For methods utilizing fluorescence for depth estimation, temporal-based, FMT, and analytical approaches achieved the deepest estimations. **Figure 5-2c** considers the imaging depth divided by the error, highlighting the methods capable of detecting fluorescence the deepest with the least amount of error. Temporal-based and hybrid imaging with offset detectors were the most accurate per depth, followed by FMT, dual-wavelength imaging, and the analytical approaches.

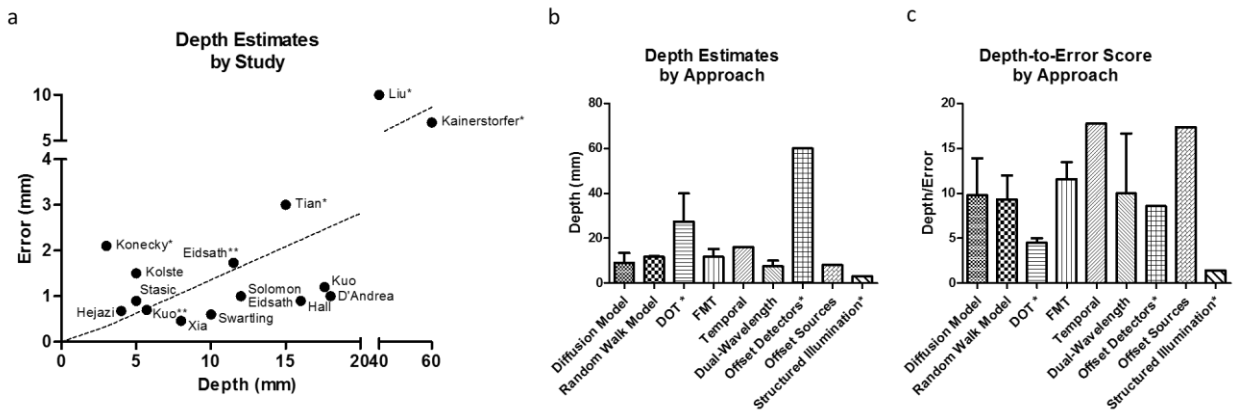

Figure 5-2: (a) Error vs. depth for each of the studies where data were available. Studies based on absorbance are indicated (*), as well as studies conducted in tissue rather than an imaging phantom (**). (b) Overall depth imaged to for each approach. (c) Depth-to-error score for each approach.

5.2.3 Conclusions

The field of optical fluorescence imaging holds much promise for future medical applications and scientific innovations. Using non-ionizing light allows for safe, rapid, and low-cost solutions to many medical imaging challenges. Although imaging with light in tissue is currently limited to a few centimeters in depth, having improved resolution in depth will only improve the field. In reviewing the approaches mentioned herein, we found that the accuracy and precision of the methods varied, and there were tradeoffs depending on the type of method selected.

When stratifying methods based on depth, the approaches can be divided into shallow (< 1 mm), intermediate (1 – 10 mm), and deep (> 10 mm) tissue imaging. For shallow depths, where high resolution depth information is required, ballistic light methods such as two-photon imaging will produce the most detailed images. Intermediate depth information was best obtained using dual-wavelength imaging, the analytical approaches, and the hybrid approach using dual offset sources. The dual-wavelength approach had 0.6 mm accuracy at up to 10 mm depths with images

formed down to 5 mm. This approach may lend itself well to translational applications such as intraoperative imaging, because multiple wavelengths can be rapidly imaged without a complex setup. Deep tissue depth imaging was most accurately accomplished using temporal-based estimation and FMT imaging. Temporal estimation used point-source detection, and the time of flight of a photon, to estimate the depth to 16 mm with an accuracy of 1 mm. A strength of temporal-based depth estimation was the insensitivity to changes in fluorophore concentration, although the fiber-based method was not used to recreate an image. FMT achieved wide-field imaging to 1 mm accuracy at depths up to 12 mm when using estimates of tissue geometry and optical properties. DOT/FMT also has the advantage that it has already been used to image *in vivo*.

In general, planar methods are advantageous because they are simple to implement, but inherent in their simplicity is the potential for greater error in depth estimation. Tomography is a more robust approach because it can account for solving the inverse problem computationally, however it comes with the tradeoff of increased complexity. Empirical approaches possess the simplicity of planar imaging; however, they rely on managing error through making mathematical assumptions to reduce the number of parameters that model the system. Hybrid planar-tomographic techniques show promise in that they combine the simplicity of planar methods, with the situationally appropriate assumptions of empirical methods, and still harness the power of tomography.

Many of the depth estimate methods we reviewed here may be bounded by certain unknown imaging conditions. These conditions could include unknowns about the tissue optical properties, variables between imaging systems, variation in fluorescent probe targeting of the tissue of interest, as well as many more factors. Because of these potential confounding factors, the superiority of a specific approach may depend on imaging need.

5.2.4 Perspectives

To date, few fluorescence guided depth estimation methods have been translated into pre-clinical or clinical applications. Choosing the proper method for a given application may be the best solution, as there may not be a "Holy Grail" to optical depth estimation for fluorescence imaging. For example, when the tissue parameters are expected to change greatly within the field of view, choosing a technique that is less impacted by the tissue optical parameters would be best suited. In other cases, the impact of the concentration of the fluorophore or the size of the inclusion may be the desired parameter to have the effects of unknown variability minimized. Further, by bounding an approach to a specific application, the true degree of depth estimation accuracy in a tissue type can be more precisely captured. Once an application and an approach have been selected, validation of the method is key to determine the robustness.

Because many of the approaches use overlapping principles, one can foresee using different combinations of methods that minimize the error based on the application. For example, structured illumination could be used to obtain the tissue optical parameters that could in turn be used as input values for an analytical or hybrid approach. Temporal-based imaging fundamentals are already incorporated into methods such as FMT/DOT, so the combination of different approaches seems like the logical next step in the field.

Overall the optimal solution for estimating the depth of a fluorescent inclusion in tissue remains elusive. The field shows great promise moving forward, with many techniques already developed to tackle this challenge. Identifying the relative strengths and weaknesses of each technique will allow for selecting the proper approach for each imaging situation. Identifying

specific translational applications, and then selecting the proper approach or combination of approaches, may prove to be the most suitable answer.

5.3 Fluorescence-Reflectance Imaging

From our analysis of the methods used to image fluorescence depth it was apparent that multiple sources of input data would be necessary for an accurate depth estimation method. Planar methods using empirical data were most accurate when there were multiple-sources, multiple-detectors, or multiple-wavelengths present. Swartling et al used a multi-wavelength approach to calculate the depth for a point-like fluorescence source, then Kolste et al expanded this to depth estimation using planar imaging [39,40]. We first investigated depth estimation using a fluorescence-reflectance method. This method was a simplified dual-wavelength imaging approach, where the fluorescence image was considered one wavelength, and the reflectance image was considered a different wavelength. By taking the natural log of the intensities at both distinct wavelengths, the depth was estimated. We added our fluorescence gradient approach to automatically define the tumor ROIs for analysis.

One important distinction to highlight is that there are multiple different depths that can be referenced when using the term "depth", each with their own implications and clinical importance. The sub-surface depth (d_{ss}) represents the distance of a fluorescent inclusion beneath the surface (**Figure 5-3**). The total depth (d_{total}) represents the depth of the fluorescent inclusion from the surface. The object depth (d_{obj}) can be obtained by subtracting d_{ss} from d_{total}. In this study we obtained d_{total} using NIR light and fluorescence-reflectance imaging.

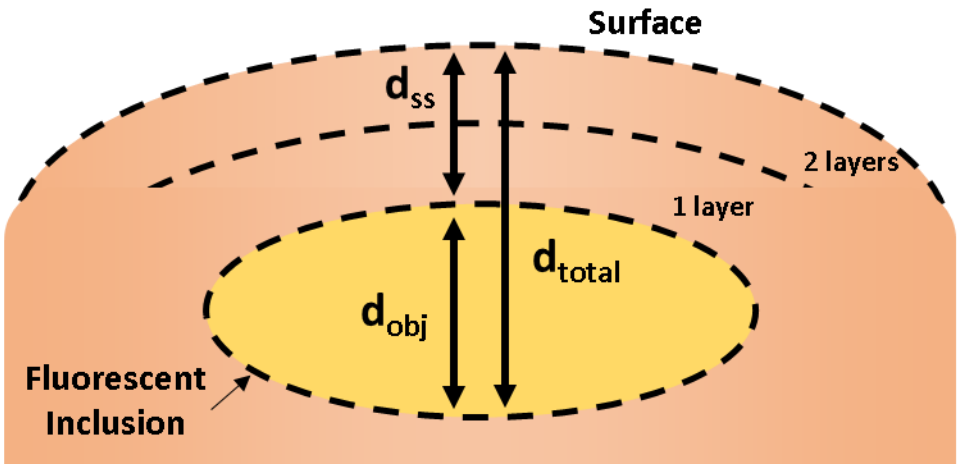

Figure 5-3: Diagram of a fluorescent inclusion in tissue covered by layers of tissue. d_{ss} represents the distance of a fluorescent inclusion beneath the surface. d_{total} represents the depth of the fluorescent inclusion from the surface, and $d_{obj} = d_{total}$ from d_{ss}.

5.3.2 Methods

After injecting LS301, we took fluorescence (**Figure 5-4a**) and reflectance (**Figure 5-4b**) images of our mice, and defined tumor vs. non-tumor using the same gradient-based approach that we used to obtain the tumor volume. For pixels defined as tumor, we divided the fluorescence signal by the reflectance signal, and then took the natural log of the ratio. This method required knowledge of the tissue optical parameters at the wavelengths of interest. We estimated these values using a previously developed model for tissue property estimation as a function of wavelength[41].

The fluorescence wavelength was 810 (λ_2), and the reflectance wavelength was the excitation light wavelength of 790 nm (λ_1). The following equations were used to calculate the depth as a function of the natural log of the ratio of the intensity at the two wavelengths.

$$\ln(\Gamma) = \left(\frac{1}{\delta^{\lambda 2}} - \frac{1}{\delta^{\lambda 1}}\right) \times D + \ln\left(\frac{A^{\lambda 2}}{A^{\lambda 1}}\right) \qquad \textbf{Eq. 5-1}$$

$$A = \frac{1}{3(\mu_a + \mu_s')} \quad \textbf{Eq. 5-2}$$

$$\delta = \sqrt{\frac{A}{\mu_a}} \quad \textbf{Eq. 5-3}$$

$$\ln(\Gamma) = m \times D + b \quad \textbf{Eq. 5-4}$$

$$D = \frac{\ln(\Gamma) - b}{m} \quad \textbf{Eq. 5-5}$$

Where Γ was the ratio of fluorescence intensity, δ was the penetration depth, A was the diffusivity based on the optical properties at each wavelength (λ_1 and λ_2), and D was the depth. The general form of **Eq. 5-4** can be rearranged and solved for depth using **Eq. 5-5.** The slope and y-intercept were calculated as m and b, respectively.

The input tissue optical parameters for **Eq. 5-2** and **Eq. 5-3**, μ_α and μ'_S, were estimated at our wavelengths of interest (790 and 810 nm) from a model developed by Jacques et al [41]. Using this model, we assumed the fraction of melanin as 3.8% for mice (average for a light skinned adult human) and the model predicted $\mu_{\alpha\ 790} = 5.867$, $\mu_{\alpha\ 810} = 5.208$, $\mu'_{S\ 790} = 14.142$, $\mu'_{S\ 810} = 12.941$. When these values were used in **Eq. 5-1** through **Eq. 5-4**, m = -1.927 and b = 0.098. We used these parameters to solve for depth pixel-by-pixel using **Eq. 5-5**.

5.3.3 Results

We found that the depth estimation method was very sensitive to the parameters that dictated the y-intercept value of the curve fit, which were in turn impacted by the optical parameters selected. To stabilize the depth estimation output, we calculated the difference in depth between the maximum and minimum depth values within the tumor region and recorded this value

as the estimated depth **(Figure 5-4c**). Saturated pixels were excluded from the analysis, and tumors that returned no depth values were represented as negative values in the plot. The method did not return values in two tumors (M1 left flank and M5 left shoulder) due to saturation, and one tumor (M3 left shoulder) due to inadequate fluorescence signal. The estimated tumor depths were compared to the caliper measured tumor depths in **Figure 5-4d**. The red line shows the ideal case of correlation between the method estimates and the measured depths, and the black line shows the curve fit of the actual correlation. While there was some difference between the estimated result and the idealized values, the average deviation from the caliper measurement was ±1.244 mm.

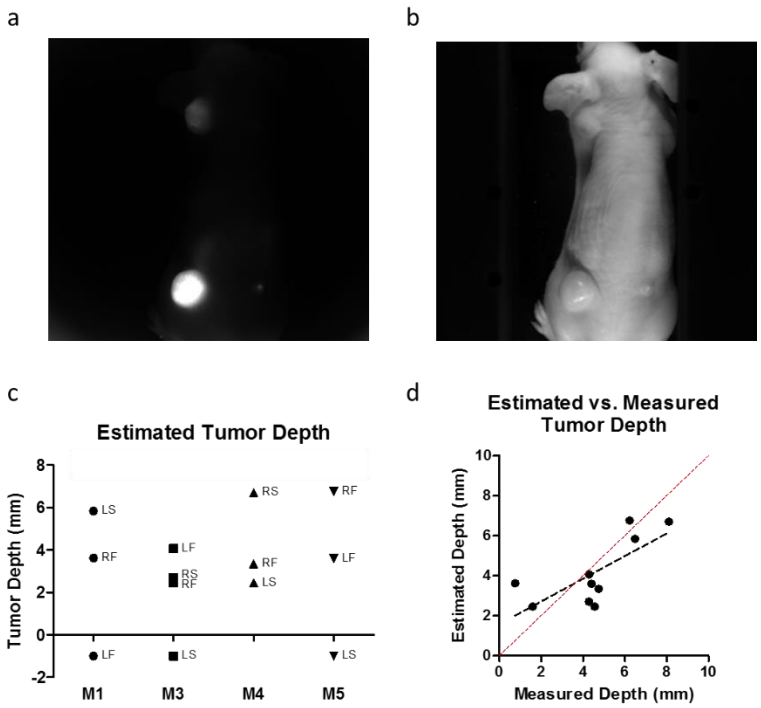

Figure 5-4: a) Fluorescence image of LS301 in a SCC-12 skin cancer model. b) Reflectance image of the same mouse in (a). c) Estimated tumor depth using the natural log of the ratio of the fluorescence divided by the reflectance image. d) Estimated depth using the fluorescence-reflectance vs. the measured depth. Red line showing the ideal case of correlation between the measured and estimated, and the black line showing the actual correlation.

5.4 Dual-Wavelength Imaging

Once we determined that fluorescence-reflectance imaging could be correlated with total depth, we sought to estimate the sub-surface depth using a related dual-wavelength approach. To calculate d_{ss}, we developed a custom fluorescent probe to clearly identify the two fluorescent signals at different wavelengths. This allowed us to gain greater control over the wavelengths imaged by having distinct excitation and emission wavelengths, and this greater control translated into increased depth resolution in our calculation. Our fluorescent probe consisted of two fluorophores conjugated together in a 1:1 molar ratio. In adopting this method, we demonstrated the feasibility of dual-wavelength imaging for both vessel depth determination and tumor sub-surface depth characterization.

Vessel sub-surface depth determination is important for intricate applications such as determining the distance from a vessel during complex dissection procedures and in tumor angiogenesis evaluation. Tumor sub-surface depth determination is important for determining margins in the z-direction during intraoperative imaging. Surgeons attempt to preserve a negative margin around a tumor. By understanding the distance between the exposed tissue and the tumor capsule, margins can be more effectively determined. Our method demonstrated a platform for dual-wavelength imaging using fluorescent probes specifically designed to resolve the sub-surface depth in tissue.

5.4.2 Methods

5.4.2.1 Imaging Agents

The dual-wavelength imaging agent LS903 (**Figure 5-5a**) was synthesized using cypate[42] and fluorescein isothiocyanate (FITC, Sigma). The FITC portion of the probe was used to produce green fluorescence, and the cypate portion of the probe to produce near infrared (NIR) fluorescence. A rigid polypropline linker consisting of 6 prolines (~2.28 nm) was used to flank the two dyes in order to increase the distance and minimize the probability of energy transfer[43]. LS904 was synthesized by conjugating m(PEG)$_{2000}$ amine (Laysan Bio, Inc) to the free carboxyl group on cypate in LS903. This was done to increase the enhanced permeation and retention tumor effect of the probe *in vivo*.

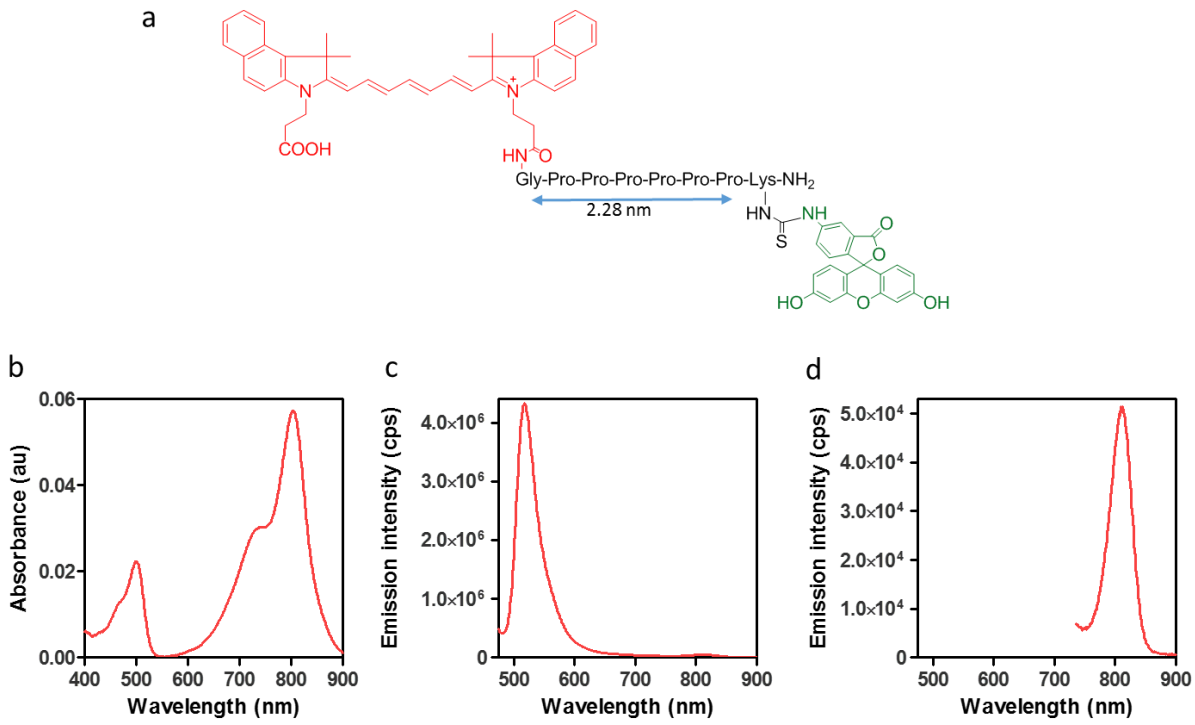

Figure 5-5: Molecular structure (a), absorption spectra (b), and emission spectra at excitation wavelength 475 nm (c) and 720 nm (d) for dual emission probe LS903. All spectra were taken in a solution of 1% bovine serum albumin in PBS, pH 7.4. Figure courtesy of Dr. Dolonchampa Maji.

The compounds were diluted in PBS, pH 7.4 with 1% bovine serum albumin milliQ water to simulate *in vivo* conditions. Absorption spectra were measured on a DU 640 spectrophotometer (Beckman-Coulter, Brea, CA). Fluorescence emission spectra were recorded on a FluoroLog 3 spectrofluorometer (Horiba Jobin Yvon, Edison, NJ) using 475 nm/490-900 nm and 720 nm/735-900 nm as excitation/emission wavelength with 5 nm slits for FITC and cypate respectively.

The absorption spectra of LS903 shows the existence of both the cypate and FITC moieties (**Figure 5-5b**). When excited at 475 nm, FITC emission can be seen as well as a relatively faint cypate signal around 800 nm indicating existence of energy transfer (**Figure 5-5c**). Cypate emission can be seen when excited at 720 nm (**Figure 5-5d**). The presence of two distinct fluorescent peaks allows for the imaging at dual-wavelengths to calculate the relative signal change as a function of depth.

5.4.2.2 In Vitro Imaging

All dyes were prepared in a 1% BSA solution prior to *in vitro* imaging. *In vitro* imaging was conducted using LS903 obscured by various materials layered on top. Our initial study was using lunchmeat (turkey breast, Budding) 0.65 mm thick to obscure a 32 μM LS903 sample in an Eppendorf tube. To obtain higher depth resolution we moved to silicone sheets 0.254 mm thick, and plastic sheets 0.13 mm thick, (Mc. Master-Carr, Elmhurst, IL). Simulated vessels were created using polyurethane tubing 0.015" ID x 0.033" OD (Braintree Scientific, Braintree, MA), and LS903 was imaged at two different concentrations (25 and 50 μM) for vessel studies. All dual-wavelength imaging was conducted using the Optix MX3 system (ART Advanced Research Technologies, Montreal, CA) with excitation and emission wavelengths at 480/535 nm for the green channel, and 785/810 nm for the NIR channel. Normalized fluorescence was used for dual-

wavelength image analysis, with the fluorescence signal normalized by the excitation power for each pixel.

5.4.2.3 In Vivo Imaging

Balb/c mice were injected with 10^6 4T1 murine breast carcinoma cells on the flanks and the resulting subcutaneous orthotropic tumors were allowed to grow until they were approximately 10 mm in diameter. Mice were shaved prior to injection and imaging. Tumor fluorescence imaging was conducted using the Optix for dual-wavelength analysis, and the Pearl small animal imaging system (Licor, Lincoln, NE) for NIR-specific analysis. For intra-tumor injections (n = 3), LS903 was prepared in a 1% MSA solution in PBS, for a final dye concentration of 60 μM in 20 μL of solution per tumor. For intravenous injections (n = 3) LS904 was prepared in a 1% MSA solution in PBS, for a final dye concentration of 60 μM in 100 μL of solution per mouse. Animals were imaged both before and after injection for intra-tumor injections, and at 0, 2, and 4, hours post injection for intravenous injections. The maximum *in vivo* contrast was detected at 2 hours post injection, so the 2-hour images were used for depth analysis. All studies were conducted in compliance with the Washington University Animal Welfare Committee's requirements for the care and use of laboratory animals in research.

5.4.3 Results

When describing tumor depth there are multiple depths that are of clinical significance. In the case of intraoperative imaging, the distance from the edge of the tumor to the edge of the healthy tissue is important in margin determination in the vertical direction. This distance is analogous to the sub surface depth (d_{ss}) when delineating the tumor margin in the z-direction (**Figure 5-6a**), or locating the depth of a fluorescent vessel under a tissue surface. There is also a

depth of the tumor itself (d_{obj}), and the overall depth of the tumor from the surface of the tissue (d_{total}). The d_{total} depth is important in tumor staging for malignancies that invade deeper structures. For our analysis we quantified the signal from dual-wavelengths as a function of depth to determine the d_{ss} for the application of *in vivo* tumor margin estimation, and *in vitro* simulated vessel depth determination.

5.4.3.1 In Vitro Depth Imaging

We obscured a solution of LS903 in a 1.5 ml Eppendorf tube under an increasing number of lunchmeat slices to represent increasing depth of a fluorescent inclusion below the surface. **Figure 5-6b** shows the NIR signal (cypate) was visible at greater depths than the signal in the green channel (FITC). We plotted the signal for each channel vs. depth (**Figure 5-6c**). The natural log of the ratio was plotted as a function of depth (**Figure 5-6d**), and the linear equation of the relationship was obtained (slope = 3.44, y-int = -0.27).

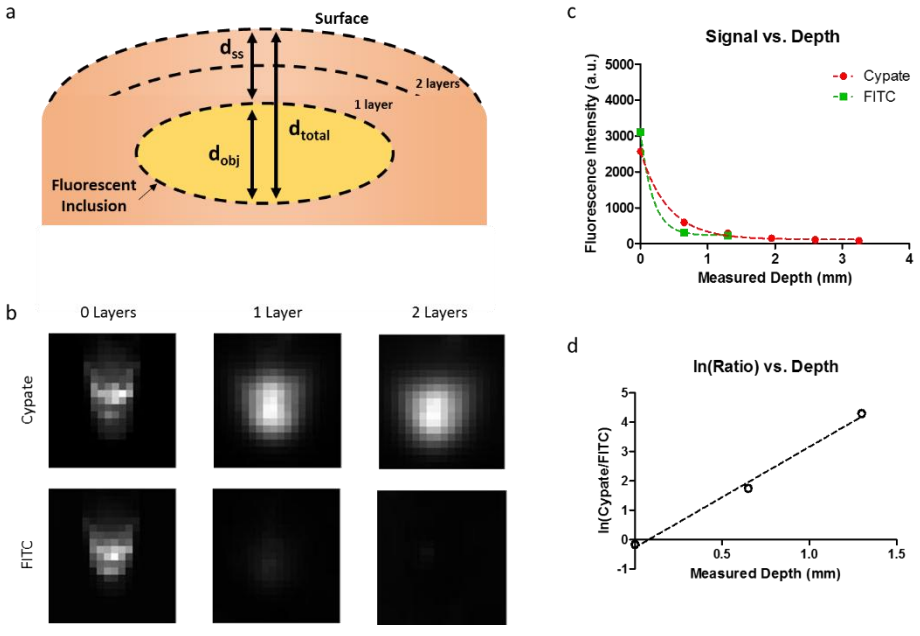

Figure 5-6: a) Diagram showing depth configuration of fluorescent inclusion overlaid by a medium (lunchmeat, silicone, plastic, or skin). The layers represent the depth layers used for *in vitro* testing, the absolute number of layers varied depending on the test. b) Images in both the cypate and FITC channels (rows) of an Eppendorf tube obscured by increasing layers of

lunchmeat. No overlying lunchmeat in the left column, 1 layer of overlying lunchmeat in the middle column, and 2 layers of overlying lunchmeat in the right column. c) Fluorescence signal vs. depth curve for the fluorescent ROI for LS903. d) Natural log of the ratio of cypate-to-FITC for LS903.

We simulated a vessel running beneath a layer of tissue by using silicone as our tissue phantom and polyurethane tubing as our vessel. LS903 was flowed through the vessel at varying concentrations and curves for the natural log of the ratios were generated (slope = 2.08, y-int = 0.43; slope = 2.10, y-int = 0.37). Next, we tested the performance of our method using a different material of unknown depth to obscure our vessel and imaged at both wavelengths (**Figure 5-7a**). The predicted depth values for the vessel were mapped in **Figure 5-7b** by using the ratio-curves previously generated. The average estimated depth was 0.40 mm and the measured depth was 0.52 mm.

Varying the optical properties, by changing the overlying material, impacted our depth estimate (**Figure 5-7c**). Materials that attenuated light more produced a higher slope value than materials that attenuated light less. Ideally this slope would be predictable prior to estimating the depth. We quantified the difference in accuracy of our depth estimates using average parameters from different materials and specific parameters using the same material (**Figure 5-7d**). There was a significant difference when using the different values ($p < 0.001$), thus indicating the importance of calibration studies with the same material that the depth estimate will be performed on. To translate this approach to *in vivo* imaging, we needed to generate a curve fit equation using the same material that we planned to image in. To accomplish this, we layered mouse skin at varying depths to obtain our tissue-specific curve (slope = 3.08, y-int = 0.05) (**Figure 5-7e**).

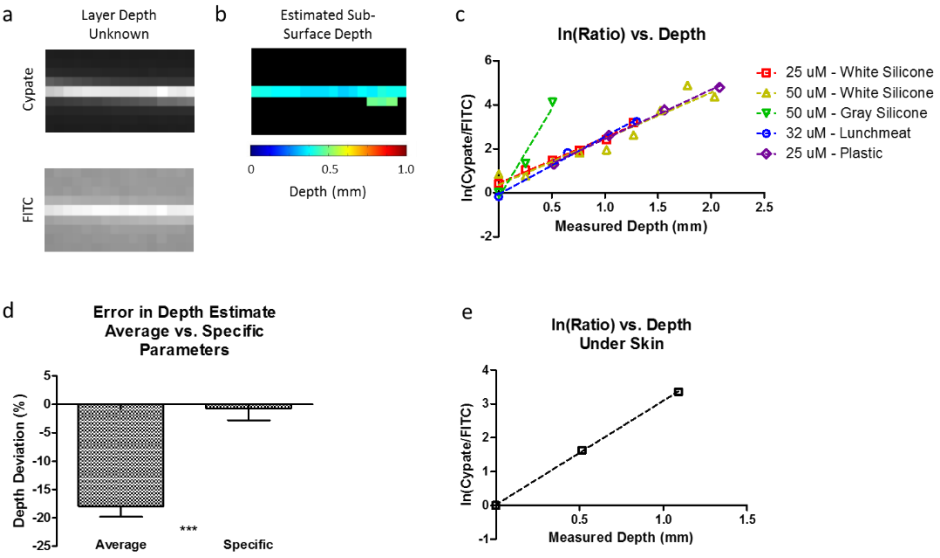

Figure 5-7: a) Dual-wavelength images of the fluorescent vessel under layers of plastic with unknown depth and optical properties. b) Depth map of estimated depth of vessel below the surface. c) Natural log of the ratio of dual signals vs. measured depth for different overlying materials and concentrations showing differing slopes depending on the medium. d) Comparison of the method accuracy for estimating depth in when using the average slope parameters and the specific slope parameter for a given medium. e) Calibration curve using the fluorescent vessel under *ex vivo* mouse skin to determine the curve fit parameters for skin.

5.4.3.2 In Vivo Tumor Depth Estimation

For *in vivo* depth estimation, we injected LS903 directly into 4T1 mouse flank tumors. M1 was injected bilaterally, and M2 was only injected in the left flank tumor. The two mice were imaged using a NIR-specific imaging system, and a dual-wavelength imaging system. The NIR-specific imaging system shows the fluorescence distribution of LS903 in the mice (**Figure 5-8b** and **Figure 5-8c**). The dual-wavelength imaging system shows the fluorescence in the tumors in both the cypate and FITC channels (**Figure 5-8d** to **Figure 5-8f**). The relative tumor signals were calculated in **Figure 5-8g**, and in both channels the treated tumors had higher fluorescence signal than the untreated control tumor (M2-RF).

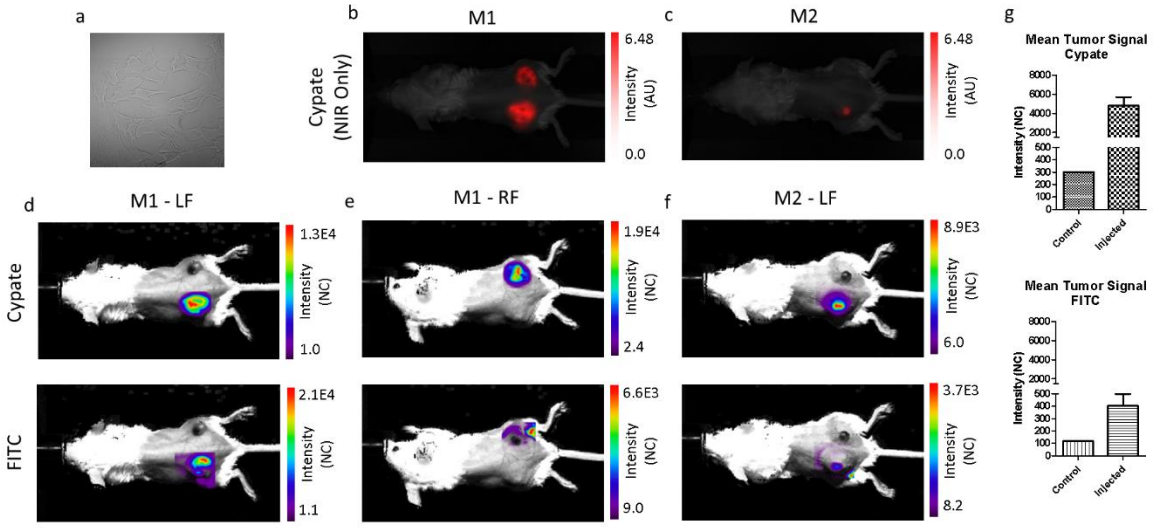

Figure 5-8: a) Bright field image of 4T1 cells injected for xenograft model. NIR image of LS903 distribution using the cypate channel for b) M1 and c) M2. Dual-wavelength images of the tumor ROI in the cypate channel (top row) and FITC channel (bottom row) for column (d) M1-left flank, (e) M1-right flank, and (f) M2-left flank. g) Quantification of the *in vivo* tumor ROI signals for the cypate channel (top) and FITC channel (bottom).

To estimate the depth of the fluorescence in the tumors, regions of interest (ROIs) were generated that included only the tumor in both the cypate (**Figure 5-9a**) and FITC channels (**Figure 5-9b**). The image from the cypate image was thresholded to create the tumor ROI. This ROI was then applied to the FITC channel, and the auto-fluorescence was subtracted by using a pre-injection image. The ratio of the two wavelengths was used to create a map of the tumor depth for each of the tumors (**Figure 5-9c**).

The depth values for each pixel were plotted in **Figure 5-9d** showing the distribution throughout the ROI. The tumor was then excised and prepared for histological analysis. The cypate and FITC channels were imaged, and areas of co-localization were analyzed (**Figure 5-9e**). The apparent outline of the co-localized fluorescence region was determined by visual analysis, then

10 measurements from this outline of the co-localized area to the surface were taken. The average measured tumor sub-surface depths were 1.31 ± 0.442 mm, 1.07 ± 0.187 mm, and 1.42 ± 0.182 mm, and the average estimated depths were 0.972 ± 0.308 mm, 1.11 ± 0.428 mm, 1.21 ± 0.492 mm, respectively (**Figure 5-9f**).

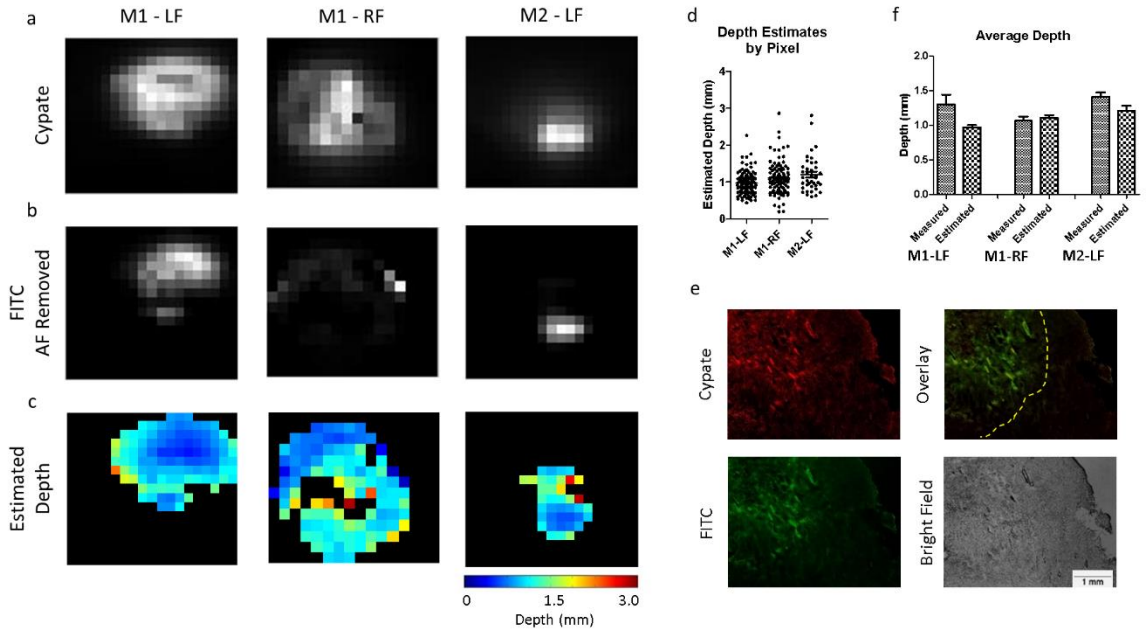

Figure 5-9: *In vivo* tumor images used for post processing. a) Cypate images (top row), and b) FITC images (bottom row) of the tumor region. The FITC image has the pre-injected auto-fluorescence subtracted from the tumor ROI. c) Depth estimate maps for each of the tumors. d) Pixel-by-pixel depth estimates for each tumor ROI. e) Representative tumor histology (M2-LF) showing cypate fluorescence (top left), FITC fluorescence (bottom left), overlay of both channels (top right), and bright field image (bottom right). f) Comparison of average measured depth vs. average estimated depth for each tumor.

To evaluate if our dye could be used to estimate depth when administered systemically, we conjugated PEG_{2000} to LS903 to obtain LS904. The signals were measured in both channels as a function of depth and the natural log of the ratios for the native and PEGylated forms of the probe were comparable. A 4T1 tumor bearing mouse was injected via the tail vein with LS904 and then

imaged using the NIR-specific and dual-wavelength imaging systems. The kidney was likely not visible in the FITC channel because it was deeper in the tissue than the green light could penetrate.

The cypate image shows that LS904 was present in the tumor region, as well as at the injection site in the tail, and in the kidneys when the mouse was viewed from the dorsal orientation (**Figure 5-10a**). The dual-wavelength images show that there was signal present in the tumor ROI in both channels (**Figure 5-10b** and **Figure 5-10c**). The bio-distribution shows the compound was primarily in the tumor, as well as the kidney and liver (clearance organs) (**Figure 5-10d**). The signals from each organ were quantified in (**Figure 5-10e**). The *ex vivo* signals were measured in both channels for both a control mouse tumor and the treated mouse tumors (**Figure 5-10f**), and the signals were quantified in **Figure 5-10g**.

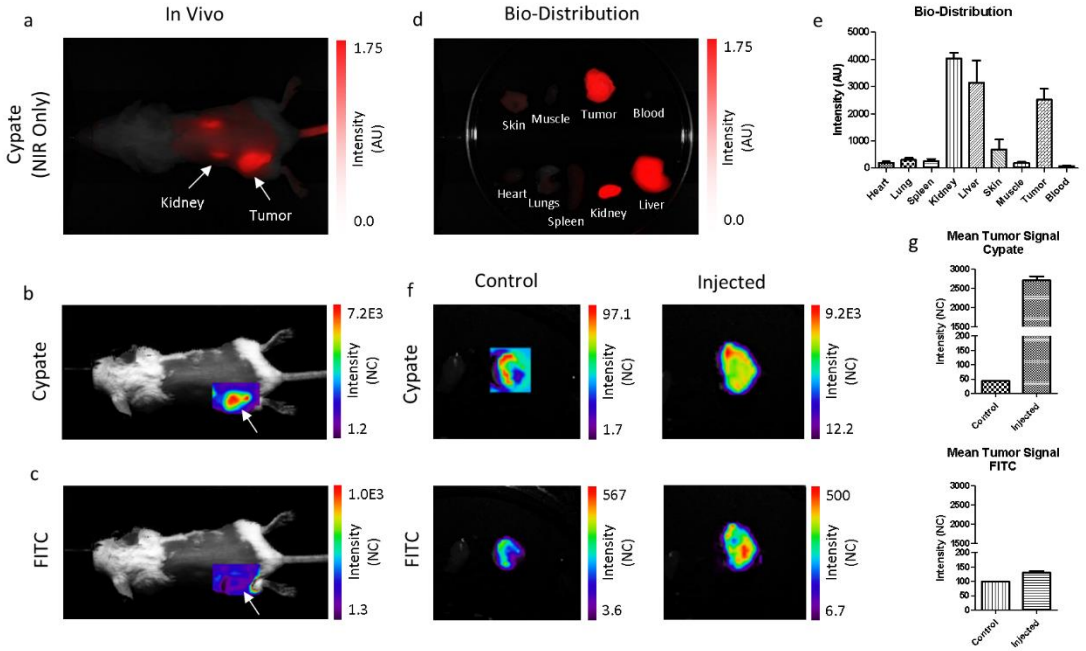

Figure 5-10: a) NIR image of LS904 distribution using the cypate channel. Dual-wavelength images of the tumor ROI in the (b) cypate, and (c) FITC channel. d) Cypate *ex vivo* bio-distribution showing organ distribution of the dye, with (e) quantification. f) *Ex vivo* tumor images of a mouse that was not injected with dye (left) and injected with LS904 (right). g) Quantification of the *ex vivo* image signals for cypate and FITC.

Depth maps were created for three tumors using the dual-wavelength images shown in **Figure 5-10**. **Figure 5-11a** shows the cypate images with the FITC images of the tumor ROIs in **Figure 5-11b**. Depth maps were created using our dual-wavelength images and are shown in **Figure 5-11c**. **Figure 5-11d** shows a pixel-by-pixel representation of the depth estimates, and **Figure 5-11e** shows the dual-wavelength histological analysis used for validation. The average measured depth values vs. the average estimated depth values for each of the tumors are shown in **Figure 5-11f**. The measured tumor sub-surface depths were 1.28 ± 0.168 mm, and 1.50 ± 0.394 mm, and the estimated depths were 1.46 ± 0.314 mm, and 1.60 ± 0.409 mm, respectively (**Figure 5-11e**).

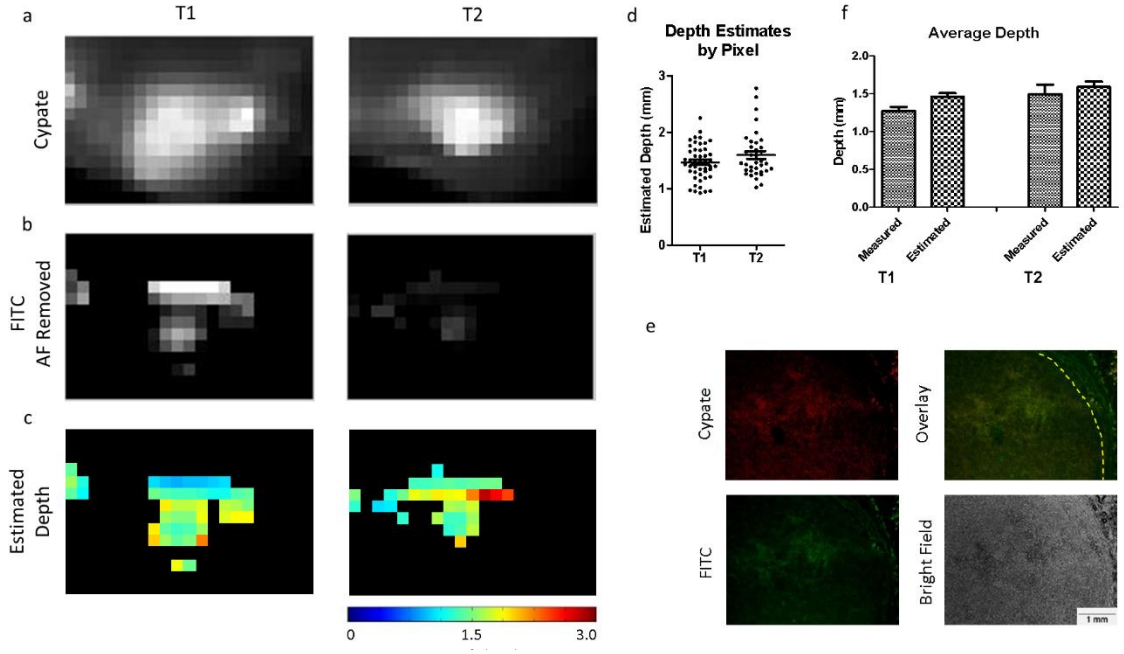

Figure 5-11: *In vivo* tumor images used for post processing. a) Cypate images (top row), and (b) FITC images (bottom row) of the tumor region. The FITC image has the pre-injected auto-fluorescence subtracted from the tumor ROI. c) Depth estimate maps for each of the tumors. d) Pixel-by-pixel depth estimates for each tumor ROI. e) Representative tumor histology (T2)

showing cypate fluorescence (top left), FITC fluorescence (bottom left), overlay of both channels (top right), and bright field image (bottom right). f) Comparison of average measured depth vs. average estimated depth for each tumor.

5.4.4 Discussion

We outlined a method for determining the sub-surface depth of a fluorescent inclusion obscured by a scattering medium for the applications of depth determination of blood vessels and tumors. Using a monomolecular dual-wavelength probe eliminated the unknown of the concentration of the dye, as both dyes were present in equal molar quantities. As such, the ratio of the signal obtained from each was predictable and used to calculate depth. Because our green light signal was attenuated rapidly by the tissue, we were only able to apply this technique to determine the sub-surface depth when the fluorescent inclusion was near the surface. To accomplish deeper tissue imaging, a fluorescent probe could be developed that uses two different NIR dyes conjugated together to take advantage of the NIR optical window. Deeper tissue imaging would allow for the expansion of this method into translational and clinical applications.

The dual-wavelength approach for sub-surface depth estimation was impacted by tissue optical properties, so with the *a priori* knowledge of the type of tissue imaging through, the approach could be applied in a feed-forward manner for translational imaging. Our method involved a preliminary calibration study to correlate the expected signal at measured depths for the medium that we would image through. Others in the field have developed methods for estimating tissue optical properties including parameterized mathematical models[44] and *in vivo* spatial-frequency domain imaging[45]. By combining these techniques with a dual-wavelength probe, accurate depth resolved tissue imaging may be achievable in many different tissue types.

An advantage of using an optical probe over auto-fluorescence spectral data alone, is that dyes also can be readily targeted to specific biologic structures using cellular receptors. The specificity of optical imaging allows for flexibility in the approach for different clinical uses. The simplicity of real-time planar optical imaging is advantageous for applications such as intraoperative imaging and screening procedures. In the context of intraoperative imaging, understanding the sub-surface depth of a tumor may decrease the rate of positive margins in the z-direction during tumor resection. Further, once a gross pathological specimen is removed from the body, real-time margin assessment could be performed via imaging prior to histological evaluation.

5.4.5 Conclusions

In the previous section we demonstrated the feasibility of the fluorescence-reflectance method to determine the overall depth of the signal (d_{total}). Here we demonstrated the feasibility of using a dual-wavelength custom developed fluorescent probe to determine the sub-surface depth (d_{ss}) of structures in tissue. The dual-wavelength method utilized LS903 with a green-emitting, and a NIR-emitting portion. Because there was a NIR portion of the LS903, the fluorescence-reflectance method could also be implemented using the same probe. The future combination of these methods would allow for a full understanding of the depth of an object beneath the surface for margin determination, and the depth of penetration of the object for extent evaluation.

We demonstrated methods to determine the tumor boundary, tumor total depth, and tumor sub-surface depth using fluorescence as a guide. Through combining these techniques, a tumor could be identified, then structurally evaluated to understand the depth and extent. Utilizing these methods will allow for the translation of tumor evaluation from a pre-clinical model, where many parameters are known, to a clinical application with additional unknowns.

We have now described static fluorescence imaging to both identify, and structurally evaluate, a tumor in tissue. Next, we will focus on dynamic fluorescence imaging for tumor evaluation. We will use fluorophore perfusion to extract tumor structure, then we will identify and characterize moving fluorescent tumor cells in the circulation.

Chapter 6 :

Perfusion Based Fluorescence Imaging for the Identification of Multifocal Orthotopic Breast Cancer Tumors in vivo

6.1 Introduction

Integral to the success of any imaging modality is the ability to generate contrast between the structure of interest and the surrounding tissue. In the field of optical imaging, contrast is primarily generated due to the accumulation of a dye, or changes in the absorbance or fluorescence of a dye. Each method has advantages and disadvantages depending on the imaging scenario and the desired output information. Accumulation of a dye is appropriate when there is a targeting moiety available for the structure of interest that is both sensitive and specific. Nonspecific binding can confound the result, and the accumulation of the dye often takes time on the order of hours post administration. Changes in absorbance or fluorescence can be achieved via activatable probes that change their chemical structure in the presence of an outside factor such as an enzyme. The time course may be rapid in this case; however, depending on the specificity of the enzyme, contrast may be difficult to obtain. Inherent in both approaches is the lack of additional structural information available when evaluating a tumor using fluorescence.

Static fluorescence imaging is often unable to delineate multiple structures of different tissue types due to the inability to simultaneously generate adequate fluorescence contrast in multiple tissue types. Dynamic contrast enhanced small animal imaging (DyCE) involves taking a time-series of images to understand the interaction of a fluorescent dye with tissue[46]. It relies on the time changes of a fluorescent molecular probe *in vivo* based on perfusion, circulation, dye kinetics, molecular interactions, and additional parameters. DyCE allows for the generation of spatiotemporal fluorescence images in a short amount of time while achieving imaging contrast, and without relying on dye targeting or activation[47]. Because the differentiation of structures is based on the dye kinetics, different tissue types can be analyzed using the same dye all at the same

time. DyCE has been used to investigate many applications including: vascular disease models[48], brain tumor hemisphere identification[49], and anti-angiogenic therapy monitoring[50]. Near infrared (NIR) perfusion based imaging has been extended from preclinical to clinical uses, highlighting the translatability of the approach[51].

For our dynamic imaging studies, we used a basis function approach with least-squares fitting to analyze our perfusion NIR images. Previous work suggested that using a basis function approach for data analysis would provide increased sensitivity and specificity for structural analysis as compared to a principal component analysis approach[46,47]. We chose dyes within the NIR optical window, as opposed to visible dyes, to allow for maximum light tissue penetration for sub-surface structural delineation. Even within the NIR optical window, dye properties could be varied such that their *in vivo* kinetics highlighted different structures. Harnessing this versatility allowed the method to be tailored to obtain optimal contrast based on the structures of interest while still achieving adequate contrast and maintaining short imaging times. Most studies previously used indocyanine green (ICG) to conduct perfusion imaging, however we used a cyanine-based dye. We demonstrated our approach to identify tumor pathology *in vivo* by identifying multifocal tumors when only the primary tumor location was known. Simultaneous imaging of the surrounding non-tumor structures was executed, and the sensitivity and specificity of perfusion-based imaging was evaluated. We demonstrated our approach in multifocal breast cancer tumors, for the eventual translational application of real-time intraoperative guidance.

6.2 Methods

6.2.1 Animal Model Development

Female athymic nude mice were used for all imaging studies. The HT1080 (human fibrosarcoma) mouse model was created by injecting 5 x 10^6 cells into the flank of the mouse. The orthotopic 4T1-Luc (murine mammary cancer) mouse models were created by injecting 0.1 x 10^6 cells into the mammary fat pads bilaterally. The HT1080 tumors grew for 3 weeks prior to imaging, and the 4T1-Luc tumors grew for 2 weeks prior to imaging. Imaging was conducted under anesthesia using 2.5% isoflurane in oxygen. Animals were sacrificed after imaging, and the 4T1-Luc tumors were harvested for histology. All studies were conducted in compliance with the Washington University Animal Welfare Committee's requirements for the care and use of laboratory animals in research.

6.2.2 Perfusion Imaging

Perfusion imaging studies were conducted following the general setup outlined by Hillman et al., with a dorsal or ventral view, and both orthogonal side views visible[47]. A cooled CCD camera (ORCA-ER C4742-80, Hamamatsu, JP), with an 830±10 nm BP filter (ThorLabs, NJ), was used for detection. Imaging was conducted at a frame rate of 1.3 frames/sec, with a 400 msec exposure time, and the f-stop set to 2.0. Excitation was achieved using a wide-field LED illumination source consisting of 16 mounted IR high power single chip LEDs (Roithner LaserTechnik, AU). Peak illumination at 760 nm, with power output of 0.6 mW/cm^2.

The NIR fluorescent dyes cypate and LS288 were synthesized in our laboratory, as previously reported. Cypate and LS288 possess hydrophobic and hydrophilic properties, respectively. Using spectrophotometry, the peak emission of cypate was 809 nm and the peak

emission of LS288 was 770 nm. We selected an excitation and emission wavelength that would minimize reflected light in our imaging, while at the same time capturing sufficient fluorescent light to detect changes over time. Our BP filter allowed light from 820 nm to 840 nm to pass with high efficiency. The filter range selected was higher than the peak wavelengths of our dyes, however the emission spectra were sufficiently broad such that satisfactory fluorescence was visible through the filter for imaging. In selecting a slightly higher BP filter window, we eliminated all reflected light from our 760 nm light source.

For imaging studies, each dye was mixed to a concentration of 100 μM in PBS with 20% DMSO, and 100 μL of total volume was injected into the mouse using tail vein catheters. The catheters were constructed of 0.015 in. ID x 0.033 in. OD polyurethane tubing (PU-033, SAI Infusion Technologies) and 29-gauge needles. Because of the extended length of the catheters, we accounted for the dead-space within the catheter (50 μL) when the total volume of dye was calculated.

6.2.3 Bioluminescence Imaging

Bioluminescence imaging was conducted on the 4T1-Luc xenograft mice expressing luciferase to confirm bilateral tumor location. These mice received an intra-peritoneal injection of 150 mg/kg D-luciferin in PBS (Gold Biotechnology, St. Louis, MO). Mice were then imaged at 10 minutes post injection under isoflurane anesthesia with an IVIS Lumina (PerkinElmer, Waltham, MA; Living Image 3.2, 10 second exposures, bin8, FOV 12.5 cm, f/stop1, open filter). The total photon flux (photons/sec) was measured from software-defined contour regions of interest (ROIs) over the tumors using Living Image 2.6.

6.2.4 Immunohistochemistry

Frozen tissue slides (5µm) were fixed by immersing slides in acetone for 5 minutes and air dried. Slides were rehydrated in DPBS and treated with dual endogenous enzyme block (Dako), TBS/0.1% Tween-20 (TBST) wash buffer, and 10 minutes of serum-free protein block (Dako). Rabbit anti-mouse CD31 antibody (D8V9E, Cell Signaling Technology) was used as primary antibody at 1:100 dilution. Following primary antibody incubation, slides were extensively washed in TBST. Anti-Rabbit EnVision+ System-HRP (Dako) used as the secondary antibody, followed by Liquid DAB+ (3,3'-Diaminobenzidine) Substrate system (Dako), both according to the manufacturer's protocol. Nuclear hematoxylin counterstain was applied, followed by dehydration through 70% ethanol, 95% ethanol, 100% ethanol, and xylene. Slides were mounted with Cytoseal XYL (Thermo Scientific). For each experiment, all slides were stained in parallel, using identical staining conditions.

6.2.5 Perfusion Algorithm Development

Our method was developed as outlined by Hillman et al., then modified to meet the needs of the current application. For our study, images were obtained in grayscale in individual tiff files over the imaging time. The image files were read into MATLAB (Mathworks, Inc., MA), where they were combined into a stack of images. A single image was used to select the center point of the ROIs to obtain the basis functions from. These center points were termed seeds, and were selected by the operator. The surrounding ROI area could be altered by the user, with increased stability obtained with a larger ROI. Because the goal of the method was to allow the method to determine the similar pixels rather than have the user define this, a small ROI of 5 x 5 pixels was selected for analysis. The average fluorescence intensity value of the ROI was calculated for each

time point, and this time course of values was the representative basis function for that tissue type. This process was repeated until each tissue type of interest was identified in the field of view.

Once each basis function was identified, the pixels in the field of view were analyzed using the nonnegative least-squares fit function in MATLAB (lsqnonneg). Each pixel was fit to each of the basis functions, and the degree of the fit for each basis function determined the extent of the color represented in each pixel. To generate the image, each pixel was assigned a color with the normalized percentage of the color shading matching the degree of fit to each basis function (more opaque coloring relates to a higher degree of fit). The DyCE method used normalized and background subtracted basis functions for the pixel time courses, however we did not see an improvement in our results by using these additional mathematic steps, so we utilized the raw fluorescence intensity for our analysis. Our perfusion-based algorithm was able to generate pixel-based images that represented both spatial and temporal data.

6.3 Results

In order to determine the appropriate dye for perfusion-based tumor identification, we used an HT1080 flank tumor model as our test case and varied the dye. We started with cypate, a near-infrared (NIR) dye that has been previously described. **Figure 6-1a** shows the in vivo imaging setup used to capture the dorsal and side views of the animal. **Figure 6-1b** shows the pixel fluorescence intensities for the basis functions for each tissue type. The in vivo kinetics of cypate were consistent with previous studies, with strong liver localization at short time points. As a result, other tissues exhibited decreasing fluorescence over time. **Figure 6-1c** shows the visual representation of the nonnegative least-squares fitting of each pixel to the appropriate basis function. Pixels with similar kinetics to the basis function were represented with the same color.

Differentiation between tissue types was apparent due to their differing characteristic perfusion kinetics.

We next injected LS288, another NIR dye that has hydrophilic characteristics as opposed to the hydrophobic characteristics of cypate (**Figure 6-1d**). Previous work has shown that the hydrophilic nature of LS288 contributes to increased tissue permeation as compared to cypate[54]. Hydrophobic dyes, such as cypate, have a higher binding affinity to albumin and are therefore more readily removed from the circulation by the liver. **Figure 6-1e** shows the LS288 basis functions and **Figure 6-1f** shows the visual representation of the basis function curve fits. In the case of the LS288 basis functions, each of the different tissues exhibited increased differentiation as time progressed as opposed to cypate that exhibited decreased differentiation over time (with the exception of the liver). We determined that the increased differentiation between tissues with increasing time was advantageous for our method, so we moved forward using LS288 for future injections.

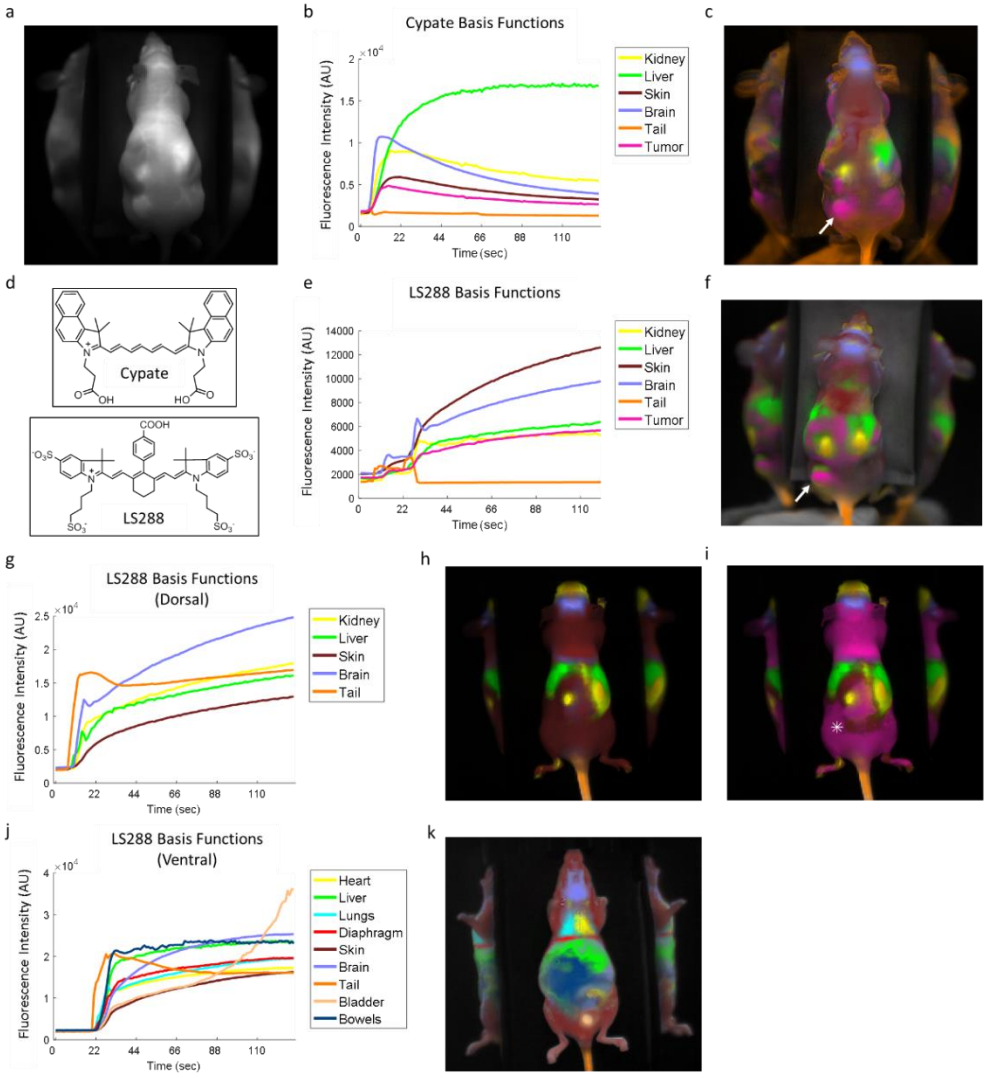

Figure 6-1: a) Imaging setup for perfusion imaging. Mirrors mounted at 45-degree angles on both sides of the mouse for additional views. Fluorescence image of cypate injected via the tail vein. b) Fluorescence intensity vs. time for cypate (organ specific basis functions). c) Visual representation of the pixel least-squares fit to the cypate basis functions. Each pixel is represented by the corresponding basis function color. The tumor located on the left flank is indicated by the arrow. d) Chemical structures for cypate and LS288. e) Fluorescence intensity vs. time for LS288. f) Visual representation of the pixel least-squares fit to the LS288 basis functions. g) Dorsal view LS288 basis functions obtained when imaging in an enclosed box without external light. The skin signal was lower than in (e) when no external light was present. h) Dorsal view fit to the LS288 basis functions. i) Area on the flank selected (asterisks) to confirm that the method does not give a tumor false positive when no tumor is present. j) Ventral view LS288 basis functions obtained when imaging in an enclosed box without external light. k) Ventral view fit to the LS288 basis functions.

Our next step was to optimize the method to reduce imaging artifact from motion and external light. We moved to a catheter-based injection, where the catheter was inserted into the tail vein, and the mouse was housed in an enclosed black box. The dye was injected into the tail vein without the need to open the box and expose the field of view to external light. In doing so, we were able to control the light such that only the fluorescence from the injected dye was visible. As expected, the shapes of the basis function curves for the kidney, liver, brain and tail (**Figure 6-1g**) were similar to the open box imaging. However, in this case the skin basis function curve had a lower signal relative to the other tissues. In this imaging method, the term skin is used to represent any tissue that does not have recognizable organs or structures beneath it. Likely skin represents a combination of skin, subcutaneous tissue, and fat. Because skin is highly reflective, any uncontrolled external light may impact the result more so than the other organs. **Figure 6-1h** shows the visual representation of the nonnegative least-squares fitting of each pixel to the appropriate basis function.

To make sure that the method was not automatically associating the flank location with a tumor, a region on the flank was selected in a similar position to where a tumor would be if present and pseudo-colored pink. For this run, the mouse did not have a tumor, so the expected result would be for the skin region and tumor region to be similar. Figure 6-1**i** shows that the least-squares fit associated with the artificial tumor selection was consistent with the skin, as should have been the case. From this we were confident that the method was assigning pixels to a tumor basis function only when a tumor was present. In **Figure 6-1j** and **Figure 6-1k** we imaged the ventral side of the mouse to visualize additional organs.

Once we determined that a tail vein catheter and eliminating light variability produced superior results, we investigated if the method could identify multifocal tumors. We used a 4T1-Luc orthotopic model, with bilateral mammary fat pad tumors. One mouse had tumors visible from the dorsal side, and the other had tumors visible from the ventral side (**Figure 6-2**Error! Reference source not found.**a**). When the mice were imaged using planar fluorescence intensity alone, without considering perfusion time, there was minimal contrast outlining the various tissue types and organs (**Figure 6-2**Error! Reference source not found.**b**). We confirmed the location of the tumor cells via bioluminescence imaging (BLI) in **Figure 6-2c**. Because we were interested in testing the ability of the method to locate a secondary tumor when the primary tumor location was known, we used the BLI image to determine our primary tumor for analysis. The tumor with the higher BLI signal was considered the primary tumor, and the tumor with the lower BLI signal was considered the secondary tumor.

For tumor visualization using perfusion imaging, the primary tumor was selected on one side of the mouse, and all other tissue with similar kinetics was identified by the method. In both mice the secondary tumor on the contralateral side of the mouse was identified when only the primary tumor was selected (**Figure 6-2d**). The perfusion method largely identified tumors in the same locations as the BLI, with the exception of regions of the dorsal view that showed a false positive on the back, and the ventral view that identified an area on the periphery of the secondary tumor. Because this method is based on perfusion kinetics, it is possible that the regions identified as tumor had similar vascular kinetics although they did not contain the actual tumor cells.

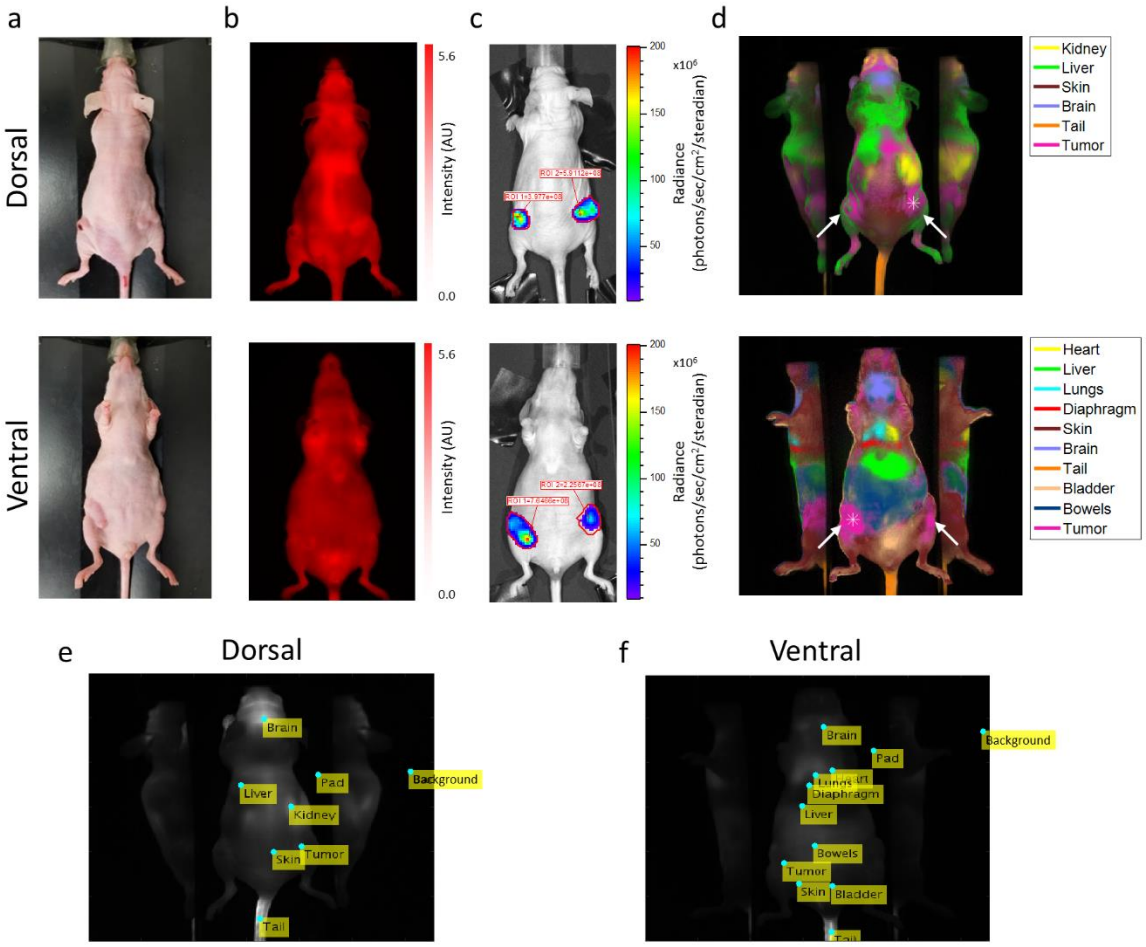

Figure 6-2: Multifocal tumor identification. (a) Bright field image of a 4T1-Luc orthotopic mouse model with bilateral tumors. Mouse from a dorsal view (top row), and a different mouse from a ventral view (bottom row). (b) Static fluorescence image of LS288 showing limited organ contrast. (c) BLI of tumor signal localizing the tumors and identifying the primary and secondary tumor based on the BLI signal. (d) Visual representation of the pixel least-squares fit to the basis functions. Tumor locations indicated by arrows, and primary tumor location selected for the basis function indicated by the asterisks. The images in (e) and (f) show the seed locations selected for the individual basis functions.

Figure 6-3a shows two large blood vessels feeding the surgically reflected primary tumor. Because the vessels were large, and the overlying tumor tissue was less thick around the periphery, this may explain the propensity of the method for increased localization of the tumor to the periphery compared to the BLI tumor locations. To examine the ability of the method to detect the

presence of a tumor, we investigated the tumor basis functions for each of the three LS288 injections as well as the cypate injection (**Figure 6-3b**). We found that the LS288 injections exhibited similar tumor perfusion kinetics, and that these basis functions differed from that of cypate. Because the perfusion kinetics were similar for a given dye in tumor tissue, this method may be amenable to using a predictive basis function curve to identify tumors. Using a predictive curve may allow for use of the method without a priori information from the image itself. Histological evaluation of the tissue using CD-31 staining showed that there was increased vasculature in the tumor as compared to the surrounding muscle (**Figure 6-3c**). The connective tissue directly surrounding the tumor showed the greatest degree of vascular density, consistent with our gross pathological findings (**Figure 6-3d**).

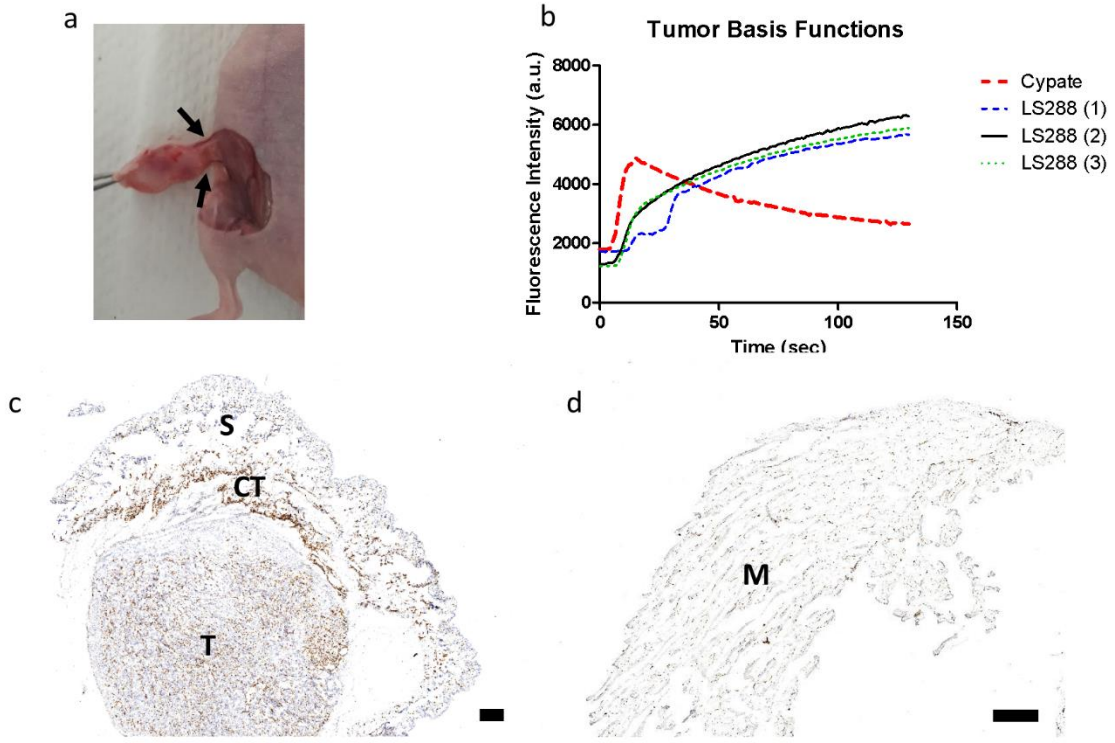

Figure 6-3: Tumor vasculature and tissue evaluation. (a) Image showing the primary tumor from the ventral view with two large vessels feeding the tumor located on the periphery (arrows). (b)

Tumor perfusion time courses for cypate and LS288 across different injection runs. (c) CD-31 staining (brown) of tumor showing increased vascularity in the connective tissue (CT) directly surrounding the tumor cells (T), and underlying the skin (S). Scale bar = 500 μm. (d) Muscle (M) tissue sample showing lower CD-31 staining than the tumor or subcutaneous tissue surrounding the tumor. Scale bar = 500 μm.

To further investigate the sensitivity and specificity of the method, we created a mask to represent the tumor region and considered this as our ground truth **Figure 6-4**.

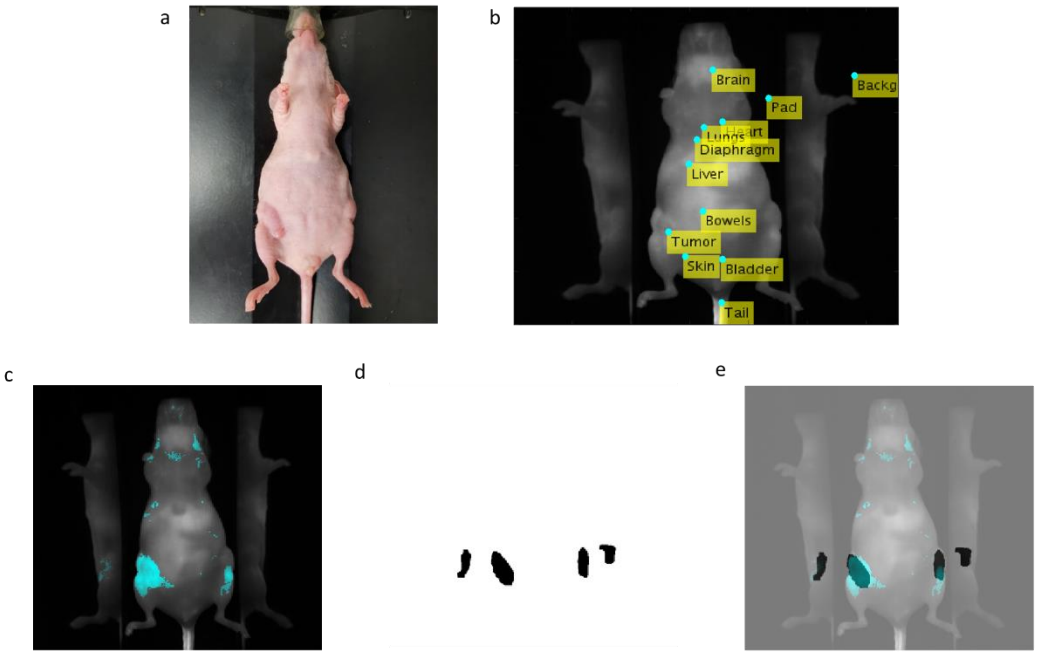

Figure 6-4: a) Bright field image of a mouse with bilateral 4T1-Luc orthotopic tumors. b) Seed locations selected for perfusion analysis. c) Pixels that fit the tumor basis function colored cyan. d) Masks were outlined manually in ImageJ to correspond with the tumor locations visible in (b). e) Overlay of mask region and method-generated tumor regions. Overlay was used for the sensitivity and specificity calculations.

The perfusion results for the tumors were compared to the mask as is visually demonstrated in **Figure 6-5a**. The sensitivity and specificity were calculated on a pixel-by-pixel basis, and were plotted for the cypate injection and the three LS288 injections (**Figure 6-5b and Figure 6-5c**). A

receiver operating characteristic (ROC) curve was generated and shows that the sensitivity and specificity of the method were superior to the random guess line (**Figure 6-5d**).

To investigate the effect of imaging time post injection on sensitivity and specificity, we considered the case of the mouse imaged from the ventral view and plotted the sensitivity and specificity as we varied the length of video analyzed (**Figure 6-5e**). In this case, the sensitivity was high at short imaging times (< 13 sec post injection), then fell for intermediate times (24 – 90 sec post injection), then rose again at longer imaging times (90 – 120 sec post injection). The specificity increased with increased imaging time until it reached an asymptote at around 24 seconds post injection. A ROC curve was created to simultaneously consider sensitivity and specificity, and three distinct groupings were apparent (**Figure 6-5f**). Group A had high sensitivity and was imaged for the least amount of time; however, this group also had the highest false positive rate. Group B balanced the sensitivity and specificity, and consisted of primarily of longer imaging times. Interestingly, Group C had the lowest sensitivity and was of the moderate imaging times, suggesting that there is a period of time post injection that the dye kinetics are similar in different tissues limiting differentiation. **Figure 6-5g** shows the basis functions for tumor and skin. Sensitivity at early time points may be driven by the slope difference between the curves, with tumors having a more rapid early uptake of dye. Specificity appears to be driven more by the magnitude of the difference between the curves.

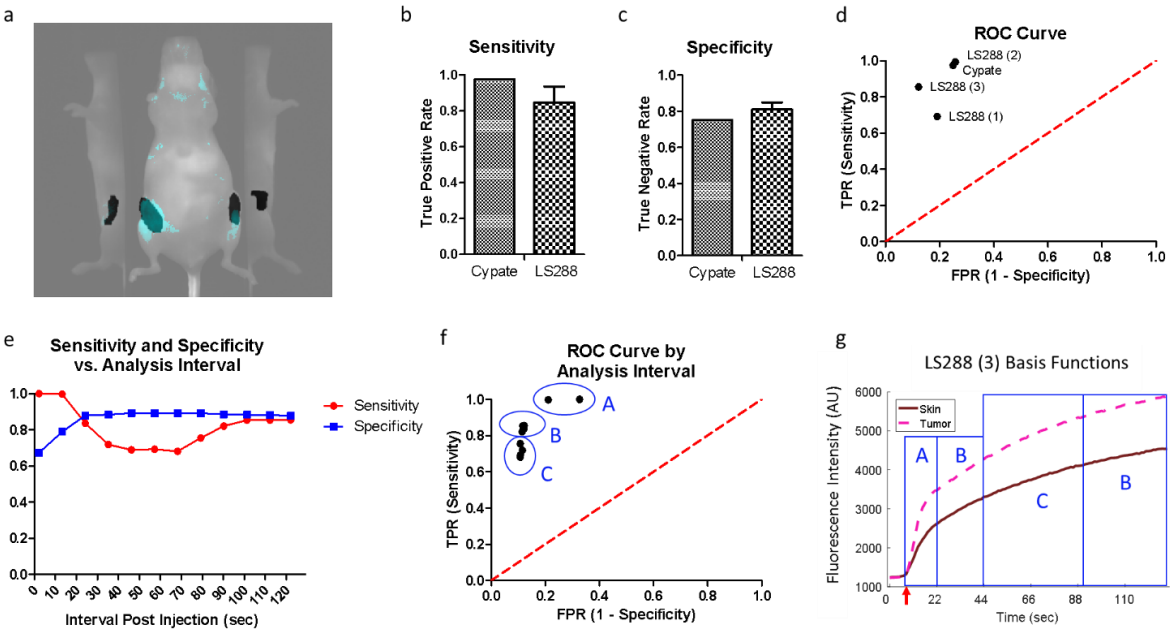

Figure 6-5: a) Mask used to calculate sensitivity and specificity. b) Sensitivity and c) specificity for a single cypate run and three LS288 runs (1), (2), (3). d) Receiver operating characteristic curve for each run. e) Sensitivity and specificity vs. analysis interval time post injection for LS288 run 3. f) Receiver operating characteristic curve for different analysis intervals post injection for LS288 run 3. g) Tumor and skin fluorescence vs. time for LS288 run 3. Injection at t = 9 sec (red arrow).Group A = 0 – 13 sec post injection, Group B = 13 – 24 sec and 90 – 120 sec post injection, and Group C = 24 – 90 sec post injection.

6.4 Discussion

We demonstrated a perfusion-based imaging method for tumor identification *in vivo*. The perfusion method was previously published for organ identification[47,49], however we expanded the approach to include the identification of multifocal tumor pathology while still observing non-tumor structural information. Static fluorescence imaging of targeted fluorescent dyes can give tumor contrast; however, this often takes a number of hours until the dye accumulates in the tumor. By simply imaging a few minutes of dye perfusion, tumors were identified more rapidly than with targeted dye accumulation. The sensitivity and specificity of the approach showed that it was effective in localizing tumor pathology when in a controlled light environment.

Tumors often exhibit increased angiogenesis, with larger blood vessels, as compared to healthy tissue [55,56], making a perfusion based approach useful to aid in tumor detection. Because tumors have different vascularity compared to other tissues and organs, the introduction of a fluorescent dye gave insight into the tumor perfusion kinetics which may be useful in better understanding tumor physiology. Our studies showed that using the same dye produced similar tumor perfusion kinetics regardless of the tumor model imaged. Perhaps there are other fluorescent dyes that have kinetics that vary as a function of specific tumor types. Factors such as the hydrophobicity of the dye can be considered to obtain the optimal dye for imaging the tissue of interest.

We demonstrated our method in both a single tumor model and a bilateral tumor model. In the single tumor model, a 5 x 5 pixel area was selected, and all of the other similar pixels were clustered and represented as such. Previous work selected the entire organ within a ROI to obtain the basis functions. Our approach utilized a seed-based approach where only a small number of pixels were needed to determine the proper basis function. Because the method relied on a seed-based approach for obtaining the basis functions, there was inherent variability in the method. Optimization of this method would allow for an automated approach to determining the proper seed locations to generate the most representative basis functions. The multifocal bilateral tumor model is of significance because by selecting only the primary tumor, we were able to extract the secondary tumor locations.

Identifying multifocal tumors using perfusion imaging holds promise in the field of translational optical imaging, because it allows a clinician to rapidly check for additional pathology at the point of care. We selected an orthotopic breast cancer model to test our theory for secondary tumor identification, because breast cancers can often be multifocal in nature[57,58]. Routine breast

cancer screening is conducted using mammography, and then if a tumor is suspected additional imaging modalities such as ultrasound and MRI are employed[59,60]. Mammography is a widely used screening modality, however it has limited sensitivity in identifying multifocal lesions making it less than ideal for preoperative planning[61]. MRI is more sensitive than mammography and is used in preoperative planning[62], however it is largely unable to provide real-time image guidance during a procedure. The location of tumor foci impacts surgical and clinical planning, so effective identification of all potential tumor foci before or at the time of a procedure is important.

Positive tumor margins are present in 20-70% of breast cancer surgeries, with multifocal tumors increasing the risk of a positive margin[63,64]. Previous studies have shown that intraoperative evaluation during tumor resection procedures can reduce the risk of leaving a positive margin, and therefore residual disease[65]. Optical imaging allows for real-time imaging, and tumor foci identification, making it useful for intraoperative guidance and tissue evaluation[18]. Once within a procedure, a surgeon could use fluorescence guidance to reduce the probability of leaving an unidentified residual tumor. Fluorescence imaging has already been employed intraoperatively to identify sentinel lymph nodes and visualize primary tumors[11,66]. Our perfusion-based imaging approach, when combined with intraoperative imaging, could reduce the chance of leaving small tumor loci post a surgical procedure. Presumably perfusion-based imaging could be applied to additional multifocal tumor models for pathology identification, such as for tumor metastases or to determine the extent of local-regional invasion.

6.5 Conclusions

We used dynamic fluorescence to identify tumor structure, in the next chapter we will use dynamic fluorescence imaging to identify and characterize circulating tumor cells.

Chapter 7 :

All-near-infrared planar fluorescence imaging platform for identification and size stratification of circulating tumor entities

7.1 Introduction

In the recent past, rare biomarkers in blood circulation have demonstrated great clinical potential in the diagnosis and management of killer diseases such as cancer. Circulating tumor cells (CTCs), CTC clusters, and tumor derived endothelial cell clusters have been detected in many forms of aggressive cancer.[67-72] These entities have each been suggested as potential cancer associated biomarkers, such as for early diagnosis of cancer metastasis. Interestingly, the metastatic potential of such entities depends greatly on constitution in terms of number and/or type of cells in the circulating cluster. For example, current data indicates that multicellular aggregates of tumor cells (two or more tumor cells) may show a much greater potential (up to 50 times) to cause distant organ metastatic than single CTCs.[73,74]. Alongside single CTCs, CTC clusters have been investigated for early diagnosis of cancer metastasis, monitoring therapy responses, and as prognosis indicators. Given this, in order to accurately use such cancer associated biomarkers it becomes necessary to not only reliably detect CTCs, but to also determine the size and other properties of these circulating entities in addition to their frequency of appearance.

There are various techniques available to detect and potentially classify CTCs based of size, however many of these involve taking a blood sample from a patient and analyzing it *ex vivo*. *In vivo* methods offer several advantages over *ex vivo* methods. *Ex vivo* methods rely on liquid biopsies that have limited sensitivity to detect rare CTCs in a patient blood sample (1-10 CTCs per 10 mL peripheral blood) due to the small volume of blood examined (~0.2% of total volume).[75] This limitation is complicated further by the extremely rare population of circulating entities in blood amidst an overwhelming number of normal hematopoietic cells. *Ex vivo* methods also are limited to peripheral sampling and may overlook certain CTC rich regions of the circulation. Additionally, *ex vivo* monitoring does not allow for longitudinal real-time surveillance.

Fluorescence based i*n vivo* detection/imaging approaches circumvent the limitations of *ex vivo* methods and include imaging methods such as confocal and diffuse optics flow cytometry.[76-78] Many of these imaging systems use bulky and expensive hardware components such as photomultiplier tubes and complicated light collection optics.[12] None of these system operate completely (both excitation and emission) in the near infrared (NIR) wavelength range which is advantageous for *in vivo* imaging. NIR excitation and emission because of its greater tissue penetration than visible light and minimal interference from tissue auto-fluorescence. NIR light allows for imaging/detection of fluorescence clusters in blood with greater sensitivity and may allow applications in deeply seated and larger blood vessels.

In this study, we designed and validated an approach that allows for all near infrared (NIR) planar fluorescence imaging (Excitation/Emission – 784 nm/ >808 nm) for imaging and size stratification of rapidly circulating fluorescent entities in blood. To achieve NIR contract in circulating cells, we treated cancer cells *ex vivo* with a NIR fluorescent molecular probe (LS301) which has been shown to target cancers *in vivo* in mice with high specificity.[79] Our planar imaging system uses CCD sensor based imaging, which can be easily integrated into a miniaturized set-up as needed. We developed an algorithm for size stratification of entities flowing through a field of view, and demonstrated the performance of our algorithm by accurately detecting the size of fluorescent microbeads flowing through a capillary mimicking blood flow. We then employed the same algorithm for the detection of a mixture of tumor cells and clusters in blood. Finally, we demonstrated longitudinal imaging of fluorescently labelled cells *in vivo. In vivo* imaging highlights that this approach could be executed by monitoring a patient peripherally or via an implant in a CTC rich region of the circulation. This affordable and compact technology has

several advantages including the ability for rapid miniaturization for the translation and implementation of this technique.

7.2 Methods

7.2.1 Cell Culture and Treatment

All experiments were performed using murine breast carcinoma cell line (4T1-Luc-GFP). The cells were cultured in DMEM supplemented with 10% fetal bovine serum and 1% Pen-Strep. For the cell experiments, the cells plated in culture plates in culture media with 40 μM LS301 and 400 mg/L calcium chloride (to enhance probe internalization) and incubated for 6 h at (37˚C, 5% atmospheric CO2). Cells were washed and imaged using an epifluorescence microscope (Olympus BX51), λex/em = 775nm/810 nm LP. After the initial images were obtained, cells were treated with trypsin and re-suspended in either PBS or heparinized porcine blood. To obtain single cell rich suspensions, post trypsinization cells were pipetted (1mL pipette tip) gently ~20 times and filtered through a cell strainer (40 μM mesh size). In contrast, to obtain clusters rich suspension cells were incubated in trypsin for lesser time and exposed to minimal pipetting.

7.2.2 In vitro Imaging

In order to test our method of detecting CTCs, we developed an imaging setup consisting of a microscope and an excitation light source. The microsphere in water, tumor cell in media, or tumor cell in blood mixture was passed through a 0.015 in ID x 0.033 in OD polyurethane tube (PU-033, SAI Infusion Technologies) at a flow rate of 3 mm/sec. Imaging was conducted using a microscope (Leica MZ10F) at 80x magnification. Calibration imaging was conducted using Fluoresbrite® YG Microspheres (Polysciences, Inc.) with a 10 μm diameter because NIR

microspheres in a cellular diameter were not available. Excitation was provided via a 460 nm LED (ThorLabs), with a 515 nm LP filter, for microsphere imaging. Excitation light power was measured at 0.8 mW/cm^2. NIR imaging was conducted using a 793 nm laser (BWT Beijing), set to a power output of 10 mW/cm^2, and the emission light was filtered using an 808 nm LP filter. The *in vitro* imaging configuration is shown in **Figure 7-1a**. The microspheres were imaged using the microscope input light port instead of external illumination. Image files were recorded in video files using a NIR sensitive camera (Fluorvivo 1500 BG, INDEC Biosystems) with an exposure time of 100 msec.

7.2.3 In vivo Imaging

In vivo imaging was conducted using the same microscope as *in vitro* imaging, however the light configuration was modified (**Figure 7-1b**). Excitation was provided via the microscope light port using a 780 nm LED (ThorLabs), with an 808 nm LP filter. Excitation light power was measured at 7.3 mW/cm^2. Internal thoracic artery imaging was conducted with an exposure time of 500 msec. 50 μL of PBS containing CTCs was injected into the left ventricle of a sacrificed mouse while the heart remained beating. Cells were imaged as they were pumped from the heart into the circulation (**Figure 7-1c**).

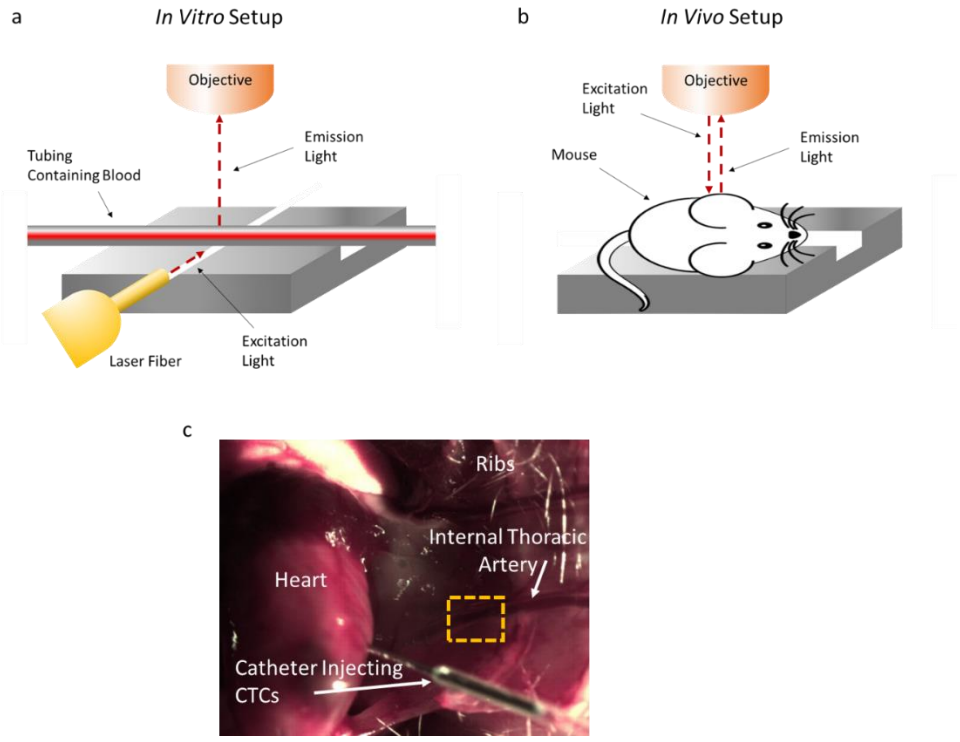

Figure 7-1: a) *In vitro* setup showing the optical configuration. An external light source was used to illuminate tubing containing CTCs in either PBS or blood. The image was magnified using the objective and recorded in video files using a NIR sensitive CCD. b) *In vivo* setup showing LED illumination through the microscope. c) View of *in vivo* imaging cavity showing the heart and thoracic artery. The yellow box highlights the area that was imaged.

7.2.4 Algorithm to Distinguish CTCs from Cell Clusters

We developed an image processing algorithm to analyze video recordings of circulating objects in our imaging setup. We developed our algorithm first using fluorescent tumor cells in media before moving to cells in blood and then *in vivo* imaging. The algorithm was validated using microspheres with known diameters. The algorithm analyzes the video files frame-by-frame with the user selecting a vertical line within the first frame (**Figure 7-2a**). That vertical line is used frame-by-frame to generate intensity profiles along that line (**Figure 7-2b**). The user inputs a threshold value, above which any pixels are considered an object. Subsequent pixels along the line are followed until the values rise above and then fall below the threshold. The length of subsequent

pixels above threshold are the object height (*h*). The midpoint of the pixels above the threshold is recorded as the midpoint of a unique object. The same line is examined in the subsequent frame, and if the midpoint is within a certain distance of the first midpoint, it is considered the same object. The object is tracked until a frame is reached where an object with the same midpoint is absent, thus ending the object.

The time for an object to completely pass through the vertical line is captured using the width in time (τ) as calculated using **Eq. 1**. Where *fn* is the number of frames, and *fr* is the frame rate. The velocity (*v*) is calculated by assuming that the distance the object is occupying in the y-dimension is similar to the distance in the x-dimension, and then using **Eq. 2**. The object area (*A*) is calculated by multiplying the height by the physical width (*w*) in **Eq. 3**. The object physical width is a function of the velocity and time for the object to pass, so it is estimated using **Eq. 4,** which is substituted into **Eq. 3**, to derive **Eq. 5**. **Eq. 5** is then used to calculate the relative object area. The term relative is applied in this case because the area is represented by a height multiplied by a width, using the simplifying assumption that the object is rectangular. However, even with this assumption, the relative sizes of single cells and cell clusters can be compared.

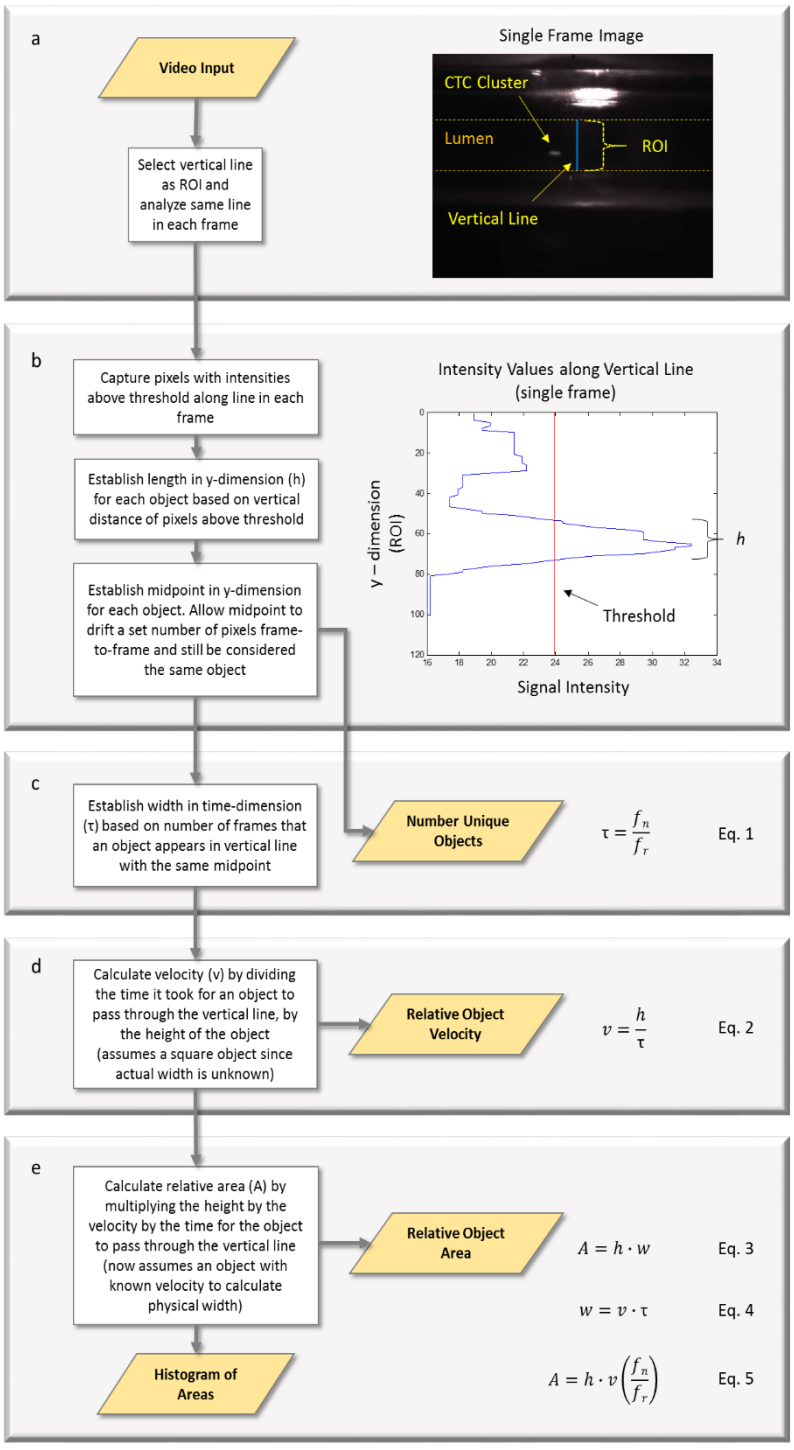

Figure 7-2: a) Single frame showing a CTC in media. b) Signal intensity along a vertical line for a single frame. c) Method for estimating the number of objects passing through the vertical line. d) Method for detecting the relative object velocity. e) Method for calculating the relative object 2D area.

7.3 Results

7.3.1 Algorithm Validation

Our algorithm was validated using fluorescent microspheres in media. We selected microspheres with diameters similar to that of our CTCs. **Figure 7-3a** shows a frame containing multiple microspheres, with the relative fluorescence intensities frame-by-frame (along the vertical line) in **Figure 7-3b**. The relative velocities of each object detected are shown in **Figure 7-3c** overlying the intensity map. The relative areas are represented visually as a function of time in **Figure 7-3d**, and the histogram of the calculated areas is shown in **Figure 7-3e**. The microspheres had a diameter of 10 μm, and using the algorithm area calculation method the idealized area would be 100 μm^2 (assumes 2D square geometry). The algorithm histogram predicted object areas clustered around 100 μm^2, thus confirming the accuracy of the algorithm. The detected object heights were output and plotted in **Figure 7-3f**, and they closely represent the microsphere diameter values, with a mean value of 10.81 ± 6.643 μm. Some of the cause of error may have been from multiple spheres passing at the same time, background fluorescence, and out of plane scattered light.

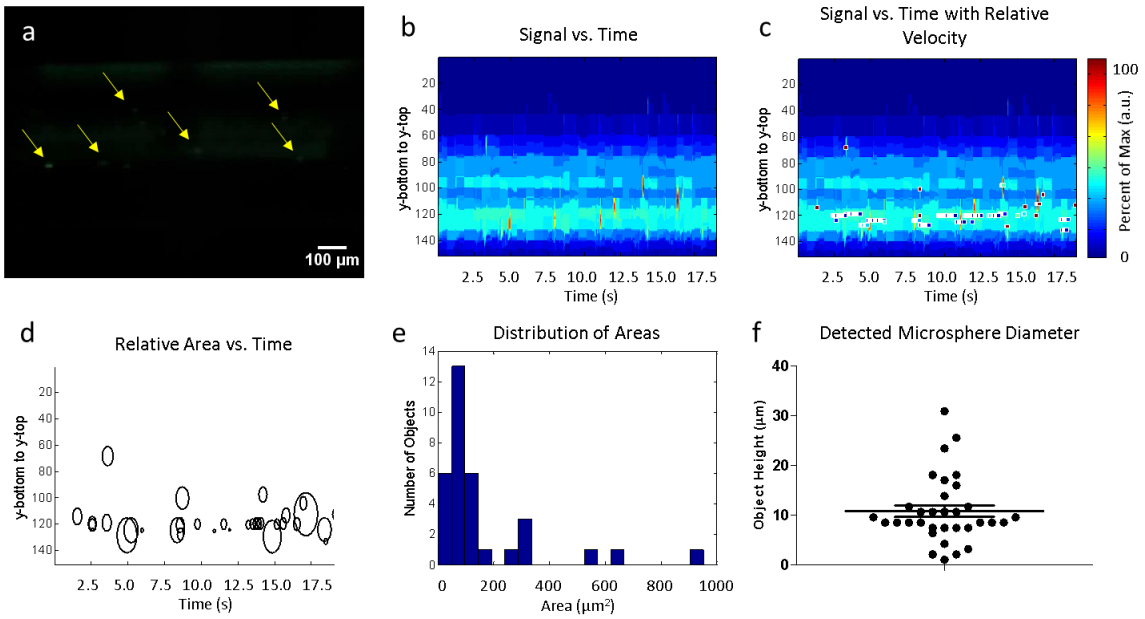

Figure 7-3: a) Circulating microspheres in media (yellow arrows). b) Microsphere signal intensity vs. time. c) Relative object velocity. Line of squares indicates the same object, and the length of the line of squares indicates the duration that the object took to pass through the vertical line. The color of the squares represents the relative velocity (red max and blue min). d) The relative object areas shown visually over time. e) Histogram of the distribution of object areas over the full time of imaging. f) Plot of individual microsphere diameters detected using the algorithm.

7.3.2 CTCs in Media

We then tested our detection system and post-processing algorithm by imaging CTCs in media. The cells were incubated in our fluorescent dye, and then imaged using NIR light. **Figure 7-4a** to **Figure 7-4c** show the fluorescent tumor cells in culture. For the initial study the cells were harvested and re-suspended in media, for later studies they were re-suspended in blood as shown in **Figure 7-4d** to **Figure 7-4f**.

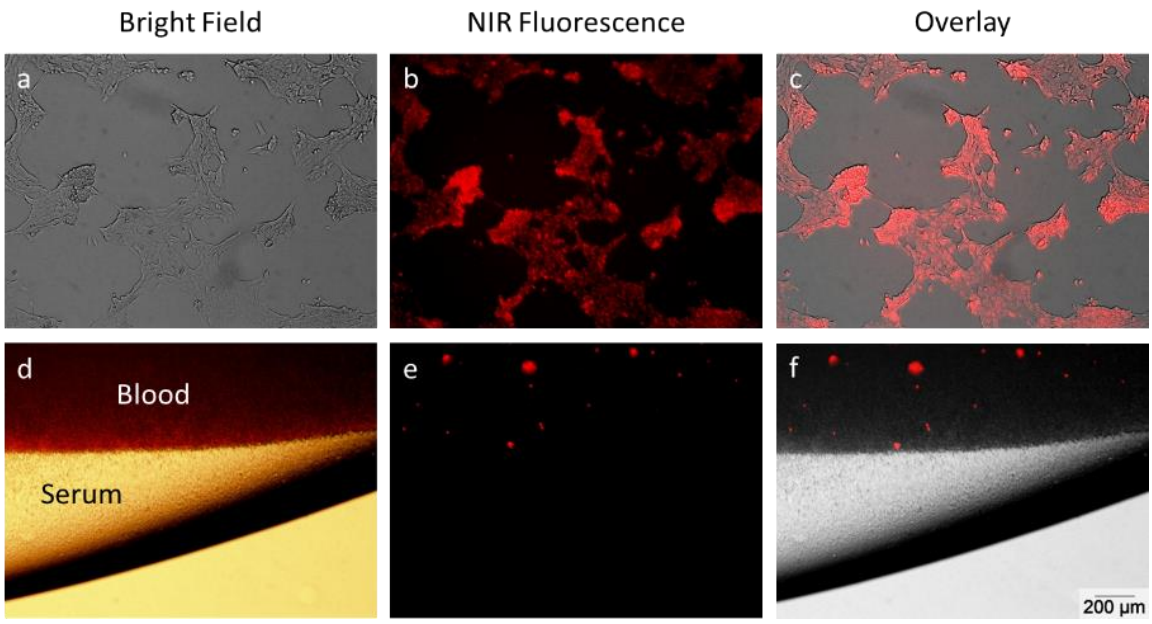

Figure 7-4: a) Bright field image showing cells in culture prior to re-suspension. b) NIR fluorescence image of labeled cells. c) Overlay image showing correspondence of NIR signal with cellular location. d) Bright field image showing CTCs after resuspension in blood. e) NIR fluorescence image of cells in blood. f) Overlay image showing the location of the fluorescence signal within the blood.

The goal of our algorithm was to differentiate small individual CTCs from large CTC clusters. To accomplish this, we first suspended individual cells in media via vigorous pipetting during re-suspension, then we compared our findings to larger clusters with reduced pipetting. **Figure 7-5a** shows a video frame containing a fluorescent CTC passing through the field of view. **Figure 7-5b** is an intensity map of the vertical line across all of the video frames under analysis (sub-frames). The relative velocities for each object detected were represented by boxes overlying the intensity map (**Figure 7-5c**), and the relatives areas are represented in **Figure 7-5d**. The distribution of object areas observed within the sub-frames analyzed were displayed in a histogram (**Figure 7-5e**). The algorithm was able to detect 10 objects out of the 13 objects observed in the video for a sensitivity of 76.9%. Some objects were below the fluorescence intensity threshold and were not detectable. We then analyzed our video containing large clusters. In this video the clusters

were traveling faster at the beginning of the video, and then slower over time. This trend is reflected in the relative velocities reducing at later time points (**Figure 7-5f**). The relative areas were significantly larger than the previous video, as evident in **Figure 7-5g** and **Figure 7-5h**. Because the cells were moving very rapidly at the beginning of the video, it was not possible to discern the sensitivity of detection. Of the clusters that were detected the algorithm was able to detect a difference in size as compared to individual cells, with the clusters much larger than the individual CTCs.

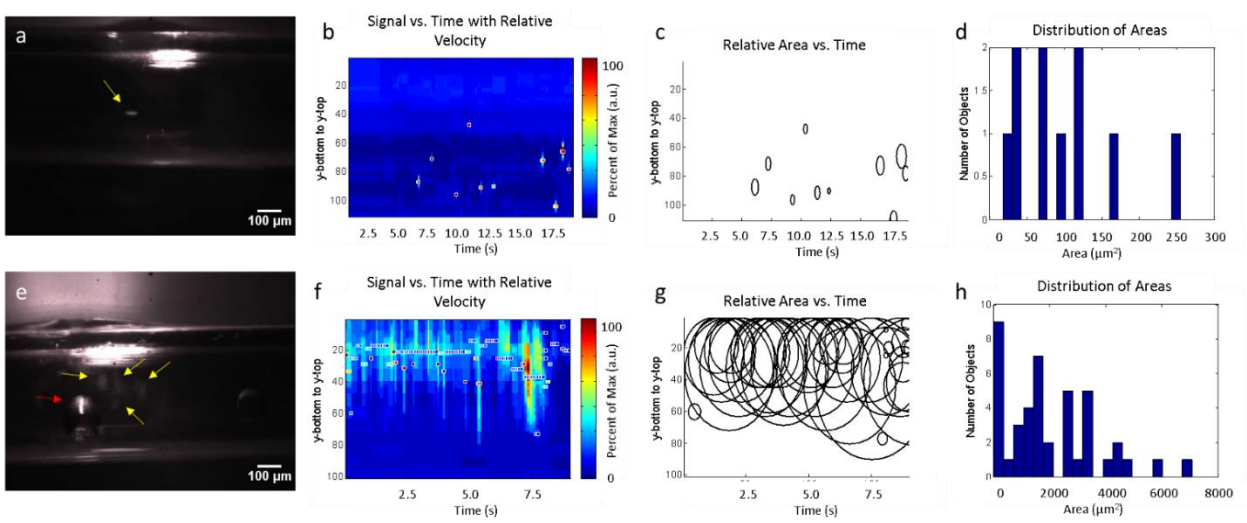

Figure 7-5: a) NIR image of CTC in media (yellow arrow). b) Relative velocity of each CTC detected. c) Relative area of each CTC detected. d) Histogram of the object areas for individual CTCs. e) NIR image of CTC clusters in media (yellow arrows). Red arrow indicates bubble that was not a CTC cluster. f) Relative velocity of each CTC cluster detected. g) Relative area of each CTC cluster detected. h) Histogram of the object areas for CTC clusters.

7.3.3 CTCs in Blood

Next, we imaged CTCs in blood to determine if our detection system was capable of detecting fluorescence in a scattering medium. The blood was opaque in appearance, and the red blood cells (RBCs) scattered our excitation light (**Figure 7-6a**). We were able to obtain video as

shown in **Figure 7-6b**, however individual changes in intensity due to CTCs were not as readily apparent as when imaging through media. **Figure 7-6c** shows the detected cells and velocities, and **Figure 7-6d** and **Figure 7-6e** show the areas of the CTCs detected. When we ran the post-processing algorithm on our control groups of blood only, and non-fluorescent CTCs, the algorithm did not return any detected cells. Therefore, the algorithm was able to detect the presence of CTCs, although the relative areas cannot be verified visually do to the reduced contrast between the fluorescent cells and blood.

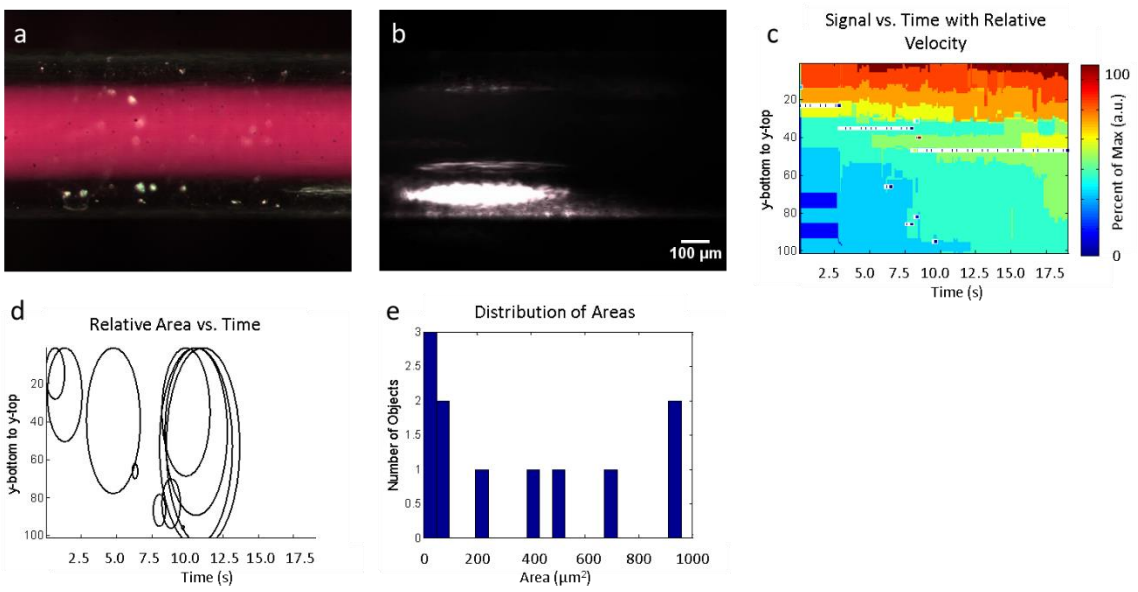

Figure 7-6: a) Bright field image of CTCs in blood in tubing. b) NIR image of CTCs (not visible) in blood. c) Relative velocity of CTCs in blood as detected using the algorithm. d) Relative areas of CTCs in blood. e) Histogram of the object areas detected.

7.3.4 CTCs in vivo

Next, we imaged CTCs *in vivo* by injecting labeled cells into the left ventricle then imaging the CTCs in the circulation. **Figure 7-7a** shows a bright field image of the internal thoracic artery of a mouse. We first injected a NIR dye to visualize the vessel (**Figure 7-7b**). The NIR dye showed a local area of intensity (red arrow), however this object was not flowing with the circulation and

was present prior to injecting our CTCs, so it was not a CTC. We then injected our CTCs into the heart and imaged the downstream artery to visualize the movement through the circulation (**Figure 7-7c**). A single CTC was visible as it passed through the field of view, and it was detected using our algorithm (**Figure 7-7e** and **Figure 7-7f**). The estimated object area was 113 μm^2, supporting the detection of a single CTC rather than a cluster (**Figure 7-7g**). We next injected cell clusters into the heart and repeated our imaging and analysis (**Figure 7-7h** and **Figure 7-7i**). The algorithm detected the presence of multiple objects of larger areas than single CTCs, suggesting the presence of clusters (**Figure 7-7j**).

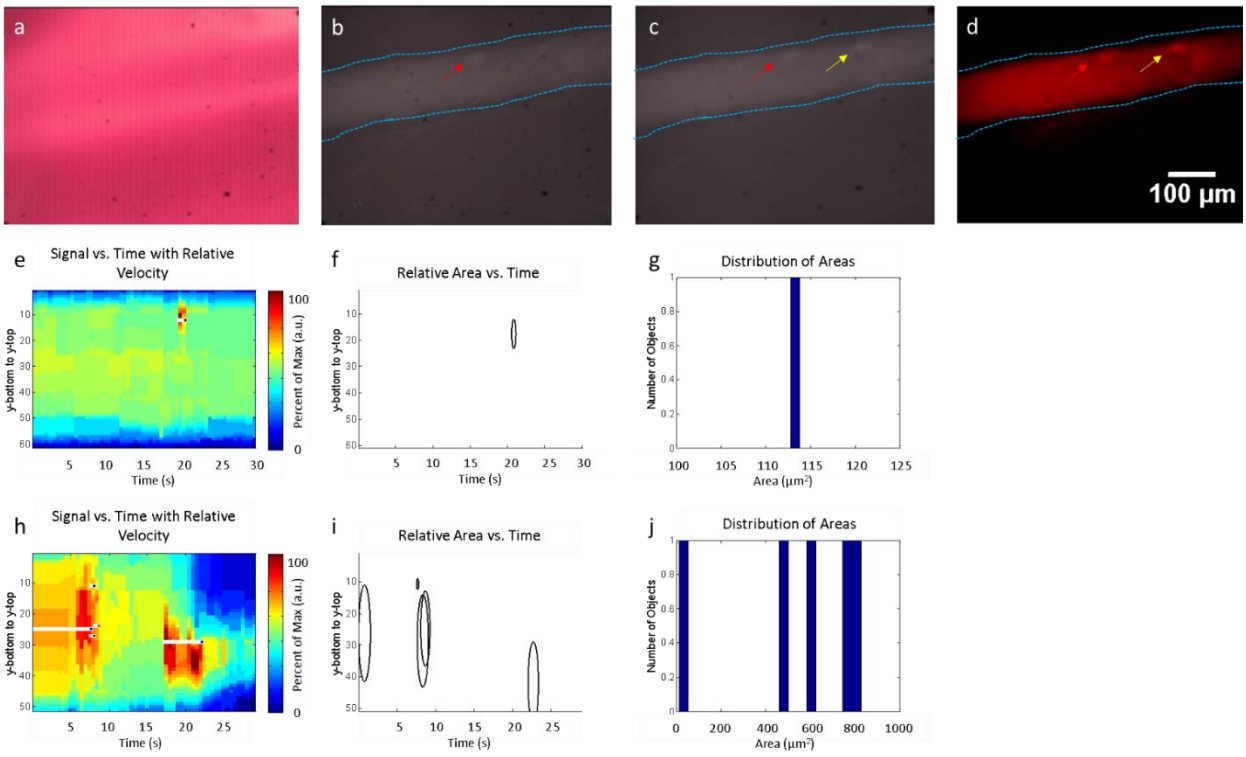

Figure 7-7: a) Bright field image of internal thoracic artery. b) NIR dye injected into artery highlighting it with arterial borders outlined in blue. Static fluorescent object that was not a CTC (red arrow). c) NIR image of CTCs post intra-cardiac injection (yellow arrow). d) Enhanced NIR image to aid in visualization of CTC from c (yellow arrow). e) Relative velocity of individual CTCs *in vivo*. f) Relative area of the individual CTC detected. g) Histogram of the object area for the CTC. h) Relative velocity of each CTC cluster detected. i) Relative area of each CTC cluster detected. j) Histogram of the object areas for CTC clusters.

7.4 Discussion

We developed a detection scheme that allowed for the imaging and detection of CTC, and the differentiated the single CTCs from CTC clusters. Additionally, we validated our method and demonstrated the *in vivo* application. NIR light has advantages over visible light of reduced scattering in blood, increased imaging penetration depth, and decreased auto-fluorescence due to endogenous fluorophores. We chose to use a CCD for our detection device to allow for future translation of our technique. Because we use a simple CCD along with magnification and a light source, a device could be constructed that combines these elements for versatile imaging.

One limitation of the technique was that the CTCs needed to emit a bright signal to be detectable in blood. We achieved this via incubation of cells with calcium *ex vivo*. Presumably, and *in vivo* labeling technique could be developed that allows for bright signal emission from cells, possibly using nanoparticle technology. Another limitation of the technology was that the threshold used to determine the presence of a CTC was determined at the time of image analysis. This was necessary because the light and location of detection would need to be consistent in order to set a consistent threshold. Achieving a consistent threshold would be achievable with the development of a stand-alone device with consistent lighting and imaging configurations. A stand-alone device would be ideal for the versatile imaging of CTCs in different anatomical locations. Developing this technology could aid in the fight against cancer through the early detection and prevention of tumor metastases. Patients could be stratified based on size of CTC clusters and their therapy and surveillance programs could be tailored to match their individual prognosis.

Our imaging method for CTC size stratification demonstrates that CTCs and CTC clusters can be detected and assessed *in vivo* using NIR fluorescence. We demonstrated that an algorithm could be used to classify moving fluorescent structures based on minimal input data.

Improvements in the miniaturization of the technology, and increasing the cellular fluorescence signal, would allow for the translation of this technology to improve cancer treatment for the numerous patients impacted each year.

7.5 Conclusions

We have now explored the structural characterization of primary tumors, the identification of secondary tumors, and the size stratification of circulating tumor cells. Each of these methods focuses on the diagnostic aspects of fluorescence imaging. In the next chapter we focus on tumor therapy; using light to treat disease.

Chapter 8 :

Theranostic Molecular System Comprising a Photosensitizer and a Near Infrared Fluorescent Probe Enables Spatiotemporal Imaging and Treatment of Squamous Cell Carcinoma

8.1 Introduction

Non-melanoma skin cancer (NMSC) is comprised of both squamous cell carcinoma (SCC) and basal cell carcinoma, and is the most common cancer worldwide impacting an estimated 2 to 3 million people each year. SCC accounts for approximately 20% of NMSC diagnosed, making it a considerable portion of all cancers. [80] Cutaneous SCC is caused by a malignant transformation of epidermal keratinocytes that leads to tumor formation, and has been linked to a number of risk factors including exposure to ultraviolet light, aging, light skin type, and chronic inflammation. [81-85] Unlike basal cell carcinomas, SCCs have high metastatic potential, requiring the development of effective treatment strategies. [80]

Numerous treatment options are available for cutaneous SCC. However, large-scale clinical studies have yet to determine a superior treatment option. [86,87] One option for treating SCC is photodynamic therapy (PDT), where light is used to activate a photosensitizer (PS) that in turn induces cell death. Methyl-δ-aminolevulinic acid-PDT (MAL-PDT) is the most common form of PDT for NMSC. Although MAL-PDT can successfully treat 70 to 90% of NMSC, it has not been successful in treating invasive SCC cases. This unfavorable result is likely because MAL-PDT relies on the focal nature of lesions, as the PS is topically applied in suspicious regions. When invasion occurs in more advanced cases of SCC, the topical application of methyl-δ-aminolevulinic acid becomes less practical because of the difficulty in identifying the exact tumor location.

To overcome the limitations in delivering the PS to metastases and invasive portions of the tumor, several targeting methods have been used, such as: nanoparticle formulations, antibodies, and peptide ligands. [88-90] For visualization, most of these compounds rely on the fluorescence

produced by the PS, which tends to have low quantum yields, and therefore low signal. In addition, the fluorescence is the visible range which interferes with auto-fluorescence.

Therefore, we developed a theranostic bioconjugate (LS797) which combines a peptide targeting ligand (cGRD) [79,91], an efficient PS (Ce6), and a NIR imaging molecule (cypate), to create a compound that addressed some of the challenges of clinical PDT. We used LS797 in a skin cancer model (SCC-12) to conduct PDT *in vivo*.

8.2 Methods

8.2.1 In vitro Cell Uptake

Uptake assays were conducted using the human skin cancer cell line, SCC-12, and the murine fibroblast cell line, 3T3. Cells were cultured on an 8-well slide, (BD Biosciences, NJ, USA), with a 4:1 ratio of SCC-12 cells to fibroblasts. The fibroblasts were GFP-expressing. Cells were incubated with 1 μM of LS797 for 4 or 24 hours, washed with PBS and imaged. Confocal microscopy was performed using an FV1000 confocal microscope with a UPLanApo/IR 60X/1.20W water immersion objective lens (Olympus, PA, USA) at 488 nm (GFP) or 785 nm (cypate) excitation laser, and fluorescence was detected at 550/50 nm (GFP), or 850 LP (cypate).

8.2.2 In vitro Photodynamic Therapy

SCC-12 cells were cultured in MatTek dishes (MatTek, MA, USA). Individual dishes were either left untreated, exposed to light at 35 mW/cm^2, for 5, 15, or 30 minutes, incubated with LS797 for 4 hours, or incubated with LS797 for 4 hours and then irradiated. After each treatment was completed, cells were incubated with 1 μM of the caspase-9 sensor, CaspaLux® 9-M2D2, (OncoImmunin, MD, USA) for 30 minutes, and imaged using a confocal microscope (details in

above) at 543 nm excitation, and 600/25 nm emission. The cultures were then grown for 3 days, after which they were stained with 0.5 μM of the cell death marker, EthD-1, for 45 minutes and imaged on the confocal at 543 nm excitation and 600/25 nm emission.

8.2.3 Tumor Model Development

All animal studies were performed in compliance with the Washington University Animal Study Committee's requirements for the care and use of laboratory animals in research. Squamous cell carcinoma xenografts were initiated using SCC-12 by injecting approximately 2.5 x 10^6 cells into the bilateral shoulder and flank regions of 6-8 week old female athymic NCR-nu/nu mice (22 – 25 g). The SCC-12 cells were injected into the intradermal compartment. Tumors were allowed to grow until they were visible and measurable. In some cases, the tumors did not graft, and these regions were not included in the study. The tumor volume was calculated by measuring the length and width of each tumor, and recorded as calculated $V = LW^2$, where *V, L, and W* are the tumor volume, length, and width, respectively.

8.2.4 In vivo and ex vivo Imaging

LS797 was dissolved in 20% DMSO and diluted in 80% PBS to a final concentration of 0.5 mg/kg dose for imaging, or a 6.8 mg/kg dose for therapy. All doses were administered via a 100 μl tail vein injection. The corresponding Ce6 doses were 0.1 mg/kg and 2.0 mg/kg for imaging and therapy studies, respectively. [92,93] Fluorescent imaging was performed using the Pearl NIR fluorescence imaging system, ex/em 785/820 nm (LICOR Biosciences, NE, USA) before injection and up to 24 hours post injection. After 24 hours, the mice were euthanized and organs of interests were removed, placed on a petri dish, and imaged with the Pearl imager. The region of interest (ROI) analysis was performed with the Pearl imaging software. The mean fluorescence intensities were measured for each tissue type to assess the bio-distribution of each compound.

8.2.5 In vitro Photodynamic Therapy

At 4, 8, and 24 hours after a 6.8 mg/kg injection of LS797, the treated tumors were irradiated for 30 minutes. Therapeutic light doses were administered using a 650 nm laser with a power output of 35 mW and a beam area of 1.0 cm^2. For control mice, there was no injection of LS797 and a subset of the tumors was irradiated to obtain untreated controls and light only controls, respectively. For mice injected with LS797, a subset of the tumors was irradiated to obtain LS797 only controls and PDT (LS797 + light).

8.2.6 Histological Analysis

Excised tumor tissues were flash-frozen in OCT (Tissue Tek, CA, USA) and stored at –20 ^oC. The tumors were sliced at a thickness of 10 μm (Cryocut 1800, IL, USA). Immunohistochemical staining of excised tumor and surrounding tissues was used for histologic validation of tissue types. Immunohistochemistry (IHC) was conducted using an immune-peroxidase method. Primary antibody was diluted in DaVinci Green (BioCare, CA, USA) at the following dilutions: Ki-67 (Thermo Scientific, MA, USA) 1:400, CK-10 (Abcam, MA, USA) 1:400, CK-8/18 (Abcam, MA, USA) 1:200, E-Cad (Abcam, MA, USA) 1:200. Anti-rabbit secondary antibody (Perkin-Elmer, MA, USA) was diluted in PBST at a dilution of 1:800, Streptavidin (Jackson Labs, PA, USA) in PBST at a dilution of 1:1600. A polymer method was used for p53 and CC3 staining with the following dilutions: p53 (Cell Signaling Technology, MA, USA) 1:100, and CC3 (Cell Signaling Technology, MA, USA) 1:10,000. Universal Polymer (Biocare, CA, USA) secondary antibody was diluted in PBST 1:4. All IHC was conducted by the Digestive Diseases Research Core Center – Advanced Imaging and Tissue Analysis Core (DDRCC-AITAC) at the Washington University School of Medicine, St. Louis, MO. Microscopy was performed with an Olympus BX51 upright microscope (Olympus America, PA, USA).

8.3 Results

8.3.1 Skin Cancer Model Characterization

We first sought to develop a cutaneous SCC model that would be appropriate for the assessment of PS accumulation in tumors and subsequent PDT. Chemical carcinogenesis animal models have previously been developed using a two-step approach of initiation and promotion. This method generates tumors on the skin after a progression from normal, to papilloma, to differentiated SCC, and then to poorly differentiated SCC. [94] Typically, this process occurs within 20 to 50 weeks, with varying percentages of carcinoma formation. We investigated an orthotopic model in order to decrease the time to tumor development and increase the yield of tumors. An SCC-12 orthotopic model was first developed by culturing cells derived from cutaneous SCC biopsies and injected them into nude mice. [95]

We sub-dermally injected SCC-12 cells into the shoulders and flanks of nude mice, and were able to develop tumors within 14 days. These tumors grew in volume for over a month with a doubling rate of 9.45 ± 3.91 days, and progressed through different morphological states (**Figure 8-1a)**. The tumors initially appeared as small bumps, next they became erythemic with cystic spaces, and finally they became ulcerative with a central clearing. This final state resembled the gross appearance of cutaneous SCC in humans (**Figure 8-1b**). [96]

After establishing the growth characteristics, the cutaneous SCC-12 model was examined using immunohistochemistry (IHC) staining (**Figure 8-1c, Figure 8-1d**). The tumor was sectioned so that the epidermal and dermal layers were visible. Cytokeratin-10 (CK-10) is a type-1 keratin that is produced by keratinocytes and is typically located in the epidermis of normal skin. Mutations in the gene encoding CK-10 are linked to hyperproliferative disorders. [97] CK-10 was expressed in the epidermis of both the normal skin and the tumor. However, the tumor had

epidermal thickening and more extensive CK-10 expression. There were small regions of CK-10 expression found throughout the dermis and within the tumor, but these dermal regions of CK-10 expression were not present in healthy skin. Cytokeratin-8 and 18 (CK-8/18) are expressed by secretory epithelia, absent from non-secretory epithelia, and expressed by a range of malignant cells. CK-8/18 was absent from the normal skin, however it was found throughout the tumor section in both the glandular regions and the cellular tumor region. The tumor suppressor gene protein p53 expression is common in cutaneous SCC tumors that originate from ultraviolet DNA damage [80], and has been shown to be expressed in SCC at higher levels than normal skin. [5,98] p53 was largely absent from the normal skin section and present in the tumor section. [99,100] E-Cadherin was the same between the skin and tumor, indicating that the intracellular epithelial junctions remained intact in our tumor model. Ki-67 is a marker of cell proliferation that is upregulated in cutaneous SCCs compared to normal skin. [99,100] Our model demonstrated increased Ki-67 staining as compared to the healthy skin. Cleaved caspase 3 (CC3) is a marker for cell apoptosis, which was present in the tumor section and largely absent from the skin. The presence of both Ki-67 and CC3 in the tumor indicated that there was increased cellular turnover.

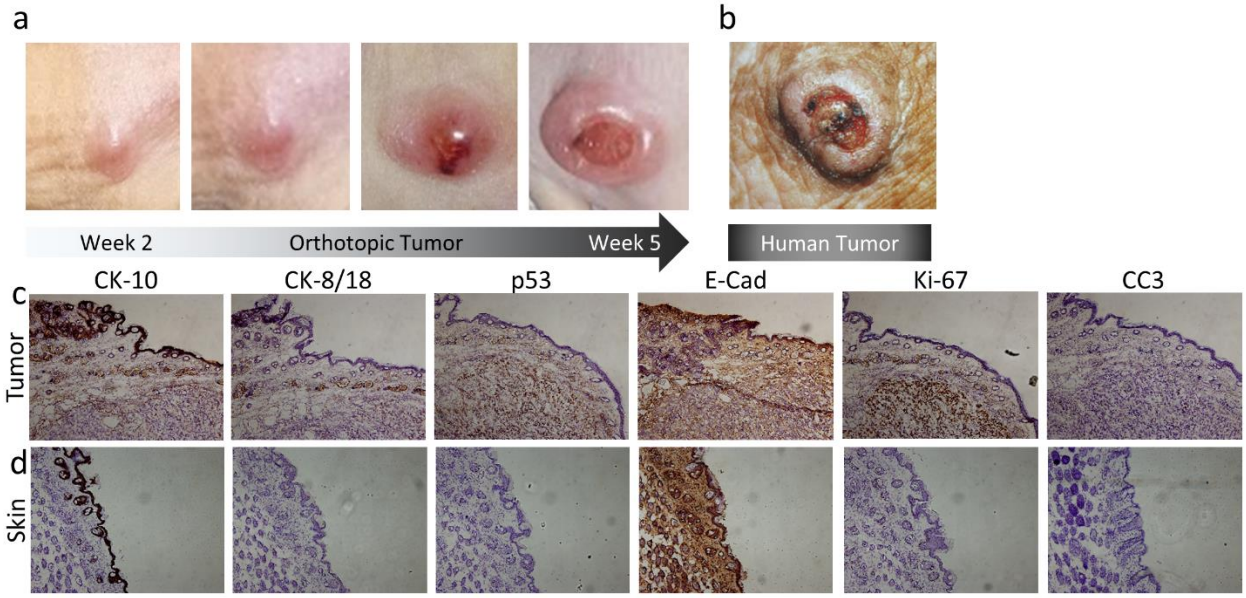

Figure 8-1: Characterization of SCC-12 model formed through subdermal injections of SCC-12 cells. a) Morphologic growth characteristics of SCC-12 xenograft, b) Human SCC, image adapted from [96]. c) SCC-12 IHC of tumor, and d) normal skin. Microscopy conducted at 10x magnification.

8.3.2 LS797 Spectral Properties

LS797 was synthesized through the conjugation of LS301 [11] to Ce6. LS301 served as the tumor targeting and NIR imaging agent (cypate), while the Ce6 acted as the PS. The resulting LS797 bioconjugate contains the three characteristic absorption peaks of Ce6 at 400 nm, 500 nm and 650 nm, and the absorption peak for cypate at 780 nm. The emission peak of Ce6 was seen at 660 nm when excited at 630 nm and the emission peak of cypate was seen at 800 nm when excited at 720 nm. Due to the minimal spectral overlap of the two fluorophores, there were no spectral changes in the integrated molecule compared to the fluorophores on their own.

8.3.3 LS797 Targeting in vitro

To determine the tumor targeting ability of LS797, GFP-expressing 3T3 fibroblasts and SCC-12 cells were co-cultured before adding LS797 to the cultures for 4 or 24 hours. The mean LS797 fluorescence was greater in the SCC-12 cells compared to the fibroblasts, and the contrast

of signal from SCC-12 cells compared to fibroblasts increased over time, from 1.6 ± 0.3 at 4 hours to 2.8 ± 0.3 at 24 hours (**Figure 8-2a**).

8.3.4 LS797 Targeting in vivo

After determining that LS797 targeted tumor cells *in vitro*, we then moved to *in vivo* studies using an SCC-12 orthotopic model. An imaging dose of LS797 (0.5 mg/kg, 0.1 mg/kg Ce6) successfully identified tumors from the surrounding normal skin in each of the tumors imaged (**Figure 8-2b**), with an *in vivo* tumor to skin contrast of *1.5 ± 0.09* at 24 hours (**Figure 8-2e**). The kinetics of LS797 show that the compound was primarily localized to the tumors within 4 hours, and was retained after 24 hours. Twenty-four hours after LS797 injection, the mice were sacrificed to obtain a biological distribution of the compound (**Figure 8-2c**). LS797 accumulated in the tumor and the major excretion organs (**Figure 8-2d**). Because the region of interest for the tumors was the skin, the signal from the excretion organs did not obscure visualization of the tumors. The *ex vivo* signal contrast between the tumor and skin was *4.6 ± 0.4*.

A therapeutic dose of LS797 (6.8 mg/kg,) was administered to elicit a dose response to PDT. The kinetics of the therapeutic dose mimicked those of the imaging dose, with initial entry into all tissues followed by localization in the tumor within 24 hours. The kinetics of LS797 at therapy dose were virtually the same as imaging dose, with the maximum tumor fluorescence value occurring at 4 hours, and a higher tumor to skin contrast value at 24 hours.

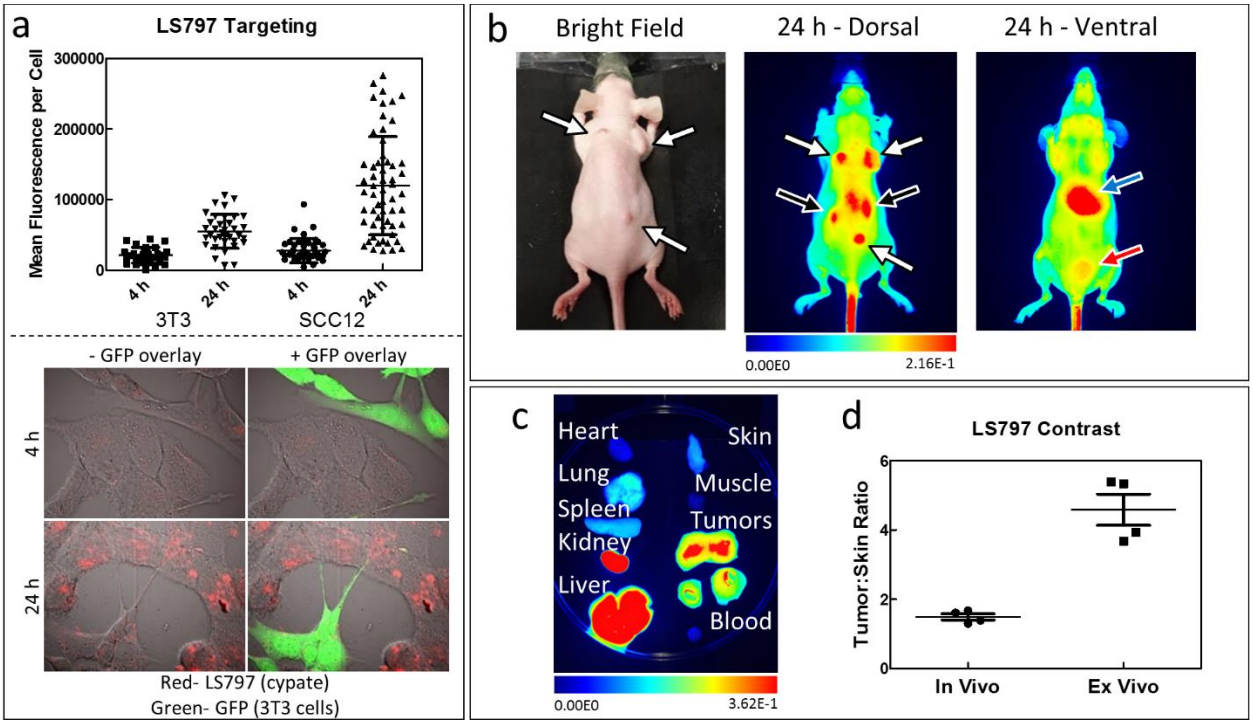

Figure 8-2: Targeting of LS797 in vitro and in vivo. a) Quantitative analysis of LS797 internalization into co-cultures of SCC-12 cells and 3T3/GFP fibroblasts. Each point represents fluorescence in a single cell. Representative images show LS797 (red) in SCC-12 cells and GFP (green) to distinguish the 3T3 fibroblasts. b) Bright field mouse image and NIR dorsal and ventral images at 24 hours post injection. Tumors (white arrows) apparent at 24 hours post injection. Fluorescence in the kidneys (black arrows), bladder (red arrow), and liver (blue arrow), show the renal and hepatic routes of excretion of the dye. c) Bio-distribution of a mouse injected with LS797. LS797 visible in tumors and excretion organs. d) *In vivo* and *ex vivo* tumor to skin contrast (n = 4). Figure courtesy of Dr. Rebecca Gilson.

8.3.5 LS797 Therapy in vitro

Once the imaging efficacy of LS797 was demonstrated, its therapeutic efficacy was tested. SCC-12 cells were incubated with LS797 (30 μM) for 4 hours and then irradiated with light (35 mW/cm^2) for 5, 15, or 30 minutes to obtain total doses of, 10.5, 31.5, and 63 J/cm^2, respectively. Caspase 9 activity indicates the activation of apoptotic pathways. Increased caspase 9 activation was seen in cells that were irradiated for 15 or 30 minutes. In contrast, only a baseline activation was seen in cells irradiated for 5 minutes (**Figure 8-3a** and **Figure 8-3b**). Three days after PDT, the cultures were stained with EthD-1 to visualize the dead cells remaining in the culture (**Figure**

8-3c and **Figure 8-3d**). EthD-1 stains the nuclei of dead cells. Control cell cultures showed sheets of cells with normal cell morphology and minimal EthD-1 staining, indicating cellular damage did not occur. The PDT cultures irradiated for 30 minutes showed high EthD-1 staining along with regions without intact cells. The PDT cultures irradiated for 15 minutes showed regions of morphologically healthy cells and regions of only debris. This variable regional morphology was supported by high levels of EthD-1 staining in some regions and low staining in others. The 15-minute irradiation group also exhibited lower caspase 9 activation, which may explain the limited cell death. The cells irradiated for 5 minutes showed normal morphology. The caspase 9 activation in these cells was similar to the baseline activation seen in the control cells. Based on the three light power settings examined, these findings suggest that cell death occurred in a light-dose dependent manner, and that 63 J/cm^2 was the minimum light power needed to achieve complete cell death *in vitro*. With lower light doses, caspase 9 activation was still observed, but it was not sufficient to cause apoptosis.

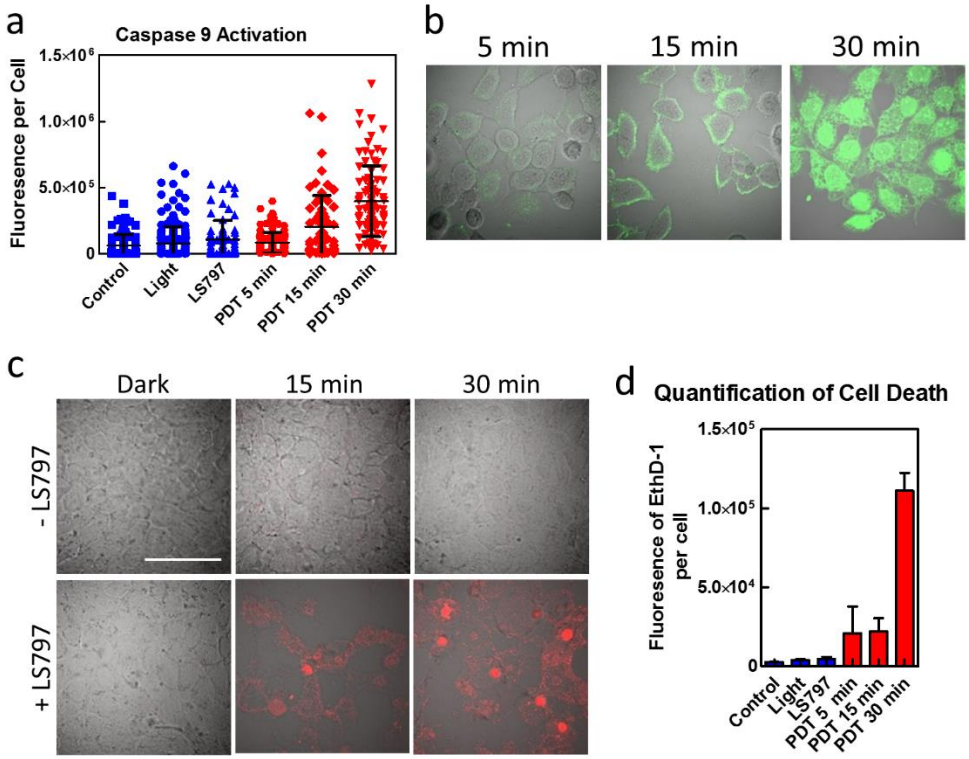

Figure 8-3: Photodynamic therapy in cells shows caspase 9 activation and subsequent cell death. SCC-12 were exposed to light, LS797 or both to determine the efficacy of PDT with LS797. a) Quantification of caspase 9 activation, 30 minutes after light delivery or at the corresponding time for cells that were not treated with light. b) Representative images of caspase 9 activation for the PDT-treated cells at different light exposures. c) Three days after PDT or control treatment, cells were stained with EthD-1, imaged to determine to morphology and the cellular viability. d) Cell death only occurred in the condition where both light and LS797 were present as shown by the quantification of the fluorescence of EthD-1 per cell. Figure courtesy of Dr. Rebecca Gilson.

8.3.6 LS797 Therapy in vivo

For *in vivo* PDT, LS797 was administered via tail vein injection and a 650 nm laser was applied at 4, 8 and 24 hours post-injection. The tumors that were not undergoing light therapy were masked. This approach allowed us to delineate the effects of PDT on tumor growth from LS797 treatment alone. The PDT setup consisted of an LED controller that modulated a 650 nm LED. The LED was used with a power output of 35 mW and a spot size of 1 cm^2, giving a total power density of 35 mW/cm^2. Each tumor received a total dose of 189 J/cm^2 over a 24-hour period.

The tumor growth was tracked by measuring the length and width of each tumor, and recorded as a volume. The tumor growth analysis consisted of an average change in tumor growth as a function of the original size, allowing each tumor to serve as its own control. The 24 hours between injection and the final light treatment were considered day zero. Tumor volumes were measured for 6 days before and after day zero and were compared. An average change in tumor volume (ACTV) was calculated for each tumor using **Eq. 8-1**.

$$ACTV = (Average(V_{D(1)} \text{ to } V_{D(6)}) - Average(V_{D(-6)} \text{ to } V_{D(-1)}))/ Average(V_{D(-6)} \text{ to } V_{D(-1)}) \qquad \textbf{Eq. 8-1}$$

Where day 0 is the day PDT occurred, $V_{D(-1)}$ is the tumor volume 1 day prior to PDT, $V_{D(-6)}$ is the tumor volume 6 days prior to PDT, $V_{D(1)}$ is 1 day post-PDT, and $V_{D(6)}$ is 6 days post PDT.

The tumors treated with LS797 and light initially swelled with PDT, then scabbed and shrank in size over a few days, as is common in PDT. The data showed that the tumors treated with LS797 and light resulted in a lower growth rate (ACTV) as compared to other treatment groups (**Figure 8-4a**). When tumors within a single mouse were compared for LS797 only vs. LS797 with light, the PDT tumors were visibly altered by the therapy (**Figure 8-4b**). Although the tumors exposed to solely light had a reduction in growth rate, the decrease was less than the PDT group, nor exhibit a scabbed appearance. This difference in appearance indicated that LS797 contributed to the enhanced cell death in the PDT group as compared to light alone.

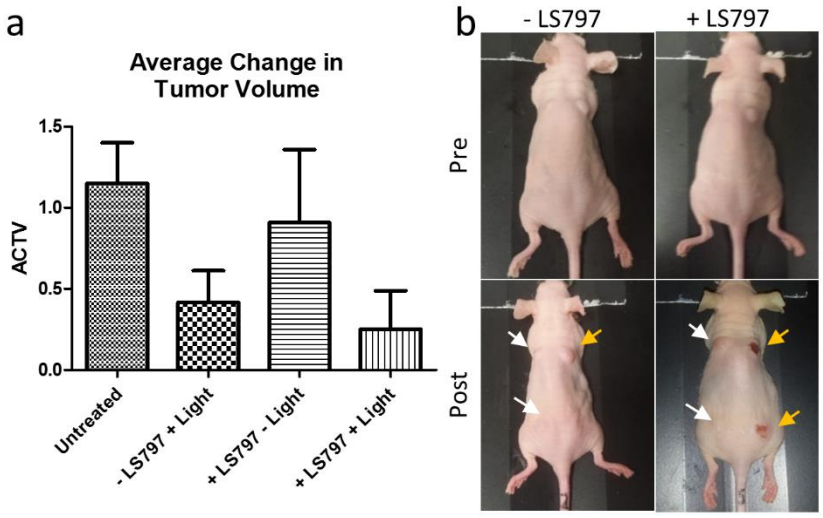

Figure 8-4: Photodynamic therapy in animals shows scabbing and decrease in tumor volume. a) Average change in tumor volume, ACTV, demonstrating a decrease in tumor growth for LS797 + light (n = 4), as compared to untreated (n = 3), light only (n = 3), and LS797 only (n = 3). b) Bright field images of a mouse receiving PDT or light, before and 24 hours after the start of therapy. Irradiated tumors indicated by yellow arrows and non-irradiated tumors indicated by white arrows.

The therapy resulted in a reduction in ACTV of 78% compared to untreated tumors. PDT suppressed the tumor volume for 6 days on average after initial treatment resulting in an overall decrease in tumor volume post therapy of 81% compared to the untreated controls (**Figure 8-5a**). At the conclusion of the study, only a small papule was present in the original location of the tumors treated with PDT (**Figure 8-5b**). IHC analysis of the tumor sections revealed that the PDT tumors had larger regions of apoptosis (CC3 staining) and smaller regions of cell proliferation (Ki-67 staining) compared to the untreated tumors (**Figure 8-5c**), indicating that a mechanism of reduced tumor volume can be attributed to the induction of apoptosis.

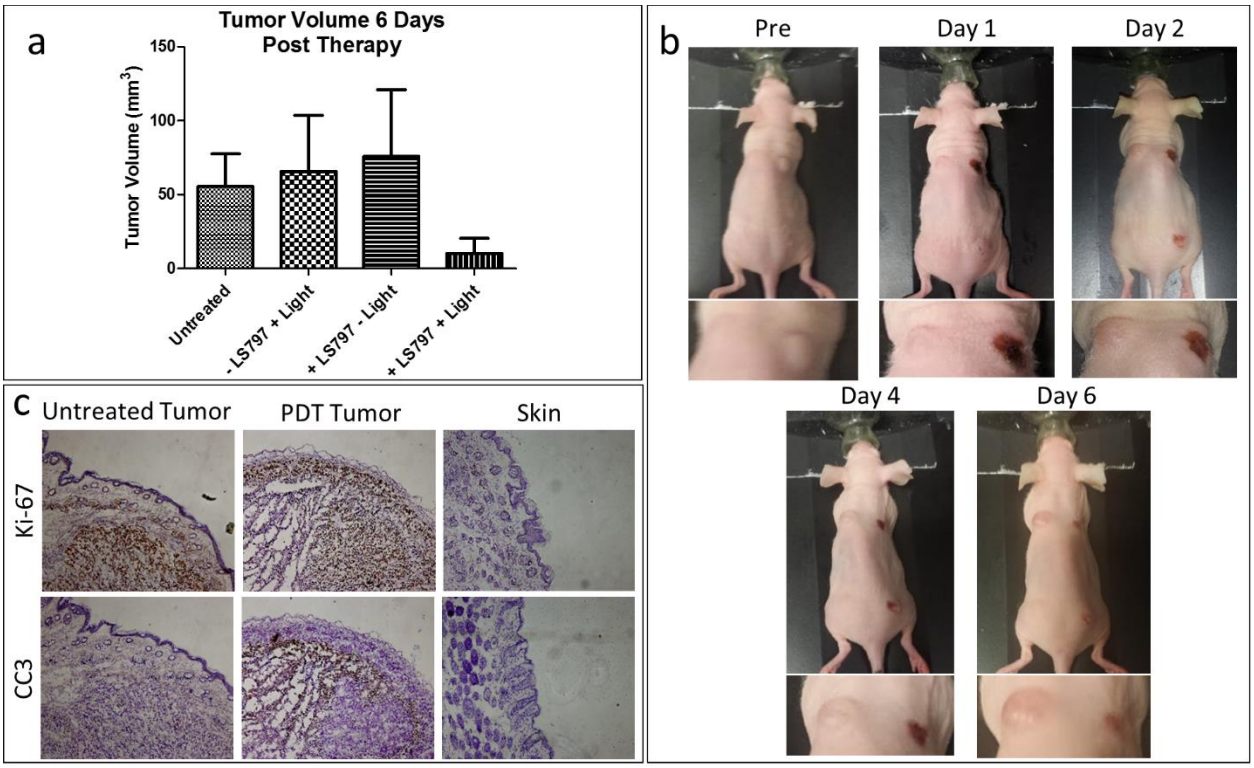

Figure 8-5: Long-term effects of photodynamic therapy. a) Tumor volume at 6 days post therapy, untreated (n = 3), light only (n = 3), LS797 only (n = 2), and LS797 + light (n = 2). b) Tumor morphological appearance pre and post therapy. c) IHC of the untreated tumor, PDT tumor, and skin stained for proliferation (Ki-67) and apoptosis (CC3). Microscopy conducted at 10x magnification.

8.4 Discussion

We characterized an orthotopic cutaneous SCC model that morphologically resembled human SCC. This orthotopic model developed measurable tumors within 2 weeks after cell injection. We demonstrated that this SCC-12 model had differential IHC expression of CK-10, CK-8/18, p53, Ki-67 and CC3, relative to normal skin. The increased Ki-67 and CC3 expression was indicative of the rapid growth and turnover of tumor cells in the dermis. [101] An increase in CK-10 expression was indicative of the increased activity of keratinocytes because of the underlying tumor. This finding was consistent with clinical findings such as hyperkeratosis and keratin horn development in cutaneous SCC. [96] The combination of the IHC profile, the presence

of CK-8/18, the upregulation of p53, and the tumor morphological appearance from benign to ulcerating indicated that this orthotopic model recapitulated the pathophysiologic behavior of cutaneous SCC. In contrast to the 50 weeks needed for the two-step chemical carcinogenesis model, our model developed tumors within 2 weeks, which is advantageous for rapid screening and optimization of drugs and imaging agents *in vivo*. Another advantage of an orthotopic model was that injection of tumor cells allows the researcher to know exactly where the tumors will grow on the animal for more precise design of experiments, while avoiding inducing skin pigmentation that is a side-effect of the promotion phase of the chemically-induced model.

8.5 Conclusions

The multifunctional theranostic agent LS797 allowed for tumor visualization via optical imaging, followed by PDT. The dual excitation of cypate for imaging, and Ce6 for PDT, provided image guidance for spatiotemporal generation of cytotoxic reactive oxygen species in the tumor region. LS797 may be used to guide surgical resection or tumor margin assessment before or after PDT. LS797 caused visible contrast between the tumor and surrounding skin that could provide feedback to a clinician when resecting a tumor surgically; particularly for real-time feedback during Mohs surgery. LS797 may provide an alternative to MAL-PDT as it did not require the treated tumors to be focal in nature due to intravenous administration and tumor targeting of the compound. Tumor targeting would allow for wide-field light application for the induction of tumor-specific therapy with a reduction in off-target side effects.

We demonstrated that LS797 was able to identify all tumors via NIR fluorescence imaging. LS797-mediated PDT inhibited tumor growth, and activated apoptosis of cells *in vitro*. The tumor targeting, NIR imaging, and PDT capabilities of LS797 made it a unique theranostic agent for skin

cancer therapy. Further optimization of LS797 dose, light dose, and drug-light interval would be necessary to reveal the full potential of LS797.

Chapter 9 :

Conclusions on Fluorescence Guided Tumor Imaging

Through this body of work, we have demonstrated that planar fluorescence imaging can be used to identify and structurally characterize tumors. We showed that fluorescence has many potential applications in oncologic medical imaging. The first step in the clinical translation of a technology is to determine the appropriate applications. Here we showed that tumor imaging, in structures such as skin and blood vessels, is a natural fit for real-time fluorescence imaging. The NIR optical window, when combined with custom fluorophores and innovative algorithms, allowed for the development and validation of dual-wavelength depth imaging in tissue. Clinical questions, such as the tumor boundary and the depth of tumor invasion, remain relevant to improving patient care and outcomes.

To push the science further, we developed algorithms that allowed us to examine the role of dynamic imaging. The vascular perfusion technique was demonstrated using fluorescence imaging. This technique could be adapted for oncologic or rheumatologic applications examining vascular perfusion of tissue. Understanding the number of circulating tumor cells *in vivo* may prove to be a method for monitoring disease progression and the risk of metastasis. We also focused on the role of therapy and demonstrated photodynamic therapy in skin. Photodynamic therapy has been conducted previously; however, we added simultaneous imaging to our application.

In summary, we showed that fluorescence imaging has many potential oncologic applications. Real-time fluorescence guided imaging is used currently in several medical fields. Through the addition of novel image processing algorithms, fluorescence guided imaging can be expanded to provide increasingly quantitative output. Our results demonstrate the potential for semi-quantitative tumor fluorescence imaging, and thereby lay the groundwork for translation into future clinical applications.

References

1 Frangioni, J. In vivo near-infrared fluorescence imaging. *Curr Opin in Chem Biol* **7**, 626-634 (2003).

2 Becker, A. *et al.* Receptor-targeted optical imaging of tumors with near-infrared fluorescent ligands. *Nature Biotechnology* **19**, 327-331 (2001).

3 Luker, G. D. & Luker, K. E. Optical imaging: current applications and future directions. *Journal of nuclear medicine : official publication, Society of Nuclear Medicine* **49**, 1-4, doi:10.2967/jnumed.107.045799 (2008).

4 Achilefu, S. *et al.* Synergistic effects of light-emitting probes and peptides for targeting and monitoring integrin expression. *Proc Natl Acad Sci* **102**, 7976–7981 (2005).

5 Tomayko, M. & Reynolds, C. Determination of subcutaneous tumor size in athymic (nude) mice. *Cancer chemeotherapy and pharmacology* **24**, 148-154 (1989).

6 Euhus, D., Hudd, C., LaRegina, M. & Johnson, F. Tumor measurement in the nude mouse. *J Surg Oncol* **31**, 229-234 (1986).

7 Ishimori, T., Tatsumi, M. & Wahl, R. L. Tumor response assessment is more robust with sequential CT scanning than external caliper measurements. *Academic radiology* **12**, 776-781, doi:10.1016/j.acra.2005.03.062 (2005).

8 Hielscher, A. H. Optical tomographic imaging of small animals. *Current opinion in biotechnology* **16**, 79-88, doi:10.1016/j.copbio.2005.01.002 (2005).

9 Graves, E. E., Weissleder, R. & Ntziachristos, V. Fluorescence Molecular Imaging of Small Animal Tumor Models. *Curr Mol Med* **4**, 419-430 (2004).

10 Jenkins, D. *et al.* Bioluminescent imaging (BLI) to improve and refine traditional murine models of tumor growth and metastasis. *Clin Exp Metastasis* **20**, 733-744 (2003).

11 Liu, Y. *et al.* Hands-free, wireless goggles for near-infrared fluorescence and real-time image-guided surgery. *Surgery* **149**, 689-698 (2011).

12 Wilke, L. G., Czechura, T., Wang, C. & et al. Repeat surgery after breast conservation for the treatment of stage 0 to ii breast carcinoma: A report from the national cancer data base, 2004-2010. *JAMA Surgery* **149**, 1296-1305, doi:10.1001/jamasurg.2014.926 (2014).

13 Atallah, I. *et al.* Role of near-infrared fluorescence imaging in head and neck cancer surgery: from animal models to humans. *Eur Arch Otorhinolaryngol* **272**, 2593-2600, doi:10.1007/s00405-014-3224-y (2015).

14 Miles, B. A. *et al.* Operative Margin Control With High-Resolution Optical Microendoscopy for Head and Neck Squamous Cell Carcinoma. *Laryngoscope* **125**, 2308-2316, doi:10.1002/lary.25400 (2015).

15 Mondal, S. B. *et al.* Real-time fluorescence image-guided oncologic surgery. *Advances in cancer research* **124**, 171-211, doi:10.1016/B978-0-12-411638-2.00005-7 (2014).

16 de Boer, E. *et al.* Optical innovations in surgery. *The British journal of surgery* **102**, e56-72, doi:10.1002/bjs.9713 (2015).

17 Rudin, M. & Weissleder, R. Molecular imaging in drug discovery and development. *Nat. Rev. Drug Discov.* **2**, 123-131 (2003).

18 Gioux, S., Choi, H. S. & Frangioni, J. V. Image-guided surgery using invisible near-infrared light: fundamentals of clinical translation. *Molecular imaging* **9**, 237-255 (2010).

19 Zhu, B., Rasmussen, J. C., Lu, Y. & Sevick-Muraca, E. M. Reduction of excitation light leakage to improve near-infrared fluorescence imaging for tissue surface and deep tissue imaging. *Medical physics* **37**, 5961-5970 (2010).
20 Heintzmann, R. in *Handbook Of Biological Confocal Microscopy* (ed James B. Pawley) Ch. 13, 265-279 (Springer US, 2006).
21 Neil, M. A., Juskaitis, R. & Wilson, T. Method of obtaining optical sectioning by using structured light in a conventional microscope. *Optics letters* **22**, 1905-1907 (1997).
22 Yang, B., Sharma, M. & Tunnell, J. W. Attenuation-corrected fluorescence extraction for image-guided surgery in spatial frequency domain. *Journal of biomedical optics* **18**, 80503, doi:10.1117/1.JBO.18.8.080503 (2013).
23 Krishnaswamy, V. *et al.* Structured light scatteroscopy. *Journal of biomedical optics* **19**, 070504, doi:10.1117/1.JBO.19.7.070504 (2014).
24 Maji, D. *et al.* Noninvasive imaging of focal atherosclerotic lesions using fluorescence molecular tomography. *Journal of biomedical optics* **19**, 110501, doi:10.1117/1.JBO.19.11.110501 (2014).
25 Solomon, M. *et al.* Detection of enzyme activity in orthotopic murine breast cancer by fluorescence lifetime imaging using a fluorescence resonance energy transfer-based molecular probe. *Journal of biomedical optics* **16**, 066019, doi:10.1117/1.3594153 (2011).
26 Mazhar, A. *et al.* Structured illumination enhances resolution and contrast in thick tissue fluorescence imaging. *Journal of biomedical optics* **15**, 010506, doi:10.1117/1.3299321 (2010).
27 Soodgupta, D. *et al.* Ex vivo and in vivo evaluation of over-expressed VLA-4 in multiple myeloma using LLP2A imaging agents. *Journal of nuclear medicine : official publication, Society of Nuclear Medicine*, doi:10.2967/jnumed.115.164624 (2016).
28 Calabro, K., Curtis, A., Galarneau, J. R., Krucker, T. & Bigio, I. J. Gender variations in the optical properties of skin in murine animal models. *Journal of biomedical optics* **16**, 011008, doi:10.1117/1.3525565 (2011).
29 Ntziachristos, V. *et al.* Planar fluorescence imaging using normalized data. *Journal of biomedical optics* **10**, 064007, doi:10.1117/1.2136148 (2005).
30 Sarder, P. *et al.* Dynamic optical projection of acquired luminescence for aiding oncologic surgery. *Journal of biomedical optics* **18**, 120501, doi:10.1117/1.JBO.18.12.120501 (2013).
31 Keren, S., Gheysens, O., Levin, C. S. & Gambhir, S. S. A comparison between a time domain and continuous wave small animal optical imaging system. *IEEE transactions on medical imaging* **27**, 58-63, doi:10.1109/TMI.2007.902800 (2008).
32 Soodgupta, D. *et al.* Very late antigen-4 (alpha(4)beta(1) Integrin) targeted PET imaging of multiple myeloma. *PloS one* **8**, e55841, doi:10.1371/journal.pone.0055841 (2013).
33 Soodgupta, D. *et al.* Ex Vivo and In Vivo Evaluation of Overexpressed VLA-4 in Multiple Myeloma Using LLP2A Imaging Agents. *Journal of nuclear medicine : official publication, Society of Nuclear Medicine* **57**, 640-645, doi:10.2967/jnumed.115.164624 (2016).
34 Miller, J. P., Egbulefu, C., Prior, J. L., Zhou, M. & Achilefu, S. Gradient-Based Algorithm for Determining Tumor Volumes in Small Animals Using Planar Fluorescence Imaging Platform. *Tomography* **2**, 17-25, doi:10.18383/j.tom.2016.00100 (2016).

35 Belanger, S., Abran, M., Intes, X., Casanova, C. & Lesage, F. Real-time diffuse optical tomography based on structured illumination. *Journal of biomedical optics* **15**, 016006, doi:10.1117/1.3290818 (2010).
36 Angelo, J. *et al.* Depth-enhanced fluorescence imaging using masked detection of structured illumination. *Journal of biomedical optics* **19**, 116008, doi:10.1117/1.JBO.19.11.116008 (2014).
37 O'Sullivan, T. D., Cerussi, A. E., Cuccia, D. J. & Tromberg, B. J. Diffuse optical imaging using spatially and temporally modulated light. *Journal of biomedical optics* **17**, 071311, doi:10.1117/1.JBO.17.7.071311 (2012).
38 Muldoon, T. J., Burgess, S. A., Chen, B. R., Ratner, D. & Hillman, E. M. Analysis of skin lesions using laminar optical tomography. *Biomedical optics express* **3**, 1701-1712, doi:10.1364/BOE.3.001701 (2012).
39 Swartling, J., Svensson, J., Bengtsson, D., Terike, K. & Andersson-Engels, S. Fluorescence spectra provide information on the depth of fluorescent lesions in tissue. *Appl Opt* **44**, 1934-1941 (2005).
40 Kolste, K. *et al.* Macroscopic optical imaging technique for wide-field estimation of fluorescence depth in optically turbid media for application in brain tumor surgical guidance. *Journal of biomedical optics* **20** (2015).
41 Jacques, S. L. Corrigendum: Optical properties of biological tissues: a review. *Physics in Medicine and Biology* **58**, 5007-5008, doi:10.1088/0031-9155/58/14/5007 (2013).
42 Achilefu, S., Dorshow, R. B., Bugaj, J. E. & Rajagopalan, R. Novel receptor-targeted fluorescent contrast agents for in vivo tumor imaging. *Investigative radiology* **35**, 479-485 (2000).
43 Galley, W. C. & Stryer, L. Triplet-Triplet Energy Transfer in Proteins as a Criterion of Proximity. *P Natl Acad Sci USA* **60**, 108-&, doi:DOI 10.1073/pnas.60.1.108 (1968).
44 Jacques, S. L. Optical properties of biological tissues: a review. *Phys Med Biol* **58**, R37-61, doi:10.1088/0031-9155/58/11/R37 (2013).
45 Cuccia, D. J., Bevilacqua, F., Durkin, A. J., Ayers, F. R. & Tromberg, B. J. Quantitation and mapping of tissue optical properties using modulated imaging. *Journal of biomedical optics* **14**, 024012, doi:10.1117/1.3088140 (2009).
46 Hillman, E. M. *et al.* In vivo optical imaging and dynamic contrast methods for biomedical research. *Philosophical transactions. Series A, Mathematical, physical, and engineering sciences* **369**, 4620-4643, doi:10.1098/rsta.2011.0264 (2011).
47 Hillman, E. & Moore, A. All-optical anatomical co-registration for molecular imaging of small animals using dynamic contrast. *Nature Photonics* **1**, 526-530 (2007).
48 Kang, Y. *et al.* Quantitative analysis of peripheral tissue perfusion using spatiotemporal molecular dynamics. *PloS one* **4**, e4275, doi:10.1371/journal.pone.0004275 (2009).
49 Zhou, H. *et al.* Dynamic Near-Infrared Optical Imaging of 2-Deoxyglucose Uptake by Intracranial Glioma of Athymic Mice. *PloS one* **4**, e8051, doi:10.1371/journal.pone.0008051.g001 (2009).
50 Lee, J. *et al.* Dynamic Fluorescence Imaging for the Detection of Vascular Changes in Anti-Angiogenic Drug Therapy. *Optical Society of America* **JMA74** (2010).
51 Seo, J. *et al.* Principal component analysis of dynamic fluorescence images for diagnosis of diabetic vasculopathy. *Journal of biomedical optics* **21**, 46003, doi:10.1117/1.JBO.21.4.046003 (2016).

52 Lee, H., Mason, J. C. & Achilefu, S. Heptamethine Cyanine Dyes with a Robust C−C Bond at the Central Position of the Chromophore. *J. Org. Chem.* **71**, 7862–7865 (2006).
53 Ye, Y., Bloch, S., Kao, J. & Achilefu, S. Multivalent Carbocyanine Molecular Probes: Synthesis and Applications. *Bioconjugate Chem.* **16**, 51–61 (2005).
54 Berezin, M. Y. *et al.* Rational approach to select small peptide molecular probes labeled with fluorescent cyanine dyes for in vivo optical imaging. *Biochemistry* **50**, 2691-2700, doi:10.1021/bi2000966 (2011).
55 Nishida, N., Yano, H., Nishida, T., Kamura, T. & Kojiro, M. Angiogenesis in Cancer. *Vasc Health Risk Manag* **2**, 213-219 (2006).
56 Nagy, J. A., Chang, S. H., Dvorak, A. M. & Dvorak, H. F. Why are tumour blood vessels abnormal and why is it important to know? *British journal of cancer* **100**, 865-869, doi:10.1038/sj.bjc.6604929 (2009).
57 Holland, R., Veling, S. H. J., Mravunac, M. & Hendriks, J. H. C. L. Histologic multifocality of tis, T1–2 breast carcinomas implications for clinical trials of breast-conserving surgery. *Cancer* **56**, 979-990 (1985).
58 Wilkinson, L. S. *et al.* Increasing the diagnosis of multifocal primary breast cancer by the use of bilateral whole-breast ultrasound. *Clinical radiology* **60**, 573-578, doi:10.1016/j.crad.2004.10.015 (2005).
59 Hlawatsch, A., Teifke, A., Schmidt, M. & Thelen, M. Preoperative Assessment of Breast Cancer: Sonography Versus MR Imaging. *American Journal of Roentgenology* **179**, 1493-1501 (2002).
60 Bozzini, A. *et al.* Sensitivity of imaging for multifocal-multicentric breast carcinoma. *BMC cancer* **8**, 275, doi:10.1186/1471-2407-8-275 (2008).
61 Harms, S. *et al.* MR imaging of the breast with rotating delivery of excitation off resonance: clinical experience with pathologic correlation. *Radiology* **187**, 493-501 (1993).
62 Boetes, C. *et al.* Breast tumors: comparative accuracy of MR imaging relative to mammography and US for demonstrating extent. *Radiology* **197**, 743-747 (1995).
63 Saarela, A. O., Paloneva, T. K., Rissanen, T. J. & Kiviniemi, H. O. Determinants of positive histologic margins and residual tumor after lumpectomy for early breast cancer: A prospective study with special reference to touch preparation cytology. *Journal of Surgical Oncology* **66**, 248–253 (1997).
64 Jacobs, L. Positive margins: the challenge continues for breast surgeons. *Annals of surgical oncology* **15**, 1271-1272, doi:10.1245/s10434-007-9766-0 (2008).
65 Balch, G. C., Mithani, S. K., Simpson, J. F. & Kelley, M. C. Accuracy of Intraoperative Gross Examination of Surgical Margin Status in Women Undergoing Partial Mastectomy for Breast Malignancy. *The American Surgeon* **71**, 22-28 (2005).
66 Vahrmeijer, A. L., Hutteman, M., van der Vorst, J. R., van de Velde, C. J. & Frangioni, J. V. Image-guided cancer surgery using near-infrared fluorescence. *Nature reviews. Clinical oncology* **10**, 507-518, doi:10.1038/nrclinonc.2013.123 (2013).
67 Cima, I. *et al.* Tumor-derived circulating endothelial cell clusters in colorectal cancer. *Science translational medicine* **8**, 345ra389, doi:10.1126/scitranslmed.aad7369 (2016).
68 Hou, J. M. *et al.* Clinical significance and molecular characteristics of circulating tumor cells and circulating tumor microemboli in patients with small-cell lung cancer. *Journal of clinical oncology : official journal of the American Society of Clinical Oncology* **30**, 525-532, doi:10.1200/JCO.2010.33.3716 (2012).

69 Hou, J. M. *et al.* Circulating Tumor Cells as a Window on Metastasis Biology in Lung Cancer. *Am J Pathol* **178**, 989-996, doi:10.1016/j.ajpath.2010.12.003 (2011).
70 Brandt, B. *et al.* Isolation of prostate-derived single cells and cell clusters from human peripheral blood. *Cancer Res* **56**, 4556-4561 (1996).
71 Molnar, B., Ladanyi, A., Tanko, L., Sreter, L. & Tulassay, Z. Circulating tumor cell clusters in the peripheral blood of colorectal cancer patients. *Clin Cancer Res* **7**, 4080-4085 (2001).
72 Cho, E. H. *et al.* Characterization of circulating tumor cell aggregates identified in patients with epithelial tumors. *Phys Biol* **9**, doi:Artn 01600110.1088/1478-3975/9/1/016001 (2012).

73 Fidler, I. J. The relationship of embolic homogeneity, number, size and viability to the incidence of experimental metastasis. *European journal of cancer* **9**, 223-227 (1973).
74 Aceto, N. *et al.* Circulating tumor cell clusters are oligoclonal precursors of breast cancer metastasis. *Cell* **158**, 1110-1122, doi:10.1016/j.cell.2014.07.013 (2014).
75 Esmaeilsabzali, H., Beischlag, T. V., Cox, M. E., Parameswaran, A. M. & Park, E. J. Detection and isolation of circulating tumor cells: principles and methods. *Biotechnology advances* **31**, 1063-1084, doi:10.1016/j.biotechadv.2013.08.016 (2013).
76 Georgakoudi, I. *et al.* In vivo flow cytometry: a new method for enumerating circulating cancer cells. *Cancer Res* **64**, 5044-5047, doi:10.1158/0008-5472.CAN-04-1058 (2004).
77 Zettergren, E. *et al.* Instrument for fluorescence sensing of circulating cells with diffuse light in mice in vivo. *Journal of biomedical optics* **17**, 037001, doi:10.1117/1.JBO.17.3.037001 (2012).
78 Sasportas, L. S. & Gambhir, S. S. Imaging Circulating Tumor Cells in Freely Moving Awake Small Animals Using a Miniaturized Intravital Microscope. *PloS one* **9**, doi:ARTN e8675910.1371/journal.pone.0086759 (2014).

79 Achilefu, S. *et al.* Synergistic effects of light-emitting probes and peptides for targeting and monitoring integrin expression. *PNAS* **102**, 7976-7981 (2005).
80 Alam, M. & Ratner, D. Cutaneous squamous-cell carcinoma. *N Engl J Med* **344**, 975-983 (2001).
81 Armstrong, B. & Krickerb, A. The epidemiology of UV induced skin cancer. *Photochem Photobiol* **63**, 8-18 (2001).
82 Brash, D. *et al.* A role for sunlight in skin cancer: UV-induced p53 mutations in squamous cell carcinoma. *P Natl Acad Sci USA* **88**, 10124-10128, (1991).
83 Gloster, H. M., Jr. & Neal, K. Skin cancer in skin of color. *Journal of the American Academy of Dermatology* **55**, 741-760, doi:10.1016/j.jaad.2005.08.063 (2006).
84 Gray, D. T. *et al.* Trends in the Population-Based Incidence of Squamous Cell Carcinoma of the Skin First Diagnosed Between 1984 and 1992. *Arch Dermatol* **133**, 735-740 (1997).
85 Karagas, M. R., Greenberg, E. R., Spencer, S. K., Stuckel, T. A. & Mott, L. A. Increase in incidence rates of basal cell and squamous cell skin cancer in New Hampshire, USA. *Int J Cancer* **81** (1999).
86 Lansbury, L. *et al.* Interventions for non-metastatic squamous cell carcinoma of the skin. *Cochrane Database Syst Rev* **14** (2010).
87 Lansbury, L., Bath-Hextall, F., Perkins, W., Stanton, W. & Leonardi-Bee, J. Interventions for non-metastatic squamous cell carcinoma of the skin: systematic review and pooled analysis of observational studies. *BMJ* **347**, f6153, doi:10.1136/bmj.f6153 (2013).

88 Sato, K., Nagaya, T., Choyke, P. L. & Kobayashi, H. Near infrared photoimmunotherapy in the treatment of pleural disseminated NSCLC: preclinical experience. *Theranostics* **5**, 698-709, doi:10.7150/thno.11559 (2015).
89 Li, R. *et al.* A Novel Tumor Targeting Drug Carrier for Optical Imaging and Therapy. *Theranostics* **4**, 642-659, doi:10.7150/thno.8527 (2014).
90 Peng, P. C. *et al.* Dual-effect liposomes encapsulated with doxorubicin and chlorin e6 augment the therapeutic effect of tumor treatment. *Lasers in surgery and medicine* **47**, 77-87, doi:10.1002/lsm.22312 (2015).
91 Mondal, S. B. *et al.* Binocular Goggle Augmented Imaging and Navigation System provides real-time fluorescence image guidance for tumor resection and sentinel lymph node mapping. *Scientific reports* **5**, 12117, doi:10.1038/srep12117 (2015).
92 Biswas, R., Moon, J. H. & Ahn, J. C. Chlorin e6 derivative radachlorin mainly accumulates in mitochondria, lysosome and endoplasmic reticulum and shows high affinity toward tumors in nude mice in photodynamic therapy. *Photochem Photobiol* **90**, 1108-1118, doi:10.1111/php.12273 (2014).
93 Park, H. & Na, K. Conjugation of the photosensitizer Chlorin e6 to pluronic F127 for enhanced cellular internalization for photodynamic therapy. *Biomaterials* **34**, 6992-7000, doi:10.1016/j.biomaterials.2013.05.070 (2013).
94 Abel, E. L., Angel, J. M., Kiguchi, K. & DiGiovanni, J. Multi-stage chemical carcinogenesis in mouse skin: fundamentals and applications. *Nature protocols* **4**, 1350-1362, doi:10.1038/nprot.2009.120 (2009).
95 Rheinwald, J. & Beckett, M. Tumorigenic keratinocyte lines requiring anchorage and fibroblast support cultured from human squamous cell carcinomas. *Cancer Res* **41**, 1657-1663 (1981).
96 Norman, R. A. & Young, E. M. Squamous Cell Carcinoma. 329-336, doi:10.1007/978-1-4471-4579-0_50 (2014).
97 Rothnagel, J. *et al.* Mutations in the Rod Domains of Keratins 1 and 10 in Epidermolytic Hyperkeratosis. *Science* **257**, 1128-1130 (1992).
98 Einspahr, J. G. *et al.* Relationship of p53 Mutations to Epidermal Cell Proliferation and Apoptosis in Human UV-Induced Skin Carcinogenesis. *Neoplasia* **1**, 468-475 (1999).
99 Bagazgoitia, L., Cuevas Santos, J., Juarranz, A. & Jaen, P. Photodynamic therapy reduces the histological features of actinic damage and the expression of early oncogenic markers. *Br J Dermatol* **165**, 144-151, doi:10.1111/j.1365-2133.2011.10270.x (2011).
100 Talghini, S., Halimi, M. & Baybordi, H. Expression of P27, Ki67 and P53 in squamous cell carcinoma, actinic keratosis and Bowen disease. *Pak J Biol Sci* **12**, 929-933 (2009).
101 Verhaegen, M. E. *et al.* Merkel cell polyomavirus small T antigen is oncogenic in transgenic mice. *The Journal of investigative dermatology* **135**, 1415-1424, doi:10.1038/jid.2014.446 (2015).